



UNIVERSITÀ DI PISA
Corso di Laurea Magistrale di Fisica

Event Time Estimate with the Belle II Silicon Strip Vertex Detector

Relatori
Dott.ssa Giulia Casarosa
Prof. Francesco Forti

Candidate
Silvia De Benedictis
605781

Anno Accademico 2021-2022

*Was finden wir jenseits
dieses Horizontes?*

Contents

Introduction	4
1 Belle II physics program	7
1.1 Standard Model	7
1.2 Intensity frontier physics	11
1.3 <i>B</i> factories	13
2 Belle II & SuperKEKB	17
2.1 SuperKEKB accelerator	17
2.1.1 Bunch crossing	19
2.1.2 Beam background	21
2.2 Belle II detector overview	23
2.2.1 Belle II current status	30
2.2.2 Belle Analysis Framework II	31
2.3 Trigger	32
2.3.1 L1 trigger	32
2.3.2 High Level Trigger	34
2.4 Tracking	36
2.4.1 Typical $B^0\bar{B}^0$ and $\tau^+\tau^-$ events	38
3 Time Measurements	43
3.1 Motivations for time measurements	43
3.2 Strip detectors	44
3.3 SVD data acquisition	46
3.4 Cluster reconstruction	49
3.5 SVD Cluster Time	51
3.6 CDC and TOP EventT0	54
4 Event Time estimate with SVD	57
4.1 Event time computation	57
4.2 Event time estimate on Monte Carlo	61

4.2.1	$B^0\bar{B}^0$ events without beam background	62
4.2.2	$B^0\bar{B}^0$ events with nominal beam background	70
4.2.3	$\tau^+\tau^-$ events with nominal background	71
4.3	Summary on simulated events	77
5	SVD event time estimate on data	78
5.1	Data samples	78
5.2	Preliminary checks on hadronic events	79
5.3	SVD Event Time for hadronic events	81
5.4	SVD Event Time for Bhabha and μ -pairs	85
5.5	Summary of the performances on data	87
5.6	Future prospects	88
	Conclusions	91
	Bibliography	92

Introduction

Although the Standard Model (SM) of particle physics is the most complete theory that describes the particles interactions at a fundamental level, supported by a large amount of experimental observations, it leaves several open questions about why there are only three generations of quarks, whether the Higgs mechanism is accountable for the neutrino masses, inferred from their oscillations, or not, and the amount of the asymmetry between matter and antimatter in the universe. The answers to these questions may be found beyond the Standard Model in the context of New Physics (NP) models. The New Physics is searched for in different ways, such as: the "energy frontier", in which particles are directly produced thanks to higher energy, like in LHC, or the "intensity frontier", that carry on indirect searches in the huge amount of data collected thanks to high luminosity. The Belle II experiment belongs to the "intensity frontier" framework. It is installed at the KEK laboratory, previously hosting the Belle experiment: its goal is to reach a nominal luminosity of $6.5 \times 10^{35} \text{cm}^{-2}\text{s}^{-1}$, that is around 30 times higher than the Belle luminosity, at the SuperKEKB asymmetric e^+e^- collider tuned at the $\Upsilon(4S)$ resonance ($\sqrt{s}=10.58\text{GeV}$), that makes it a B factory. The high efficiency detector is composed, in the innermost region, of a Vertex Detector (VXD), made by the Pixel Detector (PXD) and the Silicon Vertex Detector (SVD), a Central Drift Chamber (CDC), that takes care of the tracking reconstruction for charged particles together with the VXD and of the Particle Identification thanks to measurements of energy losses. In the barrel region there are the Time-of-Propagation (TOP) and the Aerogel Ring Imaging Cherenkov (ARICH) detector, that provide the Particle Identification thanks to the detection of the Cherenkov light, and the Electromagnetic Calorimeter (ECL), that performs energy measurements to discern neutral particles from electrons; in the outermost region there is the K_L -Muon Detector (KLM), in charge of detecting the stable long lived particles through hadronic showers. The Belle II triggering system is composed of a hardware stage (Level 1 trigger) and a software stage (High Level Trigger) that runs the online reconstruction and is prepared to face the beam background produced by the high

luminosity with high efficiency ($\sim 99\%$ on $B\bar{B}$ events): to perform high precision measurements, an efficient rejection of the background is necessary. An important feature that can be exploited to distinguish the beam background hits from signals is their timing. The Belle II sub-detectors collect different time information of an event, that is the time the e^+e^- collision, or the time of a hit in the Silicon Vertex Detector: if a hit is temporally near to the time of the collision, it is more likely to be signal, while if the hit is off-time with respect to the time of the event, it is more likely to be a beam background hit. A fast and efficient timing system is therefore fundamental to provide a good selection on data. There are stringent requirements on the execution time of the full reconstruction to avoid stopping the data acquisition because of the full trigger processing capacity (*trigger busy*). Among the processes in the online full event reconstruction, the estimate of the event time is one that takes the longest. This thesis work focuses on the estimate of the event time with the SVD, which is a 4-layer device based on double-sided strip detector readout by fast electronics (the APV25 chip developed for the CMS experiment). It has a high hit detection efficiency ($>99\%$ for most sensors) and a time resolution on crossing particles of 2-4ns.

In Chapter 1, the Standard Model of particles is briefly discussed together with an overview of the Belle II physics program, including the description of B factories working principles.

In Chapter 2, the SuperKEKB accelerator is described, with particular attention to the beam properties and the background sources; the expected contribution of the latter on the occupancy (i.e. the fraction of strips with a signal above threshold) in SVD is shown. Then, the Belle II detector and its components are described, together with the triggering scheme and the tracking reconstruction. Finally, the topology of typical Monte Carlo simulated $B^0\bar{B}^0$ and $\tau^+\tau^-$ events is studied, with particular attention to the SVD related observables, like the number of SVD hits; the choice of these events is not casual, since they are extreme cases: the former is one of the event types with the highest track multiplicity (~ 10 per event on average), while the latter is one with the lowest track multiplicity (~ 2 per event on average); $\mu^+\mu^-$ events, that have 2 charged tracks per event, are excluded since they are used for calibration purposes and not for interesting physics analyses.

In Chapter 3, the SVD working principles are described, starting from the functioning of strip detectors, and going through the data acquisition and the cluster reconstruction. Particular attention is given to the description of the computation of the cluster time starting from the raw data up to the calibrated data. Finally, the `EventT0`, i.e. the time of the e^+e^- collision with respect to the trigger is mentioned together with the `CDC` and `TOP`

contributions.

In Chapter 4, the event time estimate with the SVD is given and its performance on Monte Carlo events is discussed: $B^0\bar{B}^0$, with and without nominal beam background, and $\tau^+\tau^-$, studied directly with nominal beam background. After an optimization of the algorithm, it results to have an absolute efficiency of 96% at least and a resolution greater than 1ns measured on the residuals.

In Chapter 5, the algorithm is applied to data and its performances are studied: on hadronic events the estimate reaches an absolute efficiency greater than 99.8% and a resolution of $\mathcal{O}(1\text{ns})$; to study the possibility to use it online on all event types, it is also tested on different datasets, both hadronic and leptonic ($e^+e^- \rightarrow e^+e^-, \mu^+\mu^-$) that is confirmed by a great compatibility among the results. Moreover, the execution time of the algorithm is computed with respect to the current modules employed at Belle II and results to be 2000 times faster than the current ones.

Chapter 1

Belle II physics program

The Belle II experiment at SuperKEKB, an asymmetric-energy e^+e^- collider in Tsukuba, Japan, has the ambitious goal to reach an integrated luminosity of 50 ab^{-1} at the $\Upsilon(4S)$ resonance to perform precision measurements in the heavy flavour sector, and search for new physics (NP) thanks to a clean environment and high resolution detectors. In this chapter, after a brief discussion of the Standard Model, an overview of the Belle II physics program is discussed, with particular attention to the main features of B factories.

1.1 Standard Model

The most complete theory describing the constituent of matter and their interaction at a fundamental level is the Standard Model of particle physics (SM)[1], whose fundamental constituents are shown in fig.1.1. The interactions between particles are described as fields mediated by vector gauge bosons, spin-1 particles described by Bose-Einstein statistics. The gauge bosons are:

- the photon, γ , a massless neutral particle that couples to charged fermions and mediates the electromagnetic interactions, defined by the $U(1)$ group;
- the W^\pm bosons, that mediate charged currents (CC) and the Z^0 boson, that mediates neutral current (NC) in weak interactions. These three bosons form a triplet in the $SU(2)$ isospin space;
- the gluons g form an octet of color and mediate the strong interactions.

The matter constituents are fermions, spin- $\frac{1}{2}$ particles described by the Fermi-Dirac statistics, and are divided into two categories, quarks and leptons, each

1.1. STANDARD MODEL

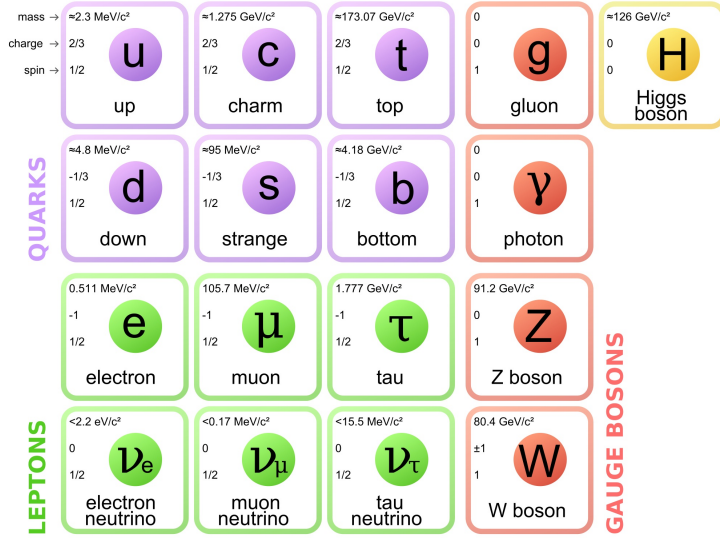


Figure 1.1: Elementary particles of the Standard Model.

one with three generations of isospin doublets. Each fermion has an antiparticle, with the same mass but opposite charge and quantum numbers. Fermion fields can be split in two orthogonal components of opposite chirality, namely right-handed and left-handed. For massive particles, chirality eigenstates are expressed as linear combinations of helicity eigenstates; in the ultrarelativistic regime, as the particle mass becomes negligible, chirality eigenstates can be approximate to the helicity eigenstates themselves. Chirality becomes relevant in weak interactions since only left-handed particles are involved, whereas it is irrelevant place in electromagnetic and strong ones. Fermions are arranged in isospin doublets

$$\begin{pmatrix} \nu_l \\ l \end{pmatrix}, \begin{pmatrix} u \\ d \end{pmatrix}$$

where u -type quarks and neutrinos have $I_z = \frac{1}{2}$, isospin projection on the z -axis, whereas d -type quarks and charged leptons have $I_z = -\frac{1}{2}$, similarly for what happens for the spin projection on the z -axis, s_z . For what concerns leptons, the three doublets have an associated lepton number $L(e, \mu, \tau)$, that introduces the accidental lepton flavor conservation, and are formed by a massive charged fermion ($q = -e$, $s_z = -\frac{1}{2}$, $I_z = -\frac{1}{2}$) and their relative neutrino ($q = 0$, $s_z = +\frac{1}{2}$, $I_z = +\frac{1}{2}$): while the former joins both electromagnetic and weak interactions, the latter, since neutral, is sensitive to weak interactions only: this means, in terms of chirality, that right-handed neutrinos, if existing, do not interact.

Quark doublets have the same isospin structure as leptons, but the *up* type quarks, namely u , c , t , have charge $q = +\frac{2}{3}e$, while the *down* type quarks, corresponding to d , s , b , have charge $q = -\frac{1}{3}e$; both *up* and *down* type quarks are massive, with masses that range from tens of MeV/c^2 to almost two hundreds of GeV/c^2 . Quarks interact through electromagnetic, strong, and weak interactions; they are associated to an additional quantum number representing their own flavor, which is not conserved by weak interactions, and to a color quantum number, that determines in strong interactions. Combining a quark and an antiquark, or three quarks (or three antiquarks), mesons and baryons, colorless particles arranged in isospin multiplets, are obtained respectively; according to the quantum chromodynamics (QCD), that theorizes strong interactions, the only observable particles are colorless, therefore it is not possible to observe either isolated quarks or gluons: this phenomenon is called color confinement and imposes the hadronization of isolated quarks.

Finally, there is the Higgs boson: it is not a gauge particle since its associated field is scalar, and it is at the base of the homonymous generation mechanism accounting for the particles masses through a spontaneous symmetry breaking.

The SM Lagrangian, that describes what has been stated so far, can be expressed as:

$$\mathcal{L}_{SM} = \mathcal{L}_{kin} + \mathcal{L}_{EW} + \mathcal{L}_{QCD} + \mathcal{L}_h + \mathcal{L}_{yuk} \quad (1.1)$$

where \mathcal{L}_{kin} is the kinetic term describing gauge bosons, \mathcal{L}_{EW} describes the kinetic properties of fermions and electro-weak interactions, \mathcal{L}_{QCD} is the strong interaction term between quark and gluons, \mathcal{L}_h describes the Higgs properties and its interactions to gauge bosons, \mathcal{L}_{yuk} includes both the fermions mass term and their interactions to the Higgs boson.

Cabibbo-Kobayashi-Maskawa matrix

As previously stated, charged currents in weak interactions do not conserve the quark flavor; to allow such transitions, Nicola Cabibbo [3] theorized a $\theta_C \sim 13^\circ$ mixing angle for two quarks, between the mass eigenstates (d, s) and the eigenstates (d', s') that take part in weak interactions:

$$\begin{pmatrix} d' \\ s' \end{pmatrix} = \begin{pmatrix} \cos \theta_C & \sin \theta_C \\ -\sin \theta_C & \cos \theta_C \end{pmatrix} \begin{pmatrix} d \\ s \end{pmatrix} \quad (1.2)$$

the Cabibbo matrix is 2×2 since it only takes into account two generations. The 3×3 generalization corresponds to the Cabibbo-Kobayashi-Maskawa

1.1. STANDARD MODEL

(CKM) complex matrix:

$$V_{ij} = \begin{pmatrix} V_{ud} & V_{us} & V_{ub} \\ V_{cd} & V_{cs} & V_{cb} \\ V_{td} & V_{ts} & V_{tb} \end{pmatrix} \quad (1.3)$$

The CKM matrix has four real parameters that depend on the parametrization. The standard parametrization is the following:

$$V_{ij} = \begin{pmatrix} c_{12}c_{13} & s_{12}c_{13} & s_{13}e^{i\delta} \\ -s_{12}c_{13} - c_{12}s_{13}s_{23}e^{i\delta} & c_{12}c_{13} - s_{12}s_{13}s_{23}e^{i\delta} & c_{13}s_{23} \\ s_{12}s_{13} - c_{12}s_{13}c_{23}e^{i\delta} & -c_{12}s_{23} - s_{12}s_{13}c_{23}e^{i\delta} & c_{13}c_{23} \end{pmatrix} \quad (1.4)$$

the independent parameters are three real angles θ_{ij} and a complex phase δ . The Wolfenstein parametrization is

$$V_{ij} = \begin{pmatrix} 1 - \frac{1}{2}\lambda^2 & \lambda & A\lambda^3(\rho - i\eta) \\ -\lambda & 1 - \frac{1}{2}\lambda^2 & A\lambda^2 \\ A\lambda^3(1 - \rho - i\eta) & -A\lambda^2 & 1 \end{pmatrix} \quad (1.5)$$

the independent parameters are A , λ , ρ , and η (complex), which is responsible for CP violation; from 1.5, it is possible to deduce that transitions within the same generation are favored (diagonal terms are $\simeq 1$), while those among different ones are suppressed (the outer the terms, the more they are $\ll 1$). It is possible to write relations between the parameters of different parametrizations, for example

$$\lambda = \frac{|V_{us}|}{\sqrt{|V_{ud}|^2 + |V_{us}|^2}} = s_{12} = \sin \theta_C \sim 0.2272 \pm 0.0010$$

$$s_{23} = A\lambda^2 = \lambda \frac{|V_{cb}|}{|V_{us}|}$$

$$s_{13}e^{-i\delta} = A\lambda^3(\rho - i\eta) = V_{ub}$$

Starting from the unitarity property

$$V_{CKM}^\dagger V_{CKM} = V_{CKM} V_{CKM}^\dagger = I$$

it is possible to write nine relations between the CKM elements to define quark transitions; the three relations on the diagonal of eq.1.5 states that the probability of an u type quark, i.e. u , transitioning to a down type quark is 1 at the tree level:

$$V_{ud}V_{ud}^* + V_{us}V_{us}^* + V_{ub}V_{ub}^* = 1 \quad (1.6)$$

while the other six relations, that correspond to off-diagonal terms, affirm that down types, i.e. d , do not transition to other down types at the tree level: this property can be obtained from the unitarity of the CKM matrix and defines a set of equations:

$$\sum_{i=u,c,t} V_{ij}V_{ik}^* = 0, \quad \forall j, k = d, s, b, \quad j \neq k \quad (1.7)$$

Each of the off-diagonal term identify a unitarity triangle, whose sides and angles vary from one another and whose area is related to the CP violation contained in δ . A remarkable unitarity triangle is the one identified by eq.1.8:

$$V_{ud}V_{ub}^* + V_{cd}V_{cb}^* + V_{td}V_{tb}^* = 0 \iff \frac{V_{ud}V_{ub}^*}{V_{cd}V_{cb}^*} + 1 + \frac{V_{td}V_{tb}^*}{V_{cd}V_{cb}^*} = 0 \quad (1.8)$$

normalized to $V_{cd}V_{cb}^*$; eq. 1.8 has the sides of the same order and, in the $\rho \times \eta$ plane, has one vertex in $(0,0)$, one in $(1,0)$, and the last one in $(\rho(1 - \frac{\lambda^2}{2}), \eta(1 - \frac{\lambda^2}{2}))$, as shown in fig.1.2 The three angles can be expressed as:

$$\alpha = \phi_2 = \arg\left(\frac{V_{ud}V_{ub}^*}{V_{td}V_{tb}^*}\right), \quad \beta = \phi_1 = \arg\left(\frac{V_{td}V_{tb}^*}{V_{cd}V_{cb}^*}\right), \quad \gamma = \phi_3 = \arg\left(\frac{V_{cd}V_{cb}^*}{V_{ud}V_{ub}^*}\right).$$

Measurements of the angles are linked to the measure of CP violation, related to the imaginary part of the V_{ij} elements.

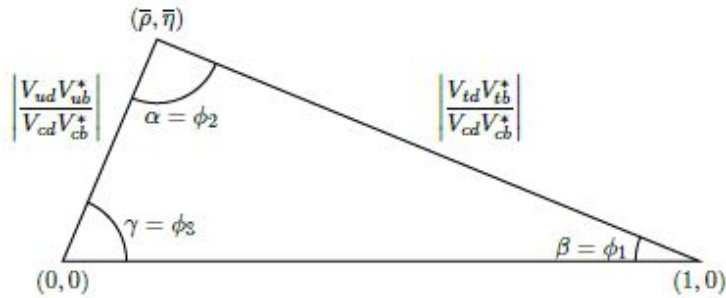


Figure 1.2: Unitarity triangle associated to eq.1.8.

1.2 Intensity frontier physics

The Standard Model (SM) [2] is not able to explain some observations such as the fermion mass hierarchy or the reasons why there are only three generation of fermions. Moreover, the observed CP violation in the quark sector is too

small to clarify the mass-antimass asymmetry in the universe. These open questions motivate New Physics (NP) models to work out where the SM fails. The search for NP is carried out in two different frameworks, the "energy frontier" and the "intensity frontier": in the former, the strategy consists in a direct search of new interactions and high mass particles at increasingly high energy and is pursued at the Large Hadron Collider (LHC) in Geneva, Switzerland, with experiments, ATLAS and CMS; in the latter, the goal is to observe deviations from the SM induced by the presence of new particles participating in the SM processes or to observe transitions that are forbidden in the SM. This requires very large data samples that experiments such as Belle II @SuperKEKB and LHCb @LHC can access.

The search for NP at Belle II sets in the spotlight channels with small theoretical uncertainties that promote high precision measurements to compare to SM predictions: inconsistencies may be a strong evidence for NP. The current search for NP, hinted by past and on-going experiments, revolves around flavor and non-flavor related programs, discussed briefly hereafter.

Flavor related NP program

Among flavor related researches, the focus is on different topics, e.g. the search for new phases for the CP violation, the nature of Higgs boson, and the search for Lepton Flavour Violation (LFV). Furthermore, high precision measurements of CKM matrix elements and phases are being carried on.

For what concerns the CP violation, an example of mesons that offer the opportunity to study it are K^0 's, D^0 's, B^0 's and B_s^0 's, and their respective antiparticles. In a $M^0\bar{M}^0$ system, CP violation can take place in the mixing, in the decay or in the interference of decays with and without mixing. The measurement of the $\sin 2\beta$, where β or ϕ_1 is an angle of the unitarity triangle identified by the elements of the CKM matrix, is an evidence of CP violation. Pivotal channels for this measurement are based on a $b \rightarrow s$ transition, such as $B \rightarrow \phi K_S^0$ and $B \rightarrow \eta' K_S^0$, induced by gluon penguin diagrams. These transitions are expected to exhibit small CP violation in the SM, but be highly sensitive to NP contributions [2]. Other interesting channels are charmless B decays, such as $B \rightarrow K\pi$ or $B \rightarrow K\pi\pi$, already studied at LHCb.

Another possible deviation from the SM can be found in the Higgs mechanism: new theories, extending the SM, predict a doublet of charged Higgs bosons, in addition to the neutral one; some discrepancies, that may suggest the evidence of NP, were found in τ processes, such as $B \rightarrow \tau\nu$ or $B \rightarrow D^{(*)}\tau\nu$. Thanks to the τ large mass, other couplings, supposedly to charged Higgs, may be expected in addition to the W boson coupling dictated

in the SM.

The τ sector is also widely explored for the LFV, lying in $\tau \rightarrow l\gamma$ processes, and the measurements of its $(g-2)$ factor and electric dipole momentum.

Non-flavor related NP program

Other interesting subjects at Belle II, that are not directly related to flavor, are the study of quarkonia states, that contributes to the further understanding of low-energy QCD, and the research in the dark sector:

- dark gauge bosons, that can either decay in visible (SM), e.g. $e^+e^- \rightarrow Z' \rightarrow \mu^+\mu^-$ with Z' dark mediator [4], or in invisible (dark) channels;
- axion like particles, dark matter candidates in final states via missing mass measurements, e.g. $e^+e^- \rightarrow a\gamma$, $a \rightarrow \gamma\gamma$ [5].

of through direct measurements that might reveal interactions through new gauge bosons that may decay in either visible SM particles or in invisible states of dark matter candidates.

1.3 *B* factories

An important field to look into to investigate the SM limits and perform neat precision measurements is the heavy flavour sector, that still shows tensions with the SM theoretical predictions, as QCD non perturbative contributions are progressively negligible with higher masses; an emblematic example of tensions with SM predictions is the semitauonic decay $B \rightarrow D^{(*)}\tau\nu_\tau$ [6], whose the Branching Ratio of the decay, accessible from the study of

$$R(D^{(*)}) = \frac{BR(B \rightarrow D^{(*)}\tau\nu_\tau)}{BR(B \rightarrow D^{(*)}l\nu_l)}$$

shows disagreements with the SM predictions of 2.0σ for $R(D) = 0.0440 \pm 0.058 \pm 0.042$ and of 2.7σ for $R(D^*) = 0.0332 \pm 0.024 \pm 0.018$. To achieve the ambitious goal, a valid choice lies in the *B* factories.

The idea of *B* factories is based on the achievements of different groups in the early '80s that show that the CKM parameters are accessible to test the *CP* violation:

- *B* mesons physics defined at CLEO experiment, impressive success given the few tens of events detected;

1.3. B FACTORIES

- B mesons lifetime measured at SLAC [8];
- $B^0 - \bar{B}^0$ mixing rate measured at ARGUS, DESY [9].

Years later, the Belle and BABAR collaborations, at KEKB and PEP-II respectively, measured a rate of one million $B\bar{B}$ mesons per day thanks to the high luminosity of $2 \times 10^{33} \text{cm}^{-2}\text{s}^{-1}$ and $3.4 \times 10^{33} \text{cm}^{-2}\text{s}^{-1}$, measuring CP violation in numerous channels and confirming the SM picture of the CP violation origin [7].

Catching up with Belle and KEKB legacy, the SuperKEKB accelerator is tuned at the center-of-mass energy of the $\Upsilon(4S)$, an unflavored $b\bar{b}$ strong resonance of mass $m_{\Upsilon(4S)}=10.58\text{GeV}/c^2$, which is the lightest particle above the threshold for a $B\bar{B}$ pair production. SuperKEKB is designed to reach a nominal luminosity of $6.5 \times 10^{35} \text{cm}^{-2}\text{s}^{-1}$, around 30 times larger than the KEKB one ($2.1 \times 10^{34} \text{cm}^{-2}\text{s}^{-1}$), that, together with a highly efficient detector, provides a totally known initial state and a large sample of $B\bar{B}$ pairs to carry out indirect searches for NP signatures.

The energy asymmetry between the e^+ and the e^- beams, being 4GeV and 7GeV respectively, results in a Lorentz boost of $\beta\gamma = 0.28$, which is one third smaller than the Belle boost of $\beta\gamma = 0.425$ but still sufficient to allow B or D mesons to travel a significant distance, useful to measure their properties, e.g lifetime, mixing parameters or CP violation. The total cross section of e^+e^- at $\sqrt{s} = 10.58\text{GeV}$ for the channels searched for at Belle II is displayed in table 1.1 showing that B factories are as a matter of facts τ and charm factories, as the cross section for the $\Upsilon(4S)$ is comparable to those of $\tau^+\tau^-$ and $c\bar{c}$ productions.

$e^+e^- \rightarrow$	$\sigma[nb]$
$\Upsilon(4S)$	1.11
$u\bar{u}$	1.61
$d\bar{d}$	0.40
$s\bar{s}$	0.38
$c\bar{c}$	1.30
e^+e^-*	300
$\mu^+\mu^-$	1.15
$\tau^+\tau^-$	0.92

Table 1.1: Cross sections of e^+e^- at $\sqrt{s}=10.58\text{GeV}$; (*) the $e^+e^- \rightarrow e^+e^-$ process is measured using the selection criteria on the polar angle $10^\circ < \theta_e^* < 170^\circ$ and $E_e^* > 0.15\text{GeV}$.

The $\Upsilon(4S)$ ($J^{PC}=1^{--}$) decays mainly in a coherent state of $B\bar{B}$ pairs in P wave with a $\text{BR}(\Upsilon(4S) \rightarrow B\bar{B}) \simeq 96\%$, with equal probability of decaying

1.3. B FACTORIES

either in $B^0\bar{B}^0$ or in B^+B^- , and no fragmentary particles: this implies that the initial state is known precisely. In the $\Upsilon(4S)$ frame the B mesons are produced basically at rest with a Q -value of $Q \simeq m_{\Upsilon(4S)} - 2m_B \simeq 19\text{MeV}$, corresponding to a momentum of $p_B^* \simeq 300\text{MeV}/c$: this means that, in the laboratory frame, the two B 's have almost the same direction of the boost.

Since the two B 's are entangled, it is possible to find out the flavor of one of them through the *flavor tagging* technique, that consist in measuring the features of its decay products (e.g. the charge of the lepton produced in semileptonic channels): this B meson is identified as B_{tag} and allows to infer the flavor of the other B , which is defined as B_{sig} , or B_{CP} . The B_{sig} decay vertex, where the B meson decays in a CP eigenstate, is reconstructed exclusively: the best channel to look for is called "Golden Mode" and corresponds to $B_{sig} \rightarrow J/\psi K_S^0$ (with a CP eigenvalue $\eta_{CP}=-1$) for both quantity and quality, as the J/ψ is a narrow resonance and may decay in a lepton pair l^+l^- (BR=6%), whose invariant mass is easy to measure: at high luminosity the narrow width allows precision measurements through an easy background suppression. This decay is described by two different Feynman diagrams (fig.1.3), that have the same phase, thus it is not affected by the so called "adronic uncertainty", resulting in a particularly clean channel. One

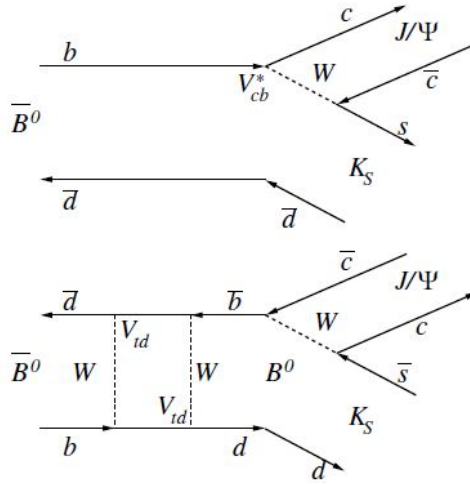


Figure 1.3: Diagrams of the golden channel, used for the measurement of $\beta \setminus \phi_1$: the interfering terms contains $V_{cd}^* V_{cb} V_{td}^* V_{tb}$ [7].

of the main benefits of a B factory is the measurement of the time-dependent CP violation by the extraction of the time difference Δt between the decay times of the two B mesons (fig.1.4), allowing the measurements of:

$$A_{CP}(t) = -\eta_{CP} \sin 2\beta \sin(\Delta m \Delta t) \quad (1.9)$$

1.3. B FACTORIES

Δt is correlated to the distance between the B 's decay vertices $\Delta z \sim \mathcal{O}(100\mu\text{m})$ and the Lorentz boost, as $\Delta t \approx \Delta z/\beta\gamma c$, so, to enhance precision measurements on the time difference between the two decays, there needs to be an improvement on the vertex measurement precision at Belle II with respect to the resolution on Δt as Belle. This improvement is achieved thanks to the PiXel Detector, described in section 2.2.

The high luminosity available at SuperKEKB, in addition to unprecedented precision in CP violation measurements will allow to explore many rare processes that could show effects of physics beyond the SM.

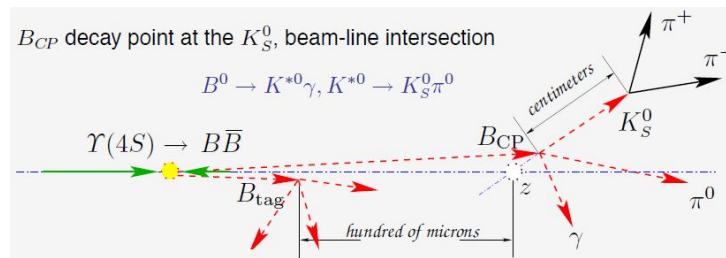


Figure 1.4: Schematic representation of a $B\bar{B}$ event; taken from [27].

Chapter 2

Belle II & SuperKEKB

In this chapter an overview of the SuperKEKB collider is given, with particular attention to the bunch crossing features and the sources of background; then, the whole Belle II detector and its purposes are described. In the final sections the Belle II trigger and the tracking algorithm are introduced to lay the foundations for the discussion of the thesis work.

2.1 SuperKEKB accelerator

The SuperKEKB accelerator [2, 10, 14] is an asymmetric electron-positron collider, shown in fig.2.1, that is redesigned from the previous accelerator, KEKB host of the Belle experiment; it is made up of a linear accelerator (LINAC), two rings, one of 7GeV for electrons (high-energy ring, or HER) and one of 4GeV for positrons (low-energy ring, or LER), and a damping ring (DR) of 1.1GeV to keep the emittance of the injected positron beam under 4nm.

The two beams are tilted and have an angle of $2\phi_c=2\cdot 41.5\text{mrad}$ at the Interaction Point (IP), approximately 4 times larger than the KEKB crossing angle (fig.2.2). The Belle II collaboration set the goal to reach the target luminosity of $6.5 \times 10^{35}\text{cm}^{-2}\text{s}^{-1}$ and integrate a total of 50 ab^{-1} . Many SuperKEKB components and parameters were modified, or even developed from the very beginning with respect to KEKB. Among the new components, there are an electron injection gun, the target to produce positrons, and the damping ring for the positron beam; moreover the radiofrequency (RF) and the vacuum system have been upgraded and an innovative focusing system has been located nearer the IP.

For what concerns the enhancement of the parameters, the vertical β_y^* function at the IP and the bunch length σ_z have been modified down to

2.1. SUPERKEKB ACCELERATOR

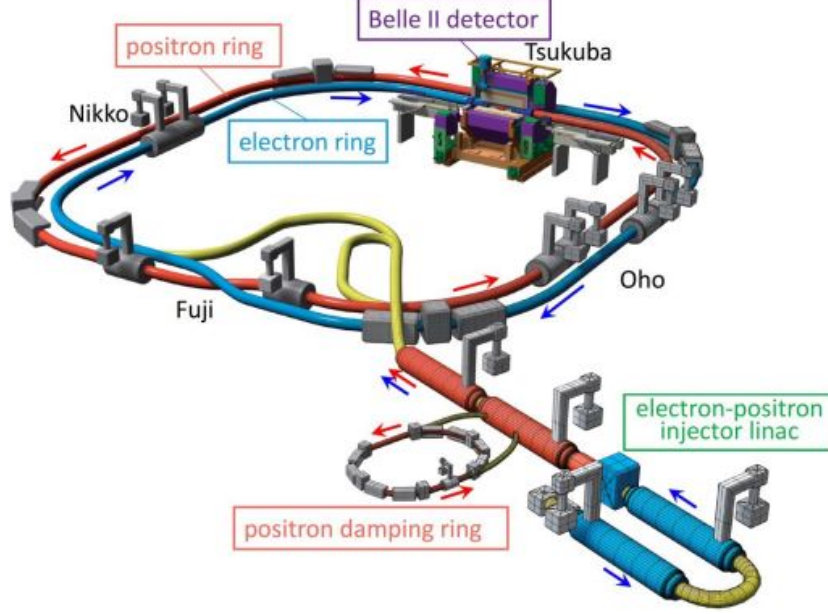


Figure 2.1: SuperKEKB collider; taken from [13].

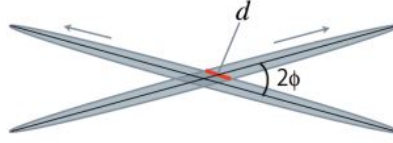


Figure 2.2: Beam collision in the nano beam scheme; taken from [13].

270-300 μm , that reduces the vertical beam size σ_y to 60nm, and 5-6mm respectively: these changes are required by thanks to the application of the *nano-beam* scheme (fig.2.2), conceived for the SuperB project [11] at first, but they are constrained since the excessive reduction of β_y^* (of σ_y consequently) under the σ_z value causes the so-called hourglass effect [12], that results in a degradation of the luminosity. Another improvement regards the beam currents, that have been increased to 3.6A for the LER and to 2.6A for the HER to reach the design luminosity, that can be expressed as:

$$L = \frac{\gamma_{\pm}}{2er_e} \left(1 + \frac{\sigma_y^*}{\sigma_x^*}\right) \left(\frac{I_{\pm}\xi_{y\pm}}{\beta_y^*}\right) \left(\frac{R_L}{R_{\xi_{y\pm}}}\right) \quad (2.1)$$

where + and - refer to positrons and electron respectively, γ is the Lorentz factor, r_e is the classical radius of electron, σ^* is the beam dimension at the IP on the vertical (y , assumed to be the same for the two beams) and on

2.1. SUPERKEKB ACCELERATOR

the horizontal (x) planes, I is the beam current, ξ is the vertical beam-beam parameter, that also keeps track of horizontal parameters such as the bunch length, and R_L and R_ξ are the luminosity and the beam-beam parameter reduction factors. The beam-beam parameter ξ can be expressed as:

$$\xi_{y\pm} \propto \frac{N_{\mp}\beta_y^*}{\sigma_x\sigma_y} \quad (2.2)$$

and describes the effect that the electromagnetic field of a bunch has on the opposite one, with N number of particles in the bunch. The main design features of SuperKEKB are displayed in table 2.1.

	KEKB	SuperKEKB
E (LER/HER)[GeV]	3.5/8	4/7.007
$\beta\gamma$	0.43	0.28
2ϕ [mrad]	22	83
RF [MHz]	508.9	508.9
nominal L [cm ⁻² s-1]	2.1×10^{34}	6.5×10^{35}
β_{IP} (x/y)[mm]	1200/5.9	32/0.27 - 25/0.30
I (HER/LER)[A]	1.64 / 1.19	3.60 / 2.60
σ_x (HER/LER)[μ m]	147 / 170	10.1 / 10.7
σ_y [nm]	940	48-62
σ_z (HER/LER)[mm]	7.0	6.0/5.0
N (HER/LER)	6.47 / 4.72×10^{10}	9.04 / 6.53×10^{10}

Table 2.1: Comparison between the achieved features of KEKB and the design features of SuperKEKB.

2.1.1 Bunch crossing

The RF dictates the frequency of the collisions, given that the bunch crossing is synchronized between the two beams, each counting 2503 **buckets** [13]; it operates at a frequency of 508.9MHz [13], meaning that the minimum time separation between two consecutive buckets is 2ns. However, there is the **filling pattern** in fig.2.3 to consider: not all the buckets are filled (the filled buckets are called **bunches**), therefore the time separation between two consecutive collisions may be a multiple of 2ns [15]. Moreover, because of machine needs, some sections along the rings are empty. The bunch crossing peculiar structure can be seen in the plots of the true time of an **event**, i.e. an e^+e^- collision, with respect to the trigger time, fig.2.4. The plot in fig.2.4 keeps track of the phase of two colliding bunches and shows the bunch

2.1. SUPERKEKB ACCELERATOR

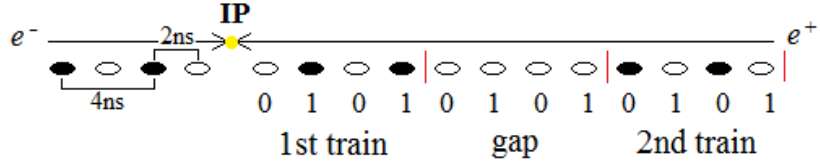


Figure 2.3: Visual distribution of the buckets in SuperKEKB. The even buckets are "0" and the odd ones are "1"; the white buckets are empty, while the black ones are filled (bunches).

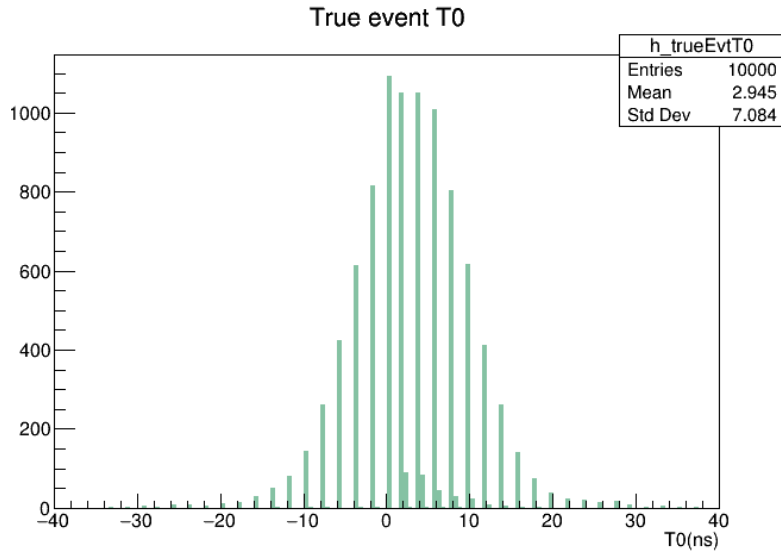


Figure 2.4: Distribution of the true time of an event for simulated $B^0\bar{B}^0$ events with no beam background.

crossing time integrated over a turn of the machine. After the first *train* of buckets, it can happen that the second one is shifted with respect to the first one: for example, if only even buckets are filled in the first train, and the gap has an even number of buckets, then the first bunch of the second train will be an odd bucket. Therefore, since the plot 2.4 is integrated over a whole turn, the time separation per turn results to be 2ns. The plot has a gaussian shape because of the convolution between the filling pattern and the trigger **jitter**. The time of the trigger is $t = 0$, while an event can occur before or after the trigger time depending on the precision of the trigger, that is $\mathcal{O}(10\text{ns})$.

2.1.2 Beam background

Since SuperKEKB has higher instantaneous performances than KEKB, with smaller beam size and higher beam currents, there is also a higher rate of beam background [16]. It consists, for example, in particles coming from non triggered e^+e^- collisions, generated by the accelerator itself (not at the IP) that cross the detector and increase the **occupancy** on sub-detectors, i.e. the fraction of channels (pixels, strips, etc.) with signal above threshold. There are several sources of the beam background, classified as single beam background, that depends on the individual beam properties (Touschek scattering, beam-gas scattering, synchrotron radiation); luminosity dependent background, due to beam-beam interactions and therefore proportional to the luminosity (Bhabha processes, two photon processes); in addition, there is also the injection background, related to the continuous injection process, necessary to maintain the beam currents constant. For what concerns the Silicon Vertex Detector, the relative contributions of the backgrounds to the occupancy scaled to the nominal luminosity is shown in fig.2.5: the main sources are the two-photon processes and the Coulomb scattering resulting from beam-gas scattering.

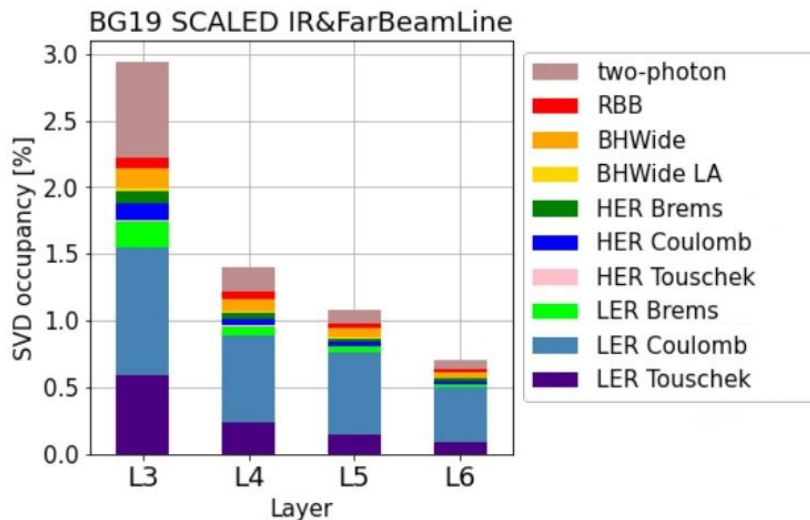


Figure 2.5: Occupancy in the four layers of the Silicon Vertex Detector from the different background contributions; taken from [17].

Touschek scattering

Touschek scattering is an intra-bunch process that sees the particles of a bunch doing Coulomb scattering and deviating their energy from the nominal

2.1. SUPERKEKB ACCELERATOR

bunch energy. This effect is accentuated by the small beam size and has a total rate proportional to:

$$R \propto \frac{n_b I_b}{\sigma E^3} \quad (2.3)$$

with n_b number of bunches, I_b bunch current, σ beam size, and E beam energy. Touschek particles may propagate in the ring and result in showers inside the detector if produced near the interaction point. In order to damp the Touschek effect, some collimators are placed around the ring: horizontal collimation, from both inner and outer sides, reduces losses by stopping those particles that deviate from their established trajectories. The Touschek rate at SuperKEKB was predicted to be 20 times bigger than the KEKB one by scaling the beam size and energy.

Beam-gas scattering

The second effect that contributes to the beam background is the scattering between beam particles and residual gas molecules inside the beampipe. This can either result in Coulomb scattering, that changes the direction of the involved particles, or in bremsstrahlung scattering, that reduces the energy of the beam particles. In SuperKEKB, the total rate is proportional to:

$$R \propto I P_{vacuum} \quad (2.4)$$

with I the beam current, that is two times higher than the one at KEKB, and P_{vacuum} vacuum pressure inside the beampipe of $1nTorr$, similar to KEKB. The rate of the bremsstrahlung scattering is most likely suppressed by the horizontal collimators and thus is negligible with respect to the Touschek effect, while the rate of Coulomb scattering although reduced by collimators can remain significant.

Synchrotron radiation

The Synchrotron radiation (SR) is the third beam-induced background. Since its rate is

$$R \propto E^2 B^2 \quad (2.5)$$

with E beam energy and B magnetic field, the HER beam is its main source. The SR may damage the inner layers of the detector, therefore the beampipe is shaped expressly to prevent SR photons from reaching the VerteX Detector. A thin gold coating is applied inside the beam pipe to absorb residual low energy photons.

Radiative Bhabha process

The photons generated by radiative Bhabha processes

$$e^+e^- \rightarrow e^+e^-\gamma \quad (2.6)$$

propagate mostly along the beam direction and may interact with magnets, producing gamma rays and neutrons. The former are a significant source of background for the Central Drift Chamber and the Time Of Propagation, while the latter are the main background for the K_L^0/μ detector. Because of the high luminosity achieved by Belle II, this background is the most significant.

Two-photon process

The fifth source of background is produced by low-momentum electrons and positrons through the process

$$ee \rightarrow eeee \quad (2.7)$$

that may cause many hits in the detector because of their spiral motion in the magnetic field.

Injection background

Injection-induced background consists in a perturbation of the bunch at the moment of its injection, that results in a higher background rate in the detector. To avoid this, and the saturation of the PiXel Detector bandwidth, a trigger veto is applied after every injection.

2.2 Belle II detector overview

The Belle II detector [14, 18], shown in fig.2.6, has a similar design to the Belle one: some parts, e.g. the sub-detectors structure, the solenoids and the iron return yokes, are taken directly from Belle; however the materials are upgraded to keep up with physics requirements and improve over KEKB performances; the Belle II detector main requirements are:

- excellent vertex resolution, down to $\sim 50\mu\text{m}$;
- high reconstruction efficiency for charged particles of few tens of MeV/c, and a general good resolution for momentum over the entire kinematic range, from 50MeV/c up to 8GeV/c;

2.2. BELLE II DETECTOR OVERVIEW

- high resolution on photon energy and direction;
- advanced PID system to identify electrons, protons, muons, pions and kaons;
- a broad angular acceptance, from 17° to 155° in the polar angle, dictated by the Vertex Detector size;
- fast data acquisition system together with the efficient trigger scheme.

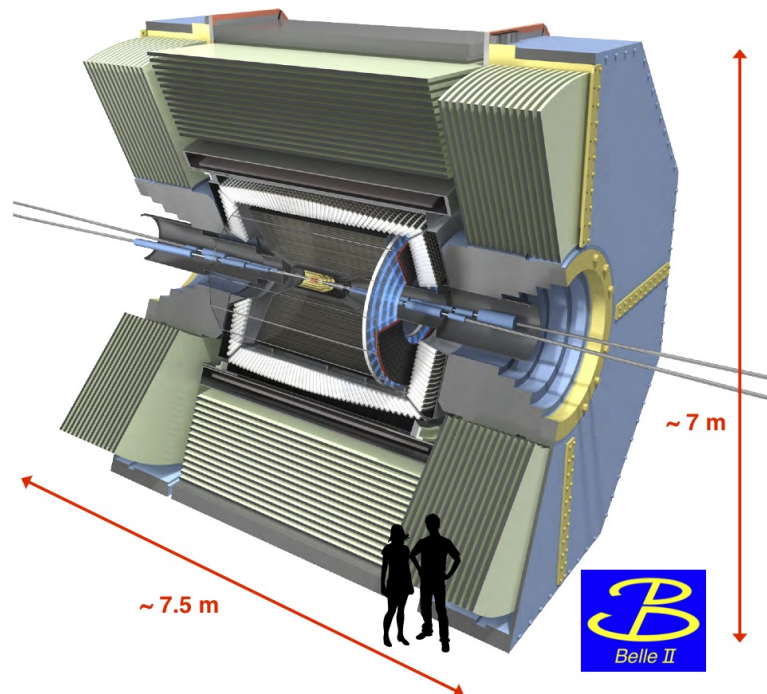


Figure 2.6: General view of the Belle II detector.

The subdetectors from the innermost to the outermost are: the PiXel Detector and the Silicon Vertex Detector forming the Vertex Detector, that takes care of the tracking together with the Central Drift Chamber, that has also a fundamental role in the PID through energy loss measurements; in the barrel region there is the PID couple of subdetectors, both based on the Cherenkov effect, namely the Time-of-Propagation and the Aerogel Ring Imaging Cherenkov Counter; the Electromagnetic Calorimeter focuses on measuring energy and angles of both neutral particles and electrons; similarly to the Belle detector, in Belle II there is a superconducting solenoid

2.2. BELLE II DETECTOR OVERVIEW

that generates a 1.5T magnetic field in the longitudinal direction; finally, the K_L^0/μ detector is the outermost and is dedicated to the measurement and the identification of these particles.

Pixel Detector

The Pixel Detector (PXD), fig.2.7, is the innermost detector at Belle II and the first part of the Vertex Detector. It is composed of two layers (L1 and L2), at radii 14mm and 22mm respectively, of 8 and 12 *ladders*, each containing two monolithic silicon sensors; at the moment, only two ladders of L2 are installed. The pixel sensors, with a pitch of $56\mu\text{m}$ (L1) and $77\mu\text{m}$ (L2) on z , are chosen over the strip ones since they have smaller occupancy and a greater number of channels; plus, they use the DEPFET (DEPlet Field Effect Transistor) technology [20], which allows the use of thin sensors (around $50\mu\text{m}$ thickness) and reduces the multiple scattering, as a consequence. The two layers are respectively 90mm and 123mm long and define the acceptance region in the polar angle, between 17° and 150° .

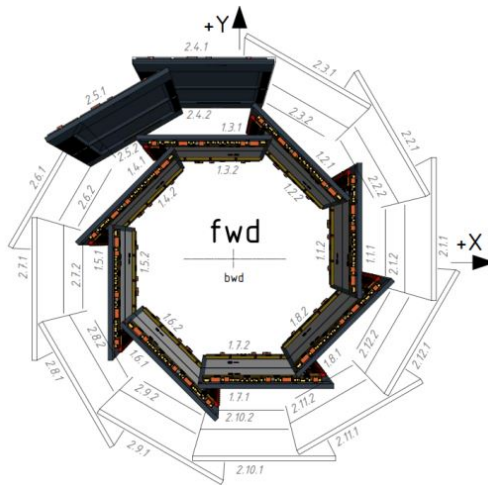


Figure 2.7: Current structure of the PXD; taken from [19].

Silicon Vertex Detector

The Silicon Vertex Detector is the second component of the Vertex Detector, shown in fig.2.9. It comprises four layers of Double Sided Strip Detectors (DSSD) of n-type silicon ($300\mu\text{m}$ thick), each covered with a layer of SiO_2 ; the aluminum strips are oriented either along z (P strips) with a pitch between $50\mu\text{m}$ - $75\mu\text{m}$ or along $r\phi$ (N strips) with a pitch between 160 - $240\mu\text{m}$, and are

2.2. BELLE II DETECTOR OVERVIEW

connected to the APV25, a low noise readout system, described in Chapter 3, that provides charge measurements. The four layers are placed at 39mm, 80mm, 104mm, and 135mm from the IP respectively and are organized as:

- layer 3 (L3): two small rectangular DSSDs;
- layer 4 (L4): two large rectangular and one trapezoidal DSSDs;
- layer 5 (L5): three large rectangular and one trapezoidal DSSDs;
- layer 6 (L6): four large rectangular and one trapezoidal DSSDs;

the trapezoidal sensors are slanted to reduce the material budget, offering a greater coverage in the forward (FW) direction.

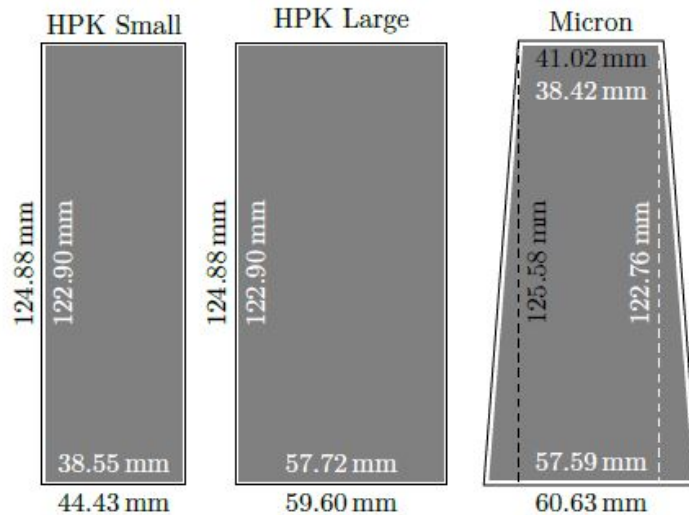


Figure 2.8: Different DSSDs implemented in the SVD; taken from [21].

Together with the PXD, the SVD can reconstruct low p_T tracks and provides the data employed in the tracking. Moreover, it is able to detect the K_s decays outside the PXD volume, that are useful to the tracking of some important channels of B mesons.

Central Drift Chamber

The Central Drift Chamber (CDC) is a cylindrical detector with an inner radius of 160mm from the IP and an outer radius of 1130mm. It contains 14336 tungsten wires, fig. 2.10, divided in 56 layers; the wires can be either "axial", directed along the magnetic field axis, or "stereo", skewed with

2.2. BELLE II DETECTOR OVERVIEW

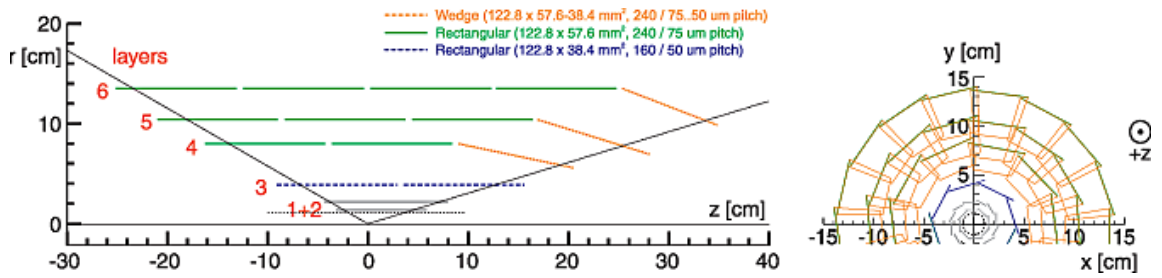


Figure 2.9: Frontal and transverse layout of the SVD; taken from [30].

respect to the previous ones: the combination of both layers allows the reconstruction of the particle helices in the tridimensional space. The Chamber is filled with a mixture composed of He and C_2He_6 in the same percentage that is characterized by an average drift velocity $3.3\text{cm}/\mu\text{s}$ per drift cell. The CDC engages precise measurements of the momenta of charged particles and particle identification through the energy losses in the gas.

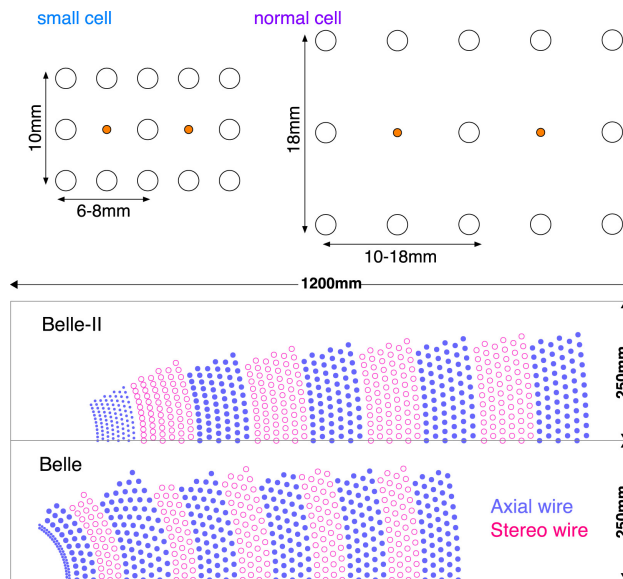


Figure 2.10: CDC wire structure; taken from [18].

Time-Of-Propagation and Aerogel Ring Imaging Cherenkov Counter

The Time-Of-Propagation (TOP) is a Cherenkov detector, shown in fig. 2.11, consisting in a 2.6m long synthetic fused silica (quartz) bar situated in the barrel region. The Cherenkov ring is reconstructed through the arrival time

2.2. BELLE II DETECTOR OVERVIEW

and position of the photons seen by the photo-detectors, placed at the end of the bar, and counted by the 16 channels PMTs with 100ps single photon time resolution. The light conserves the ring image depending on the Cherenkov angle θ_C and propagates through internal reflection; the ring image is then expanded by a wedge crystal. Thanks to the Cherenkov effect, the TOP is able to perform PID basing on different mass hypotheses, starting from different ranges of p_T , e.g. it distinguishes K 's from π 's up to a momentum of 3.5GeV/c.

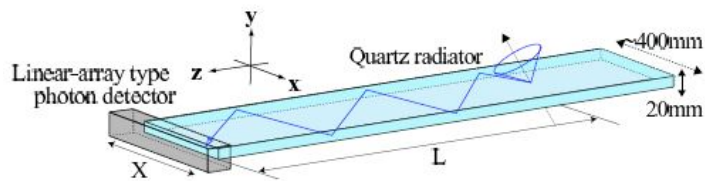


Figure 2.11: Schematic view of the TOP counter; taken from [14].

The second PID sub-detector, the ARICH, fig. 2.12, is located in the end-cap region and consists in: two layers, of 2cm thickness, of aerogel radiator with different refractive indices, $n_1=1.045$ and $n_2=1.055$, where Cherenkov photons are produced, and an expansion region 20cm long, in which the Cherenkov ring is formed; the light is detected by hybrid avalanche photodiodes (HAPD), in which photoelectrons are accelerated by a 8kV potential: the sensors in this region are able to detect single photons with high efficiency and good resolution. The ARICH has been designed to accomplish the identification of charged particles and the distinction of different particles, e.g. electrons, muons and pions, with momentum down to 1GeV/c.

Electromagnetic Calorimeter

To detect neutral particles such as photons or π^0 's and distinguish hadrons from electrons, the Belle II detector is equipped with a high resolution Electromagnetic CaLorimeter (ECL), fig. 2.13. Like the Belle calorimeter, it consists in three regions (barrel, forward and backward) equipped with more than 8000 CsI(Tl) crystals that cover a polar angle range between 12.4° and 155.1° . In absence of background, the ECL performances at Belle II are very similar to those at Belle, e.g. an energy resolution of 4% at 100MeV and 1.6% at 8GeV and an angular resolution of 0.23° for $e^+e^- \rightarrow \gamma\gamma$ processes.

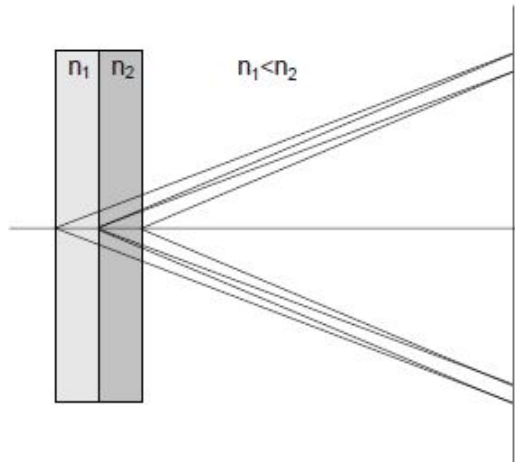


Figure 2.12: ARICH operating principle; taken from [18].

K_L -Muon Detector

The K_L^0 and Muon detector (KLM) in fig.2.14 is taken from Belle and consists in 4.7cm thick iron plates alternated to active detector materials, previously consisting in resistive plate chambers (RCP) at Belle then replaced with silicon photomultipliers (SiPM), chosen to mitigate background effects at Belle II. Its barrel region covers a polar angle range between 45° and 120° and includes 14 iron plates and 15 detector material layers, while the endcaps cover a range from 20° to 45° and from 120° to 155° and includes 14 detector material layers and 14 iron plates.

The K_L^0 's interact in the iron layers generating hadronic showers, similar to what happens in the ECL: the hits on the detector layers that are within 5° between each other are gathered into the same cluster and, if the cluster is aligned within 15° to the neutral cluster detected in the ECL, then they both are associated to a single track; to identify K_L^0 's, the tracks must have hits in two different layers at least within the KLM acceptance.

For what concerns muon identification, the tracks are reconstructed starting from the CDC hits and their energy loss: if the track has a momentum that is at least $0.6\text{GeV}/c$ and crosses at least one detector layer, then the outermost hit is used to extrapolate the track and identify a muon.

Coordinate system in Belle II

The cartesian coordinate system [23] for the Belle II detector is defined as:

- the z -axis coincides to the solenoid axis, and is directed toward the electron beam;

2.2. BELLE II DETECTOR OVERVIEW

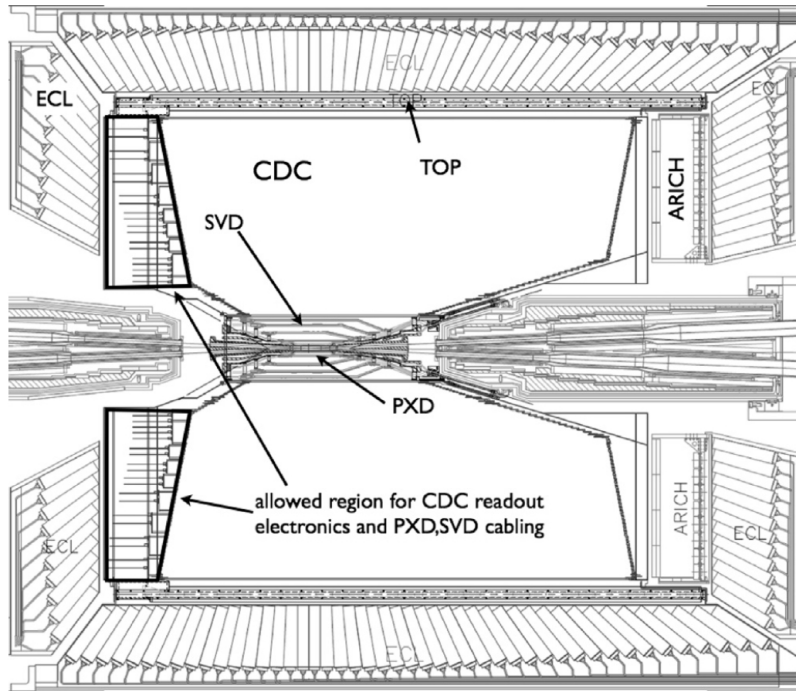


Figure 2.13: Schematic structure of the ECL; taken from [22].

- the x -axis is horizontal and directed from the IP to outside the detector;
- the y -axis is directed upwards from the IP;

The $x - y$ plane corresponds to the transverse plane and defines the bi-dimensional radius ρ , that is the distance from the IP on the transverse plane. The azimuthal angle ϕ and the polar angle θ , that goes from the z -axis to the transverse plane $s = \sqrt{x^2 + y^2}$ are used to describe the direction of the decay products.

2.2.1 Belle II current status

The data acquisition at Belle II started in springtime in 2019. One year later, Belle II recorded the instantaneous luminosity world record value of $2.22 \times 10^{34} \text{cm}^{-2} \text{s}^{-1}$, beating both KEKB, with $2.11 \times 10^{34} \text{cm}^{-2} \text{s}^{-1}$ and LHC, with $2.14 \times 10^{34} \text{cm}^{-2} \text{s}^{-1}$ (2018); almost three years later, in Dec. 2021 Belle II reached the world record value of 2fb^{-1} of daily integrated luminosity, with an instantaneous luminosity value of $3 \times 10^{34} \text{cm}^{-2} \text{s}^{-1}$. Currently, the total integrated weekly luminosity value has reached 340.44fb^{-1} , fig.2.15, of

2.2. BELLE II DETECTOR OVERVIEW

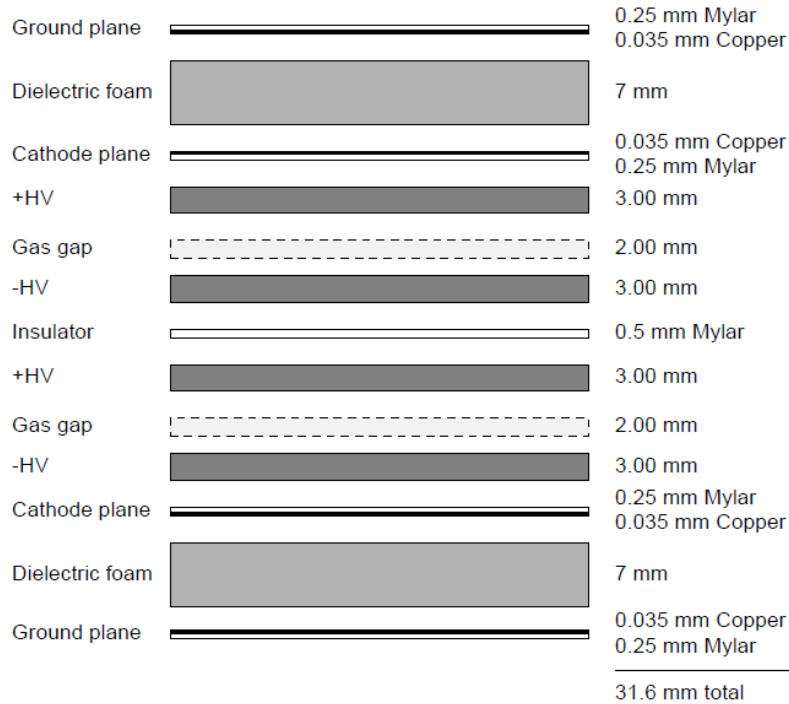


Figure 2.14: Schematic view of the KLM.

which, 75.32 fb^{-1} are recorded between the beginning of March, 2022 and the end of April, 2022, fig.2.16.

2.2.2 Belle Analysis Framework II

The Belle Analysis Framework II (basf2) [24] is the Belle II official software framework that allows both online (data acquisition, data quality monitoring, high level trigger online reconstruction) and offline (offline reconstruction and analysis) use. The different data processing methods are written in independent **modules**, that can be combined in one or more **paths** in the **steering file**, the file that collects and organizes the input and the output data. The modules are written in C++, while the steering files are written in *python3*. The output data are enclosed in ROOT **ntuples**, that store the information in different variables useful for the analysis.

In this thesis, the used ntuple is `SVDEventTOTTreePerformance`, that contains different variables related to the time (event time, cluster time, etc. These variables are discussed in Chapter 4) and to the SVD (number of hits, layers, u - v sides, etc.), useful to give an overview the features of the event before the event time estimate.

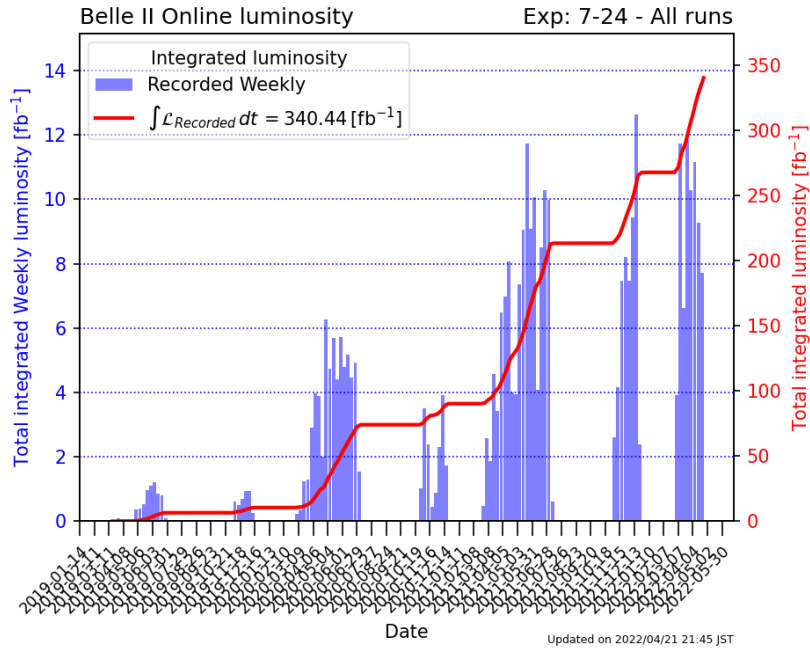


Figure 2.15: Integrated luminosity recorded by the Belle II detector between March, 2019 and April, 2022.

2.3 Trigger

The Belle II experiment has a highly efficient triggering scheme (99% efficiency for $B\bar{B}$ events) for several decays, that minimizes the deadtime between data acquisitions and faces the high background [2]. The trigger system is divided into two parts: the Level 1 trigger, that operates on the sub-detectors hardware part through Field Programmable Gate Arrays (FPGAs) and reduces the rate of incoming events that are provided to the High Level Trigger, the software stage that operates online. In table 2.2 the main processes searched at Belle II at design luminosity are exposed, together with their total cross section and rate.

2.3.1 L1 trigger

The Level 1 Trigger (L1) has an acquisition rate of around 20kHz at nominal luminosity. It is divided in two sub-triggers and a Global Decision Logic (GDL), each with FPGAs to program the logic. The total latency of the trigger system is fixed to about $5\mu\text{s}$. The L1 trigger is required to have:

- a high efficiency for both hadronic and continuum events;

2.3. TRIGGER

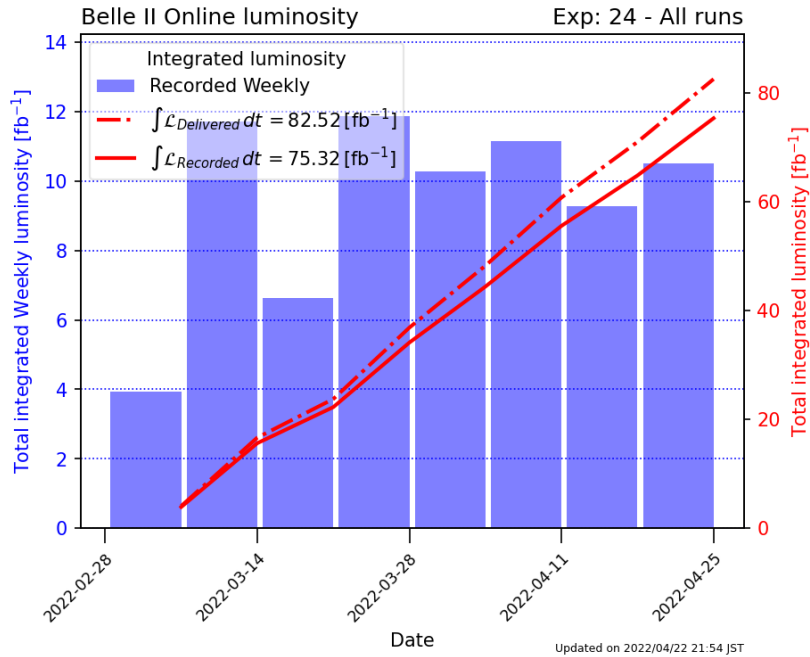


Figure 2.16: Integrated weekly luminosity recorded (continuous line) by the Belle II detector and delivered (dashed line) by SuperKEKB between March, 2022 and April, 2022.

- a maximum rate of 30kHz;
- 10ns timing precision at most (trigger jitter);
- 190ns minimum event separation (corresponding to 6 clocks in 31.805MHz, acquisition frequency of SVD);
- a flexible and robust structure.

The outline of the L1 Trigger is given in the following. It has the task to generate a trigger signal (in $5\mu\text{s}$, meaning that the sub-detectors need to have a buffer for data acquired in this time window) for every interesting physics event and is composed of two sub-triggers, the CDC one and the ECL one:

- CDC sub-trigger: it uses pieces of information about charged particles detected, such as transverse momentum p_T , charge, longitudinal impact parameter, multiplicity, etc. to decide whether an event is interesting or not. Because of the limited solid angle acceptance, it detects the charged particles only in proximity of the IP: $|d_z| \leq 4\text{cm}$ and $|d_r| \leq 4\text{cm}$.

2.3. TRIGGER

Physics process	σ [nb]	Rate [Hz]
$\Upsilon(4S) \rightarrow B\bar{B}$	1.2	960
hadron production from continuum	2.8	2200
$\mu^+\mu^-$	0.8	640
$\tau^+\tau^-$	0.8	640
BhaBha ($\theta > 17^\circ$)	44	350*
$\gamma\gamma$ ($\theta > 17^\circ$)	2.4	19*
other 2γ processes ($\theta > 17^\circ, p_T > 0.1\text{GeV}/c$)	80	15000

Table 2.2: Total cross sections and rates for interesting events at Belle II; (*) the rates have been scaled by a factor 100 due to their large cross sections [2].

- ECL sub-trigger: it is fundamental as the calorimeter can generate fast signals for both neutral and charged particles. It is composed of two different systems: the former is the total energy trigger, sensitive to high electromagnetic deposits, while the latter is sensitive to MIPs and multi-hadronic events with low energy clusters. Moreover, the calorimeter is the only detector that provides information about BhaBha and $\gamma\gamma$, necessary to measure the luminosity.

Together with these two, the L1 trigger collects live stream information from the KLM and the TOP, too; the live stream of data is elaborated by the FPGAs, that matches data to the trigger conditions. The sub-trigger information are sent to the GDL, whose logic distinguish physics events starting from the number of tracks ($\Upsilon(4S)$ has a "three-track logic", while τ -pairs have a "two-tracks" one), and saves less interesting events for the Belle II physics program like BhaBha, $\gamma\gamma$, and μ -pairs events for the calibration.

2.3.2 High Level Trigger

The Data AcQuisition system (DAQ), fig.2.17, uses data that passed the L1 trigger selection coming from all subdetectors except PXD, and sends them to the HLT to perform the full event reconstruction and to decide whether an event is significant or not basing on the physics of the event. Data are transferred to a multi-step front-end electronic scheme that processes and stores them, composed of the Belle2Link, a high speed data transmission link that works on a lower rate than the maximum rate permitted by the bandwidth, the COmmon Pipelined Platform for Electronic Readout (COPPER), the Event Builder, and finally the HLT. Data from all sub-detectors, except the PXD, are collected and compressed in blocks by the Event Builder 1; then

2.3. TRIGGER

this blocks are sent to the HLT that performs the data reduction [25]. The DAQ procedure is shown in fig. 2.17. Schematically, the HLT receives the

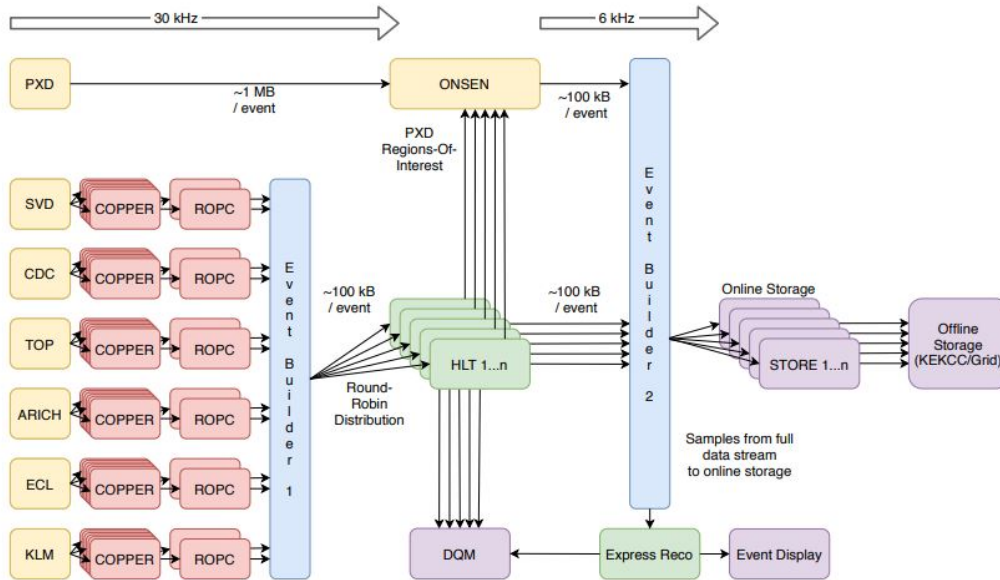


Figure 2.17: Overview of data flow of the Belle II DAQ system; taken from [25].

raw data from the L1 trigger and performs a first reduction, thanks to the application of the Level 3 (L3) filter: the reconstruction has been optimized to be fast (HLT processing output rate is 10kHz at nominal luminosity) to overcome the backpressure problem, which may cause a stopping of online data acquisition, and a consequent loss of events, if the HLT deadtime is too long. The online full reconstruction is finalized only on the events that pass the filter. In addition to the filtering, the HLT classifies the events in different physics skims, applying loose selection criteria to events, e.g. it counts the number of tracks per event; there are different types of skims (hadronic, Bhabha, $\mu\mu$, $\tau\tau$ etc). The final step is to extract the Region of Interest (RoI) on the PXD surface in order to reconstruct low momentum tracks and reduce the bandwidth: the RoIs are extracted by the FPGA based DATA CONcentrator (DATCON) system starting from SVD only data; the ONLINE SElection Node (ONSEN) receives the RoIs and the HLT events that passed the filtering and merges them to send them to the Event Builder 2 for the full event reconstruction.

2.4 Tracking

The tracking algorithm [28] aims to identify the hits on the VXD and CDC layers and to reconstruct and fit trajectories of daughters of short lived particles generated inside the beam pipe at the IP, and daughters of long lived particles produced outside the beam pipe, such as K_s^0 , Λ and converted photons. In addition, it is also used to align the whole detector, in order to obtain unbiased measurements for accurate analyses.

The tracking algorithm works fine for tracks with transverse momentum down to 50MeV/c and its efficiency for charged particles is 95% for events with $p_T = 100\text{MeV}/c$, as shown in fig.2.18. The track of each charged particle

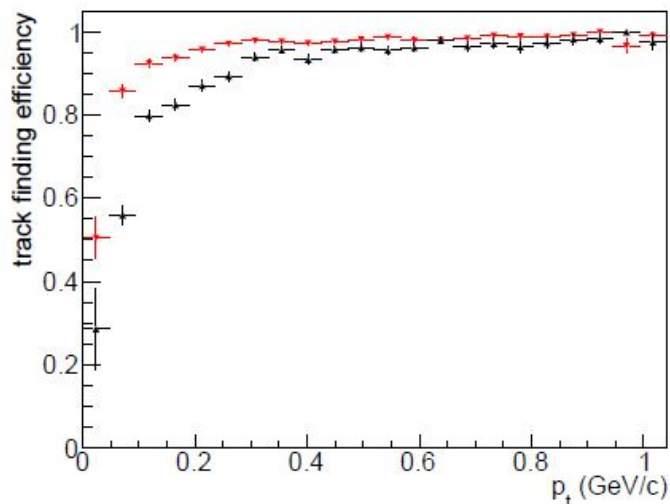


Figure 2.18: Track finding efficiency as a function of transverse momentum for the CDC-only (black) and the full tracking (red) evaluated on simulated $B^0\bar{B}^0$ events; taken from [30].

can be identified by five parameters [2], shown in fig.2.19

- d_0 , the signed distance between the the point of closest approach (POCA, \vec{P}) to the z -axis, whose sign depends on the direction of the angular moment of the particle in \vec{P} , with respect to the magnetic field;
- z_0 , the longitudinal distance between the \vec{P} and the origin;
- ϕ_0 , the angle between the transverse momentum in \vec{P} and the x -axis;
- $\tan \lambda$, where λ is the angle between the total momentum of the track and the transverse plane;

2.4. TRACKING

- ω , curvature of the track whose sign is given by the charge.

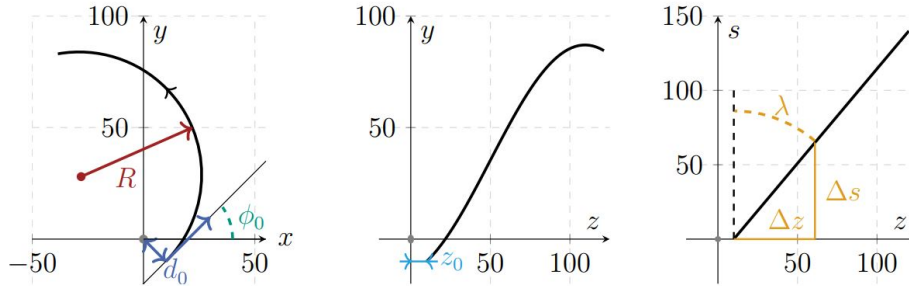


Figure 2.19: View of the trajectory of tracks in the $x-y$ (left), $z-y$ (middle) and $z-s$ (right) projections, where $s = \sqrt{x^2 + y^2}$. All dimensions are in cm. Taken from [28].

The tracking algorithm can be divided into two different steps:

- *track finding*: it consists in the identification of the candidates for a same track applying **pattern recognition** (PR) algorithms to the hits on VXD and CDC. The candidates are then merged together;
- *track fitting*: the reconstructed track is fitted finding the best values for the five track parameters.

The performance of the PR is affected by different factors, such as:

- **occupancy**, the fraction of VXD and CDC channels with a signal above threshold per triggered event, that is affected by the beam background. At nominal luminosity, the number of background hits is greater than signal hits by two orders of magnitude, that means 2% PXD occupancy and 3% SVD occupancy in the innermost layer, and a dominating fraction in the CDC occupancy;
- **multiple Coulomb scattering** and **energy loss** in the material, major for soft particles with $p_T < 200 \text{ MeV}/c$: these particles are usually *loopers* that leave hundreds of hits in the CDC.

When applying the PR algorithm on data, in addition to signal tracks, there can be:

- *fake* tracks: either tracks non corresponding to real particles or tracks that do not belong to the triggered event;

2.4. TRACKING

- *clone* tracks: the PR algorithm associated two different tracks to the same particle, usually a looper;

either way, *fake* and *clone* tracks are mostly discarded depending on their quality indicator and p-value.

For what concerns the tracking in MC simulation [28], two fundamental concepts to evaluate the performance of the PR are:

- *hit purity*, corresponding the fraction of signal hits over the total;
- *hit efficiency*, that is efficiency in the identification of the hits belonging to the same particle.

The algorithm succeeds if the hit purity is higher than 66% and the hit efficiency is higher than 5%. For non signal tracks, if two or more tracks are associated to the same MC track, the one with the highest value is chosen, while the others are called *clones*; if the tracks have the same hit purity, the algorithm chooses the one with the highest hit efficiency. If a PR track has a hit purity under the threshold, it is called *fake* track.

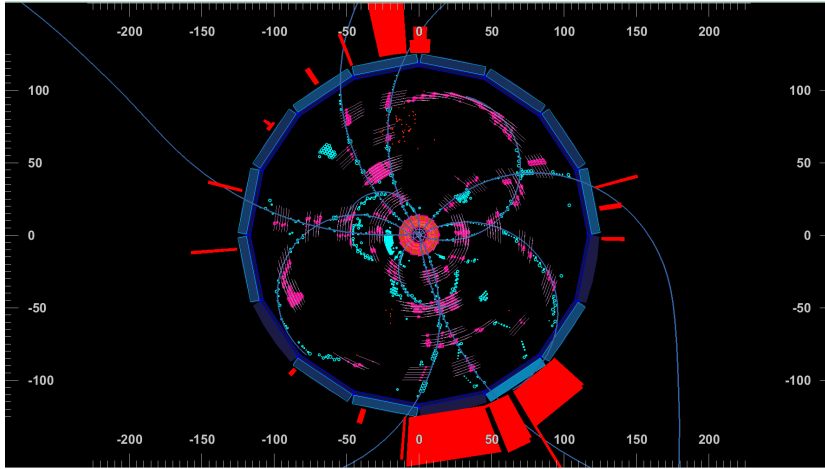
The final fit of the tracks, after the PR stage, is based on the Runge-Kutta-Nystrom [29] method and takes into account multiple scattering, energy loss and the effect of the magnetic field.

2.4.1 Typical $B^0\bar{B}^0$ and $\tau^+\tau^-$ events

The tracking algorithm is a fundamental step for the full event reconstruction: it is possible to characterize different events based on the number of the number of signal tracks or other tracks variables. The discussion is now focused on the characterization of $B^0\bar{B}^0$ (fig.2.20) and $\tau^+\tau^-$ events, basing on the SVD information, which is fundamental since in this thesis the time of an event (i.e. e^+e^- collision) is estimated starting from SVD hits.

On 1000 simulated $e^+e^- \rightarrow \Upsilon(4S) \rightarrow B^0\bar{B}^0$, the tracking reconstruction succeeds in finding 10770 correctly reconstructed candidates that underwent the truth matching, as shown in fig.2.21 (left). The correctly reconstructed candidates are sorted per flavor using the PDG numbers associated to each particle and respective antiparticle; the average composition of a $B^0\bar{B}^0$ event is displayed in table 2.3.

Out of 10770 correctly reconstructed candidates, only 10405 particles cross the SVD, being the 96.6% of the total, while the remaining 365 supposedly correspond to daughters of long-lived particles that decay outside the SVD volume; among the candidates seen in SVD, only 10149 form clusters, that corresponds to an efficiency of 97.5%, as in fig.2.21 (right); the 256

Figure 2.20: Event display of a candidate $B\bar{B}$ event; taken from [27].

particles	mean	std dev
π^\pm	7.6	3.0
K^\pm	1.3	1.1
e^\pm	0.8	0.9
μ^\pm	0.7	0.8
$p\bar{p}$	0.4	0.7

Table 2.3: Average composition of a simulated $B^0\bar{B}^0$ event.

tracks left over, corresponding to the 2.5%, probably particles crossing the inactive volume of the SVD. As expected [28], a $B^0\bar{B}^0$ event is composed of 10 charged tracks on average, turning out to be the event type with the highest track multiplicity; moreover, the average number of hits per track is 8, as shown in fig.2.21 (right), meaning that the particles cross the four ladders of SVD, each with two sides, while for a few tracks more than 8 hits are counted: these could be either particles that cross the overlaps of the layers (fig.2.22), or the so-called *loopers*, low $|p_T|$ tracks which trajectory results in a loop, having a smaller curvature radius, according to eq.4.4.

When signals on different adjacent strips are reconstructed as a single hit, then a cluster is formed: the average number of signal clusters, i.e. clusters associated to signal tracks, per event is 80, as shown in fig.2.23, as expected for the number of charged tracks (10) times the number of hits per track (8).

For what concerns τ -pairs, for 1000 $e^+e^- \rightarrow \tau^+\tau^-$ simulated events, the average number of charged tracks per event is ~ 2.5 , that varies with the decay

2.4. TRACKING

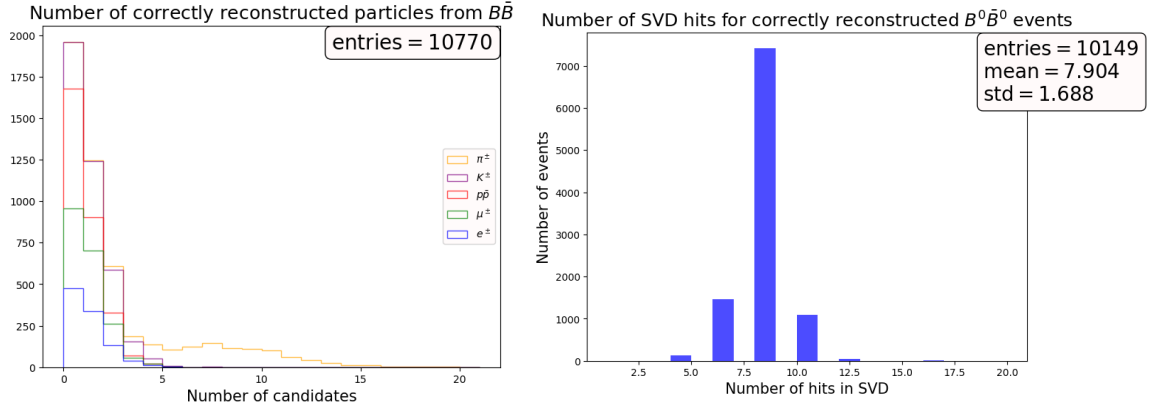


Figure 2.21: (left) Distribution of the number of correctly reconstructed candidates in 1000 $B^0\bar{B}^0$ events; (right) distribution of the number of tracks hits in SVD for $B^0\bar{B}^0$ events.

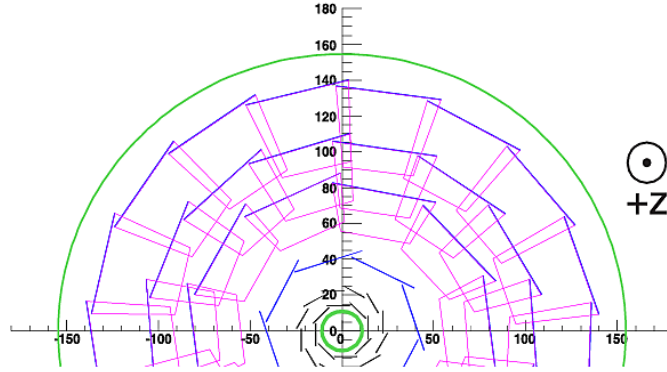


Figure 2.22: Overlaps between the sensors of a same layer, SVD section view; taken from [30].

channel (one prong, three prongs, leptonic, etc.). τ -pairs are the events with the lowest track multiplicity ($\mu^+\mu^-$ events excluded).

The correctly reconstructed candidates are sorted per flavor: the average composition of a $\tau^+\tau^-$ event is displayed in table 2.4.

Over the total of 2556 reconstructed tracks, only 2514 form clusters in SVD (fig.2.24), corresponding to an efficiency of 98.4%. Like in $B^0\bar{B}^0$ events, tracks from $\tau^+\tau^-$ events have on average 8 hits per track in SVD as shown in figure 2.25 (left). Therefore, the number of signal clusters per $\tau^+\tau^-$ event is ≈ 22.6 , as shown in fig.2.25 (right).

2.4. TRACKING

particles	mean	std dev
π^\pm	1.68	1.36
e^\pm	0.46	0.66
μ^\pm	0.32	0.51
K^\pm	0.05	0.23
$p\bar{p}$	0.04	0.25

Table 2.4: Average composition of a simulated $\tau^+\tau^-$ event.

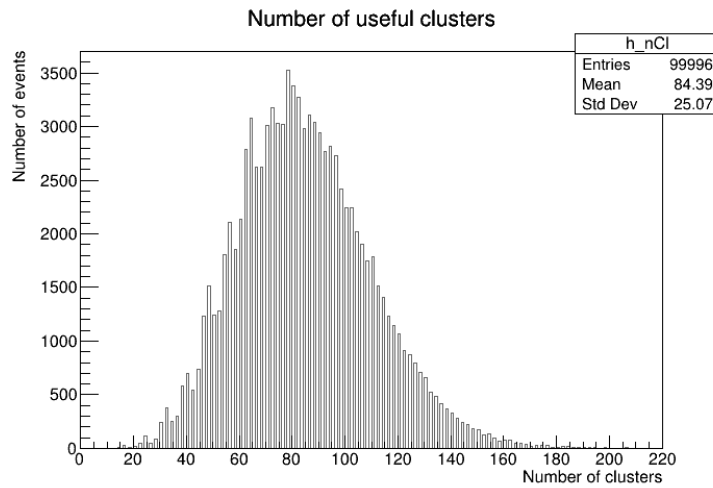


Figure 2.23: Number of signal clusters in SVD for $B^0\bar{B}^0$ events.

2.4. TRACKING

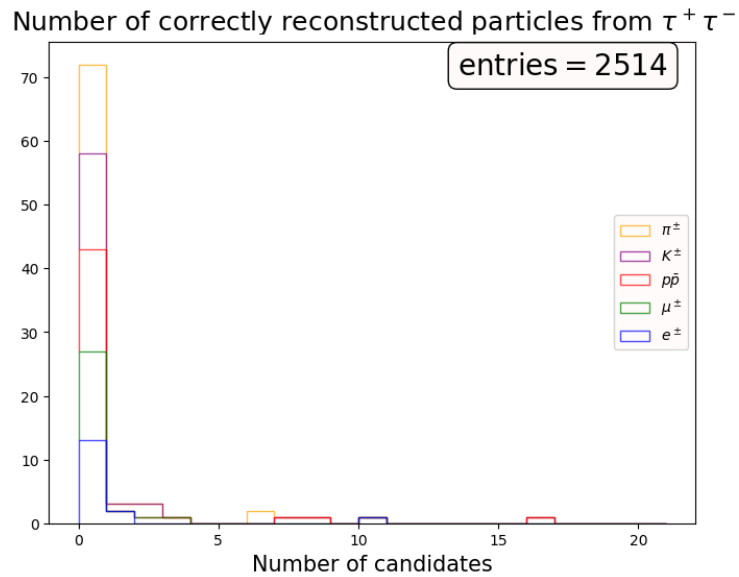


Figure 2.24: Number of correctly reconstructed candidates in 1000 $\tau^+ \tau^-$ events.

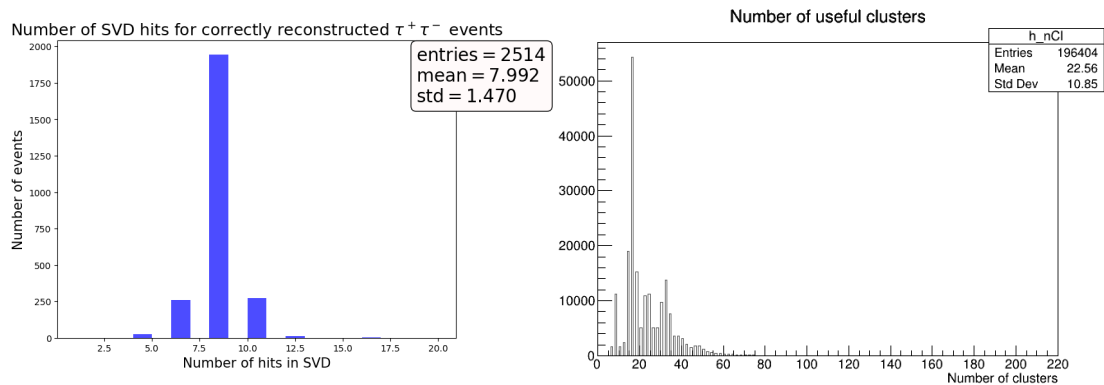


Figure 2.25: (left) Number of track hits in SVD for $\tau^+ \tau^-$ events; (right) number of clusters in SVD for $\tau^+ \tau^-$ events.

Chapter 3

Time Measurements

In anticipation of the nominal luminosity, various studies are being carried out to improve the performances of the timing system, fundamental to reach the reconstruction performance needed for high precision measurements. The high beam background expected at high luminosity needs dedicated rejection tools, that are also based on timing. The Silicon Vertex Detector is a fundamental sub-detector for the beam background rejection, thanks to a hit detection efficiency higher than 99% in most sensors and a resolution on cluster time measurements between 2 and 4ns. The timing problem also impacts the triggering system, since the algorithm that computes the time of an e^+e^- collision (`EventT0`), takes up to $\sim 83\%$ of the HLT processing time at the current luminosity. It is therefore of great interest to develop a faster algorithm to find the event time, exploiting the excellent time resolution of the SVD. In this chapter, the functioning of strip detectors, SVD data acquisition and cluster reconstruction are discussed to provide a full picture and to lay the ground for the event time estimate with the SVD; the two algorithms to compute the event time with the CDC and the TOP are also briefly presented.

3.1 Motivations for time measurements

Time measurements constitute a fundamental step at the base of the full event reconstruction: as a matter of fact, precision analyses carried out at Belle II rely on an efficient distinction of signals from the high beam background. For this purpose, a fast and efficient timing system is essential: SVD, with a hit detection efficiency of 99% (fig.3.1 [35]), has been designed to cope with a high rate of background ($1.5\text{MHz}/\text{cm}^2$ at nominal luminosity [30]) with the goal to efficiently reject off-time hits with respect to the time of

3.2. STRIP DETECTORS

a e^+e^- collision, corresponding to background particles or to particles from previous bunch crossings, before the tracking stage.

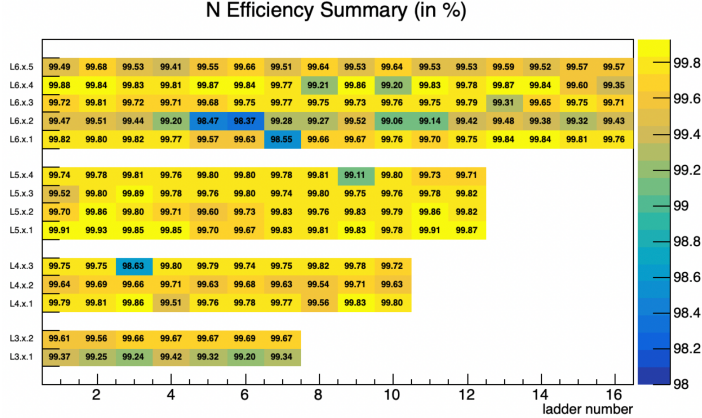


Figure 3.1: SVD hit detection efficiency on N strips: only on few sensors it is under 99% affected by statistical-only error ($< 0.05\%$); taken from [26].

At the tracking stage, SVD is crucial to find tracks with low transverse momentum, such as the slow pions in $B \rightarrow D^{*+} X$, $D^{*+} \rightarrow D^0 \pi_s^+$, since the CDC-only efficiency is 80% at $p_T = 100\text{MeV}/c$ (fig.2.18).

In general, hit time measurements in other sub-detectors are needed to perform correct PID algorithms for calibration, reconstruction and analysis.

For what concerns the time of an e^+e^- collision, contribution from CDC, ECL, and TOP are stored as `TemporaryT0` data objects in the `eventT0` class, each calculated with a specific algorithm; CDC and TOP `EventT0` estimates are briefly described in the section 3.6. At the moment, the `eventT0` algorithms, among many others, are being optimized to improve and speed up the tracking reconstruction, that takes up to the 83% of the HLT processing time [31, 32], aiming to prepare the DAQ system for a higher rate given by the increasing luminosity: the slowest module of the HLT reconstruction, `FullGridChi2TrackTimeExtractor` (abbreviated as `FullGrid` from now on), takes up to 30ms per event (fig.3.2). Currently, different solutions to overcome the slowdown in the HLT operation are proposed, together with the improvement of `EventT0` performance and algorithms.

3.2 Strip detectors

As stated in section 2.2, the Silicon Vertex Detector is made of semiconductor material (n-type Si substrate) and is composed of four layers, for a total of

3.2. STRIP DETECTORS

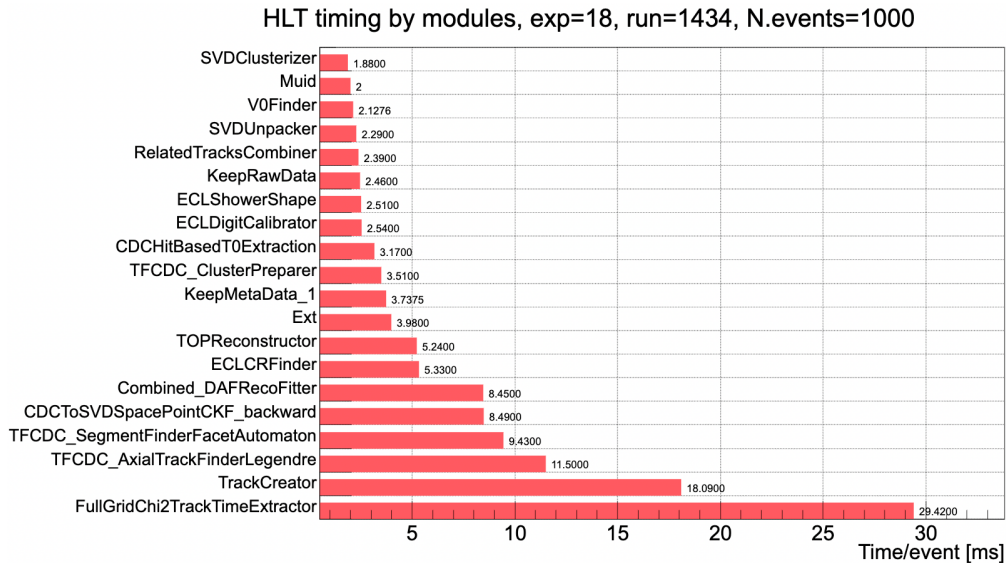


Figure 3.2: Execution time of various modules in the HLT online reconstruction on data; taken from [32].

172 silicon sensors. The detector itself is a double-sided strip detector [33, 34], with two sets of orthogonal strip (P, N) implanted on each sensor (details are listed in table 3.1): this configuration, shown in fig.3.3, is fundamental to provide precise measurements of the position of a crossing particle thanks to the acquisition of the two coordinates.

	Small	Large	Trapezoidal
# of P strips	768	768	768
# of N strips	768	512	512
P strip pitch	50 μ m	75 μ m	50-75 μ m
N strip pitch	160 μ m	240 μ m	240 μ m
thickness	320 μ m	320 μ m	300 μ m

Table 3.1: Specifications of DSSDs strips [34].

When a particle crosses the detector, the ionization of the semiconductor material occurs: electrons and holes start drifting through the electric field created by an external bias, as in fig.3.4, and, as soon as the charge carriers start moving, an electric signal is induced on the strips. Each strip, through an aluminum electrode, is connected to one amplifier channel of the APV25 ASIC, originally developed for the CMS experiment, that provides a measurement of the charge deposited on the strips.

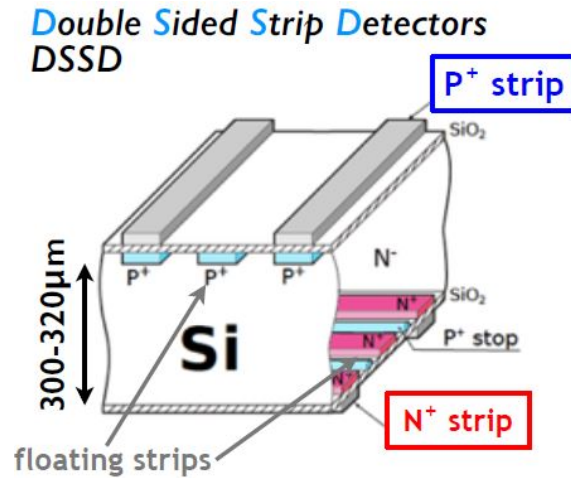


Figure 3.3: Representation of the passage of an ionizing particle through a DSSD; taken from [34].

SVD coordinate system

In addition to the global coordinate system, defined for the Belle II detector, the SVD reconstruction software identifies a local frame for each sensor given by the triplet (u, v, w) , that originates from the center of the sensor, where:

- u is directed along the global $r\phi$;
- v is directed along the global z ;
- w points away from the IP in the direction perpendicular to the sensor.

In this local frame, u is measured by the P strips, while v is measured by the N ones (fig. 3.3); since the P strips on the forward sensors on layers 4-5-6 are not parallel to one another because of trapezoidal shape of the sensors, the u coordinate of a hit can only be established if the v one on the same sensor is already known.

3.3 SVD data acquisition

The SVD online data acquisition system [30] is composed of two key components: 52 Flash Analog to Digital Converter (FADC) boards and 1748 front-end APV25 readout chips [36]. The Front-end Timing SWitch (FTSW) system transmits the Belle II clock and trigger to the SVD, in particular to the FADC boards through the FADC_Controller interface: the upcoming clock frequency is reduced from 127MHz to 31.8MHz, frequency of the

3.3. SVD DATA ACQUISITION

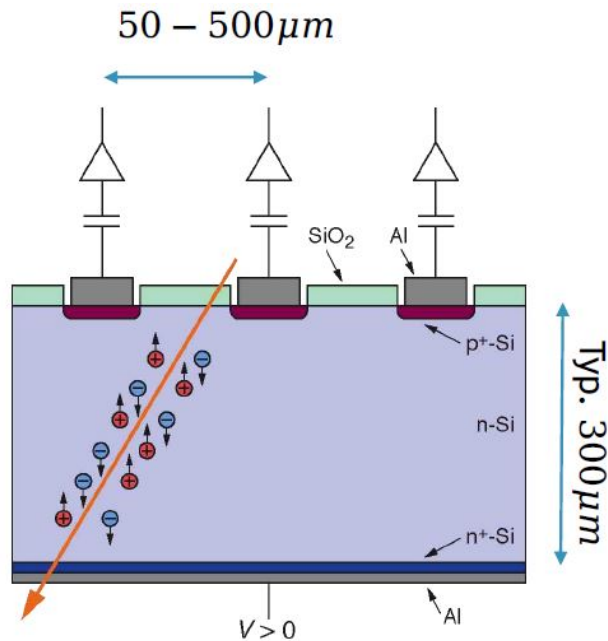


Figure 3.4: Passage of a particle through a silicon sensor; taken from [34].

FADC and APV25 boards. The APV25 operates in a multipeak mode to provide the data frames called samples: each sample is stored in a cell of an APV25 buffer. Each APV channel, each one linked to a strip, has 192 cells of analog pipeline to store the samples of the waveform with a frequency of 31.8MHz. SVD fixes the maximum latency to the DAQ system ($\sim 5\mu s$). When the trigger signal arrives, the APV25 provides 6 samples, 31.4ns apart, corresponding to the triggered event, as shown fig.3.5.

Two time frames can be conceptually identified:

- SVD reference system with $t_{SVD} = 0$ corresponding to the first sample of the APV25;
- global reference system with $t_{glob} = 0$ corresponding to the arrival of the trigger.

The two frames are synchronized and it is possible to switch between them by performing a simple temporal translation. Since the APV25 has a frequency 4 times lower than the trigger clock, the FADC registers the trigger arrival time within one APV25 clock and stores it in the Trigger Bin (TB=0,1,2,3) that represents in which quarter of APV25 clock the trigger signal is received (e.g. 0 indicates the first quarter of the APV25 clock).

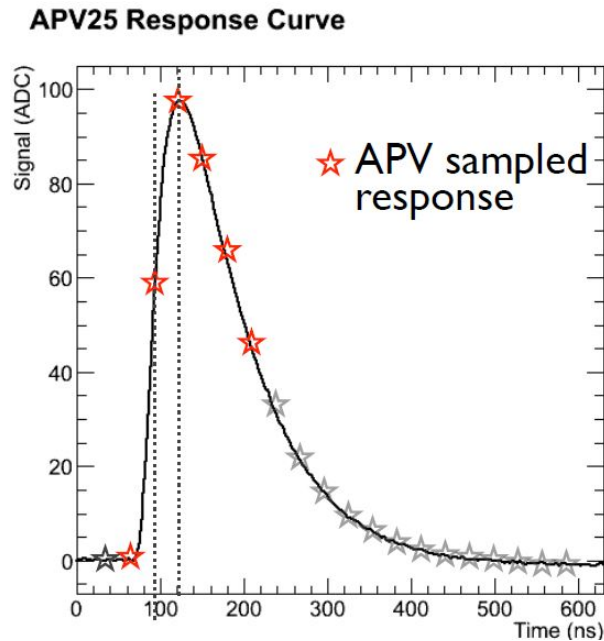


Figure 3.5: Response curve of an APV25 channel.

SVD stores one sample per APV25 clock front (31.8MHz, or 31.4ns) in its own reference system starting at $t_{SVD}=0$: the first sample corresponds to the 0 in the SVD time frame, and the whole set of samples has to be translated in the global time reference frame to be used in the tracking stage.

The FADC boards, each connected to ~ 35 APV25 chips, proceeds to:

- digitize the signal;
- remove the strip pedestal to the raw signal;
- apply the common mode correction, which consists in the subtraction of the average amplitude, calculated for 32 consecutive strips, from individual non-masked strips and from individual non-masked strips with a signal non greater than 3 times the noise value;
- suppress the strips with a sample lower than 3 times the noise value (*zero suppression*).

The sample with the highest charge gives the **charge** of the strip, which is converted in electrons through strip gain in the calibration. The provided information is then used to reconstruct clusters that are employed in the tracking and in the PID. It is important to point out that calibration of

different cluster properties on the two sides of the strips are treated separately because of the different capacitive loads and readout mode of the APV25.

3.4 Cluster reconstruction

The acquired strips that passed the *zero suppression* are processed by the SVD reconstruction software, that will compute position, time, and charge collected after the passage of a particle on the strips. The reconstruction starts with:

- **SVDSHaperDigits**, consisting in an array per strip that contains the digitized samples sent by the APV25;
- **SVDEventInfo**, an object that contains pieces of information about the triggered event, such as the data acquisition mode used by the APV25, the trigger type and the TB value.

A set of adjacent strips that passed the *zero suppression* form a cluster if at least one of the strips, called *seed*, has a Signal to Noise Ratio (SNR) value greater than 5; the efficiency of the cluster reconstruction has been estimated to be ≈ 1 through MC simulation with nominal beam background. The cluster charge S_{CL} is calculated as:

$$S_{CL} = \sum_{i=0}^{i < size} S_i \quad (3.1)$$

where S_i is the charge of the single strip. S_{CL} is correlated to the incident angle of the particle on the strip: the cluster charge is minimal for perpendicularly incident tracks, while the deposit is bigger for slanted trajectories, as shown in fig.3.8. As shown in fig.3.6, the charge distributions are different for the two sides, because of the different sensor capacitive couplings a charge loss is expected on the *v* side.

The **SNR** is defined as the cluster charge over the sum in quadrature of the noise of strips belonging to the same cluster

$$SNR_{CL} = \frac{S_{CL}}{N_{CL}}, \quad N_{CL} = \sqrt{\sum_{i=0}^{i < size} N_i^2} \quad (3.2)$$

and depends on the cluster charge, noise and size; the strip noise, measured as ADC counts and then converted in Equivalent Noise Charge electrons (ENC) through the APV25 gain. Since the u/P strips are longer than the

3.4. CLUSTER RECONSTRUCTION

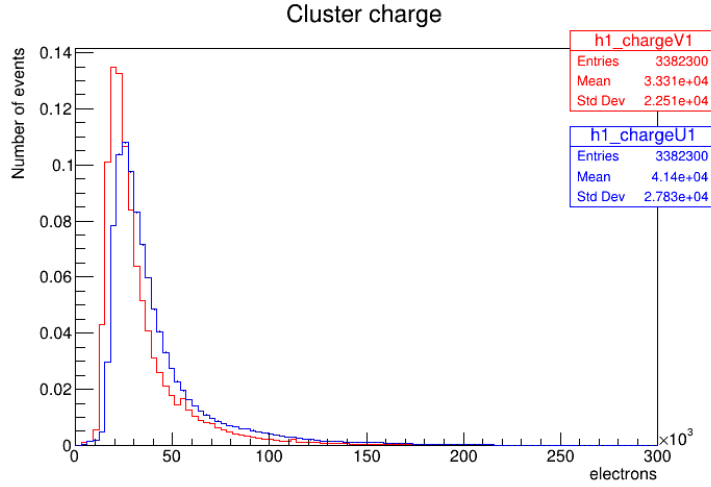


Figure 3.6: Charge distribution with peaks between 21k-24k electrons as predicted for MIPs on u and v sides for simulated $B^0\bar{B}^0$ events.

v/N ones, the noise is also higher on this side; as a consequence, the SNR value is greater on v side than on u side; the SNR performance is reported to be good, as it has a Most Probable Value (MPV) between 13 and 30 (from measurements in July 2020).

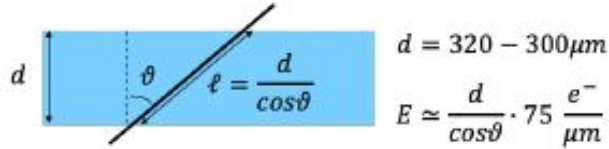


Figure 3.7: Scheme of a SVD sensor; taken from [30].

The cluster **position** x_i and its error Δx_i are computed with different algorithms, depending on the number of strips that form the cluster, taking into account the strip pitch p and the strip charge. The cluster position on data is reconstructed with a resolution, function of the incident angle, of $7\mu\text{m}$ and $11\mu\text{m}$ on u side L3 and L4-5-6 respectively, and of $14\mu\text{m}$ and $20\mu\text{m}$ on v side L3 and L4-5-6 respectively; it has been estimated through the residuals of the cluster position and the unbiased track extrapolation (reconstruction without cluster) on $e^+e^- \rightarrow \mu^+\mu^-$ events with at least 1 PXD hit, 8 SVD and 30 CDC hits and invariant mass of $10\text{-}11\text{GeV}/c^2$.

The cluster time reconstruction is described in section 3.5.

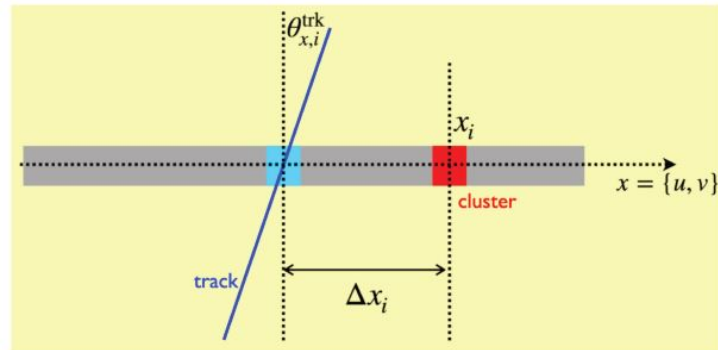


Figure 3.8: Position resolution estimate; the red square represents the cluster, while the blue one is given by the unbiased track extrapolation; taken from [26].

SpacePoint creation

At this point, u/P clusters are combined to v/N ones to provide the 3D hit reconstruction: clusters can be rejected if

- $t_{CL} < t_{min}$: the cluster is early with respect to t_{min} , minimum established time;
- $|t_{CL}| > \Delta t$: the cluster is late with respect to the 0 in the SVD time frame;
- $|t_{CL}(u) - t_{CL}(v)| > \Delta t'$: the time difference between the two sides is greater than the established $\Delta t'$.

This constitutes a clear example of how the timing system can be exploited to reject the background hits. At the moment, thanks to the low background, the application of these criteria are not needed in data reconstruction, therefore all of the $t_{CL}(u)$ and $t_{CL}(v)$ make it to the tracking stage.

3.5 SVD Cluster Time

The cluster time is computed with the algorithm called Center of Gravity 3 (CoG3), that starts with the MaxSum algorithm, that finds the best 3 of the 6 samples to the CoG3 and is divided in three steps:

- finds the highest sum of two consecutive samples ($A_i + A_{i+1}$), with A_i amplitude of the i -th sample;

3.5. SVD CLUSTER TIME

- chooses A_i and A_{i+1} , together with A_{i-1} , where $i - 1$ called First Frame (FF), as the three samples;
- if $i=0$, then the three samples are A_0, A_1, A_2 .

where each sample A_i is the sum of the corresponding j -th strip sample a_i^j :

$$A_i = \sum_{j=strips} a_i^j. \quad (3.3)$$

The raw cluster time is calculated as the weighted average of the sample times ($i\Delta t$), weighted with the sample charge A_i :

$$t_{raw}^{clusters} = \Delta t \cdot \frac{\sum_{i=0}^{i<3} i \cdot A_i}{\sum_{i=0}^{i<3} A_i} \quad (3.4)$$

with $\Delta t \simeq 31.4$ ns, sampling period.

Hit Time Calibration

The Hit Time Calibration uses the correlation between the cluster time and CDC event time. It is implemented in the *Calibration Framework* and needs the time of the event in the SVD frame, defined as:

$$T_0^{SVD} = T_0 - \frac{\Delta t}{4} \cdot (3 - TB - 4FF) \quad (3.5)$$

where $TB=0,1,2,3$ is the trigger bin that gives the correct time shift to switch between the two time references and FF value of the First Frame; this T_0^{SVD} is correlated to the cluster time t_{raw} as shown in fig. 3.9. Neglecting the flight time, the calibration function is

$$t_{hit} = f(t_{raw}) + \delta t \quad (3.6)$$

where δt is the time shift to switch from the SVD reference frame and the global one, and

$$f(t_{raw}) = a + (b + cd^2)t_{raw} - cd t_{raw}^2 + ct_{raw}^3/3 \quad (3.7)$$

with a, b, c, d parameters extracted from the fit of fig 3.9 for the u side and the v side separately for each sensor.

3.5. SVD CLUSTER TIME

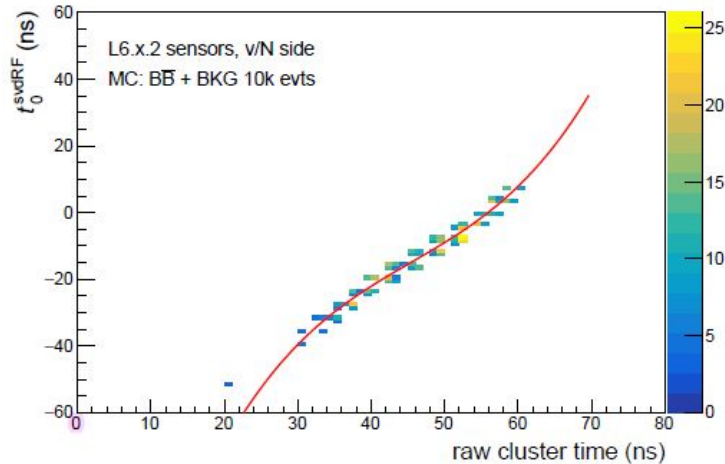


Figure 3.9: Scatterplot of T_0^{SVD} v. t_{raw} ; taken from [30].

Cluster time resolution

The final cluster time, given by the variable $clsTime$, is obtained after the calibration of the $t_{raw}^{clusters}$. The resolution on the cluster time is estimated to be 2-3ns (fig. 3.10 left) for the CoG3 computation on simulated events and 3-4ns on data (fig. 3.10 right), and it is calculated as the width of the residuals defined as:

$$clsTime - eventT0 \quad (3.8)$$

where $eventT0$ is the time of the event corresponding to the one reconstructed by the CDC in the majority of cases.

Cluster time error

Since the cluster time error is missing in the `EventT0` class, it is calculated here through the propagation of uncertainties. We assume that the noise of each sample of the j -th strip is the same, n_j , and that the strip noise is fully correlated among different strips. Therefore σ_A , the error on A_i , given in eq.3.3, is independent from the sample and is calculated as:

$$\Delta A_i = \sum_j n_j = \sigma_A. \quad (3.9)$$

Assuming that the error on Δt is negligible with respect to the noise and that the contributions of each i -th sample are fully correlated, the error on

3.6. CDC AND TOP EVENTT0

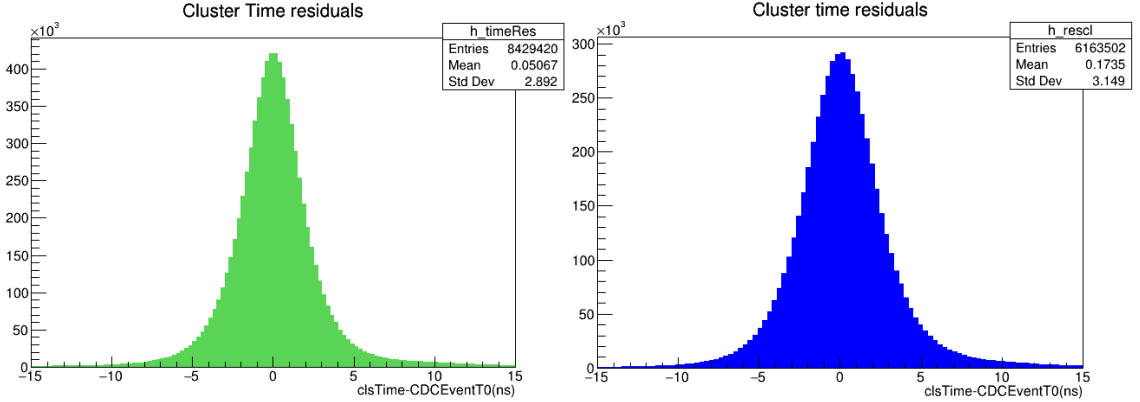


Figure 3.10: Cluster time residuals calculated with respect to the *eventT0* estimated by the CDC for $B^0\bar{B}^0$ simulated events (left) and for hadronic events from experiment 22 run 566 (right): there is a slight worsening $\mathcal{O}(0.5\text{ns})$ of the performances on hadronic events with respect to the simulation.

the raw cluster time is obtained by simple error propagation by eq.3.4:

$$\Delta t_{raw}^{clusters} = \sum_{i=0}^{i<3} \left[\frac{\Delta t \cdot i - t_{raw}^{clusters}}{\sum_k A_k} \right] \cdot \sigma_A. \quad (3.10)$$

The cluster time error is on average $\mathcal{O}(3\text{ns})$ on both simulation and data.

3.6 CDC and TOP EventT0

The detectors that currently provide an *eventT0* are the CDC [37] and the TOP [40].

The CDC measures the arrival time of electrons on a wire (anode) t_1 with respect to the trigger time $t = 0$. To compute an *eventT0* the CDC picks the track with the highest momentum and, with a χ^2 -based fit, it finds the best value of the *eventT0* that is compatible with the measured drift time. The drift time is the time between the trigger signal and the arrival of the drift electrons on the sense wire, and therefore it includes the flight time of the particles and the *eventT0*. For example, if the *eventT0* is overestimated (it happens too late with respect to the trigger), then the track will pass near the wire later than one would expect with the measured t_1 , as displayed in fig.3.11. The module computes the χ^2 for different *eventT0* hypotheses and chooses the one with the minimum χ^2 . An example of the reconstructed *CDCEventT0* is plotted in fig.3.12. The module that computed the *CDCEventT0* is included in the *FullGrid* one, that slows down the online reconstruction in the HLT.

3.6. CDC AND TOP EVENTT0

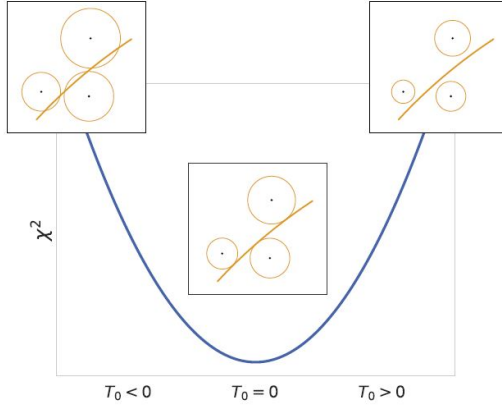


Figure 3.11: χ^2 method for the CDC *eventT0* estimate; taken from [37].

For what concerns the TOP time measurement, the *eventT0* is reconstructed by the **TOPBunchFinder** module, which provides the actual bunch crossing responsible for the triggered collision, thanks to an high time resolution. The algorithm efficiency depends strongly on the type of the event, background and track multiplicity: for MC simulation, the reconstruction efficiency is displayed in table 3.2: while for what concerns the application of

	<i>BB</i>	BhaBha	μ -pairs
no BG	98.3%	99.8%	99.8%
nominal BG	93.0%	94.7%	89.3%

Table 3.2: Reconstruction efficiency of *TOPEventT0* for simulated $B\bar{B}$, Bhabha and μ -pairs events with and without beam background.

the *TOPEventT0* (fig.3.13) on data, the performance depends on the event type; the residuals with respect to *CDCEventT0* depends on the event type, too [41]: for event of Experiment 14 Run 694 the reported offsets, corresponding to the mean of the residuals, are displayed in table 3.3:

	hadron	BhaBha	mumutight
$T0^{CDC} - T0^{TOP}$ (ns)	-3.1	-4.0	-3.8

Table 3.3: Residuals of *CDCEventT0-TOPEventT0* for different datasets.

This suggests that further improvements on the CDC and TOP alignment in time should be carried on to find an efficient combination of *eventT0s*.

3.6. CDC AND TOP EVENT T0

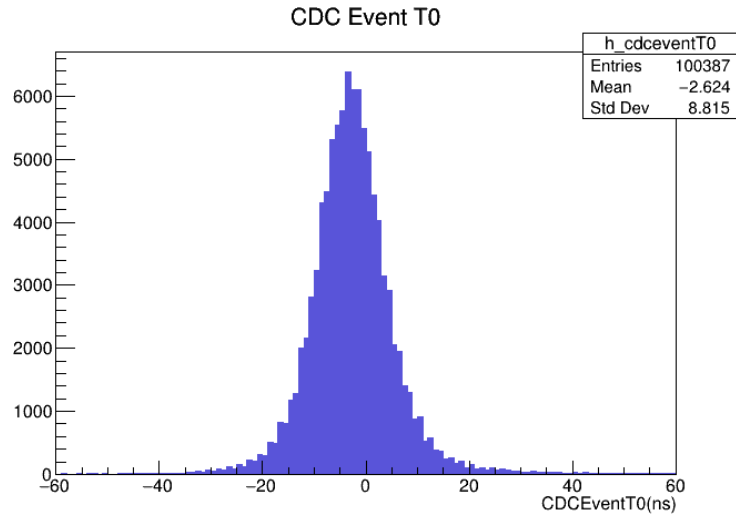


Figure 3.12: $CDCEventT0$ distribution for hadronic events.

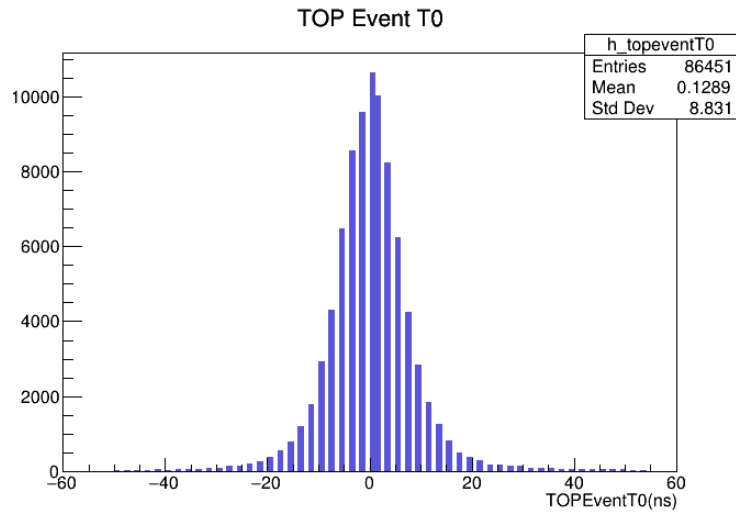


Figure 3.13: $TOPEventT0$ distribution for hadronic events.

Chapter 4

Event Time estimate with SVD

In this chapter the estimate of the event time given by SVD is described, together with the optimization of the algorithm. Its performance on Monte Carlo events, i.e. $B\bar{B}$ and τ -pairs is studied: the computation is performed with and without nominal beam background for the former, and with nominal beam background for the latter. The resolution on the computation with respect to the true event time, introduced in Chapter 3, is displayed to offer a benchmark for data and Monte Carlo comparison.

4.1 Event time computation

Conceptually, $SVDEventT0$ can be estimated starting from the the SVD-only time information, given the excellent hit reconstruction and the high resolution on the cluster time. The clusters used in the computation are signal clusters, i.e. clusters associated to tracks, so background hits are excluded. In the first place, a fundamental hypothesis is assumed: the tracks used belong to the same event and have a high purity. Under this hypothesis, the event time is estimated as the average time of the hits associated to tracks. The temporal information associated to a cluster is represented by the variable $clsTime$ so all the hit times in SVD are summed and divided by the number of clusters of that same event, given by the variable $nCluster$:

$$T0_{SVD} = \frac{1}{nCluster} \sum clsTime \quad (4.1)$$

Knowing the cluster time error, it is possible to calculate the uncertainty on $SVDEventT0$ as:

$$\Delta T0_{SVD}^2 = \left(\frac{1}{nCluster} \right)^2 \sum \sigma_{clstime}^2 \quad (4.2)$$

4.1. EVENT TIME COMPUTATION

The flight time of the particles to SVD layers is not a problem since it does not generate a wide spread in the cluster time distributions, that could lead to an overestimate of $SVDEventT0$. The comparison between the cluster times is shown in fig.4.1, for simulated $B^0\bar{B}^0$ events (with no background) the $clsTime$ on the two layers have a reported offset of $\Delta t \simeq 0.04\text{ns}$ in average, which is computable as the difference between the means of the distributions, displayed in the table 4.1

layer	mean[ns]
L3	3.32
L4	3.32
L5	3.29
L6	3.29

Table 4.1: Mean values for cluster time distributions on the four layers of SVD

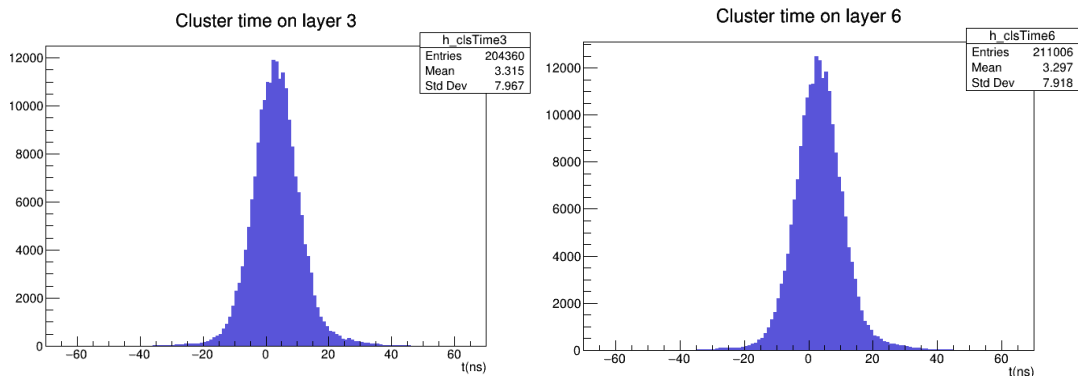


Figure 4.1: Cluster time distributions on L3 and L6 for simulated $B^0\bar{B}^0$.

The order of magnitude of the flight time can be estimated with a geometric construction of simulated particles travelling helices in the magnetic field towards the SVD sensors. The geometric construction is based on the assumption of helical trajectories, and does not take into account distortions caused by the interaction with the detector material. Given the measured transverse momentum is it possible to calculate the Lorentz factor and the velocity of a particle for each mass hypothesis ($m = m_e, m_\mu, m_\pi, m_K, m_p$)

$$\gamma = \frac{E}{m} \quad \text{and} \quad \beta = \frac{p}{m\gamma} \quad (4.3)$$

and, from the magnetic rigidity, the curvature radius of the charged particles

4.1. EVENT TIME COMPUTATION

in the magnetic field B

$$\rho[m] = \frac{p_T c [GeV]}{0.3B[T]} \quad (4.4)$$

Then, the circumference (fig.4.2) travelled by the particle in the transverse plane is assumed to be

$$x^2 + (y - \rho)^2 = \rho^2 \quad (4.5)$$

where ρ is calculated in equation (4.4); for fixed $y = L_i$, where L_i is the distance between the four SVD layers and the IP, assumed to be the origin of reference system, the solution of (4.5) is

$$x_i = \pm \sqrt{\rho^2 - (L_i - \rho)^2} \quad (4.6)$$

From (4.6) it is possible to calculate the arc of the circle S_i travelled by the

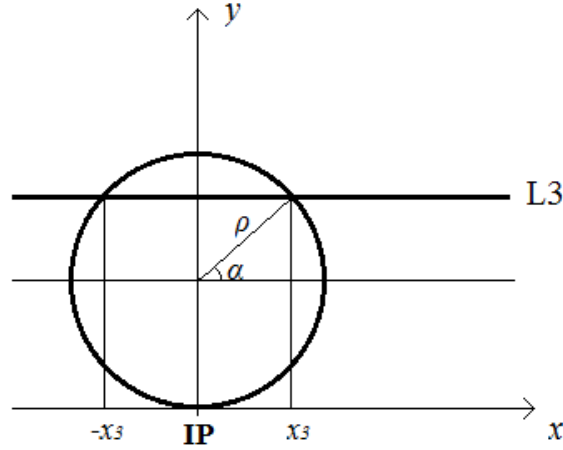


Figure 4.2: Geometric construction scheme.

curved particles, identified by the the angle α_i , for arriving to a layer:

$$\alpha_i = \arctan \left(\frac{\sin \alpha_i}{\cos \alpha_i} \right) = \arctan \left(\frac{L_i - \rho}{\alpha_1} \right) \quad (4.7)$$

$$S_i = \rho \left(\frac{\pi}{2} + \alpha_i \right) \quad (4.8)$$

and finally an upper limit for the flight time:

$$\Delta t' = \frac{S_i}{\beta} \quad (4.9)$$

For the different mass hypotheses ($e^\pm, \mu^\pm, \pi^\pm, K^\pm, p\bar{p}$), the resulting Δt distributions are plotted in fig.4.3. For pions (the most abundant species) the

4.1. EVENT TIME COMPUTATION

difference between the mean of L3 and L6 of the flight time is $\Delta t' \simeq 0.25\text{ns}$, while for protons it can be up to 0.75ns on average. This flight time is comparable with the true one, *trueft*, computed without distinction among the particles masses and plotted in fig.4.4, calculated as the difference between the true cluster time and the true event time:

$$\text{trueFT} = \text{trueTime} - \text{trueEventT0} \quad (4.10)$$

that has a mean value of 0.65ns , compatible with the FT of the geometric construction.

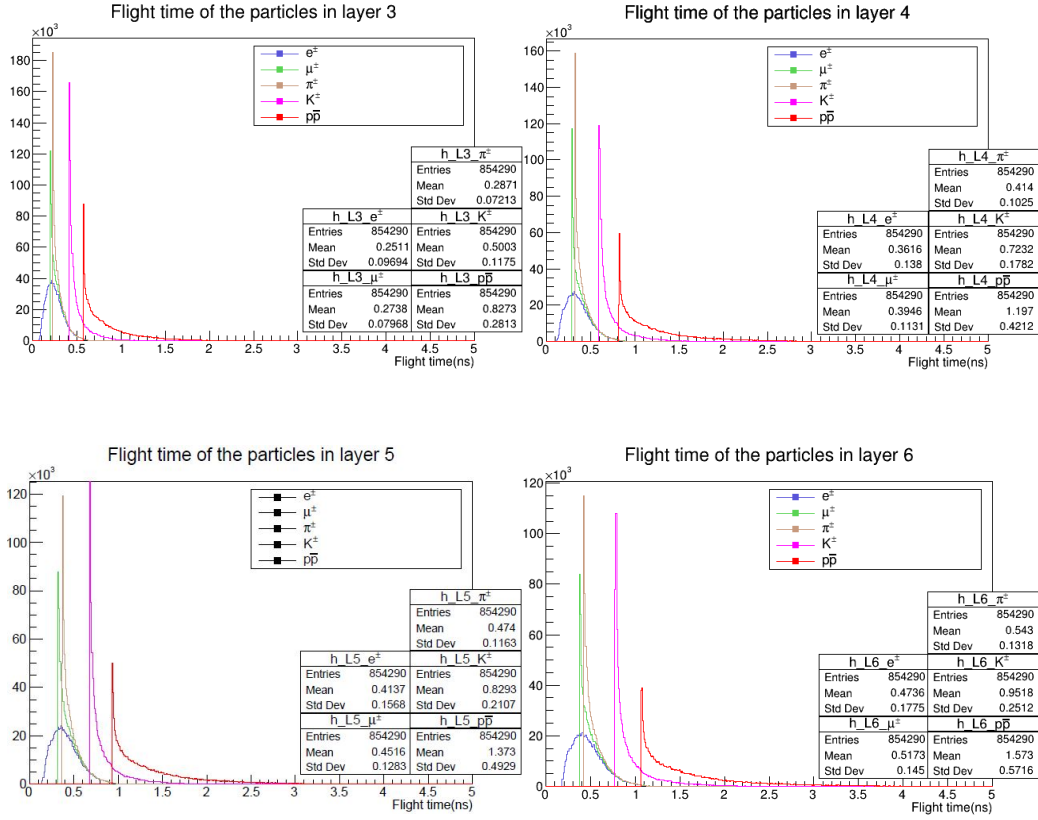


Figure 4.3: *FT* distribution on L3 (top left), L4 (top right), L5 (bottom left) and L6 (bottom right).

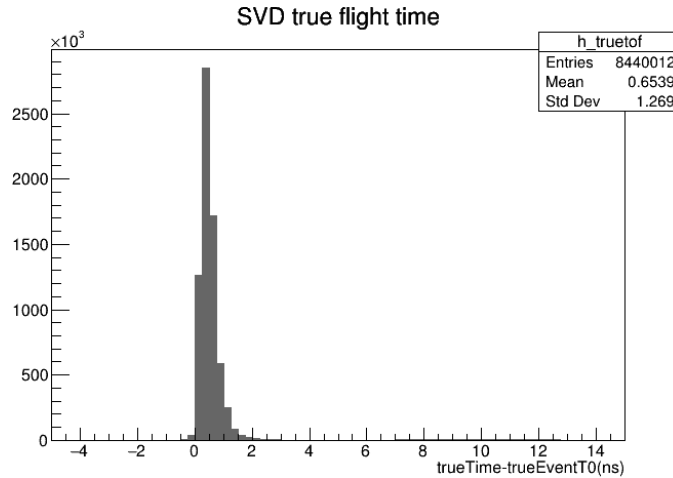


Figure 4.4: True flight time of simulated $B^0\bar{B}^0$ events.

4.2 Event time estimate on Monte Carlo

The estimate in eq.4.1 is first applied to Monte Carlo events, in particular to:

- simulated $e^+e^- \rightarrow \Upsilon(4S) \rightarrow B^0\bar{B}^0$, corresponding to events with the highest track multiplicity per event;
- simulated $e^+e^- \rightarrow \tau^+\tau^-$, corresponding to events with the lowest track multiplicity per event;

if the *SVDEventT0* estimate works well on these events, then it should suit all of the other cases in between in terms of track multiplicity.

The *steering files* run to generate the events, are written in Python 3 and contain:

- the `expList` number, from which the simulated events are taken; it is set to 1003, corresponding to the current detector and machine status, for events without background, and 0, corresponding to detector and machine conditions at nominal luminosity, for events with nominal background;
- the generator module, which contains different function to generate different physics events, such as `evtgen_generator` for $B\bar{B}$ or `kkmc_generator` for $\tau^+\tau^-$;
- the `tracking_reconstruction` module;

- the ROOT ntuple that is used to analyze the events through a list of different variables stored in the TREE; the one used in this thesis is `SVDEventTOTTreePerformance`.

The computation is applied at first to a run simulated with no background, and then to one with nominal background, which is the highest background expected. The time variables took into account for the analysis are:

- *trueTime*: the true signal cluster time (that has a peculiar shape due to the convolution of the *trueEventT0* and the flight time);
- *clsTime*: the measured signal cluster time, that is the convolution of the *trueTime* and the experimental resolution (*clsTime* residuals, integrated on all the possible jitter that give a finite resolution of 2.5ns);
- *trueEventT0*: the true event time, convolution of the filling pattern and the trigger jitter;
- *eventT0*: the event time measured by the CDC, given the tracking reconstruction (neither TOP nor ECL are included), corresponding to the convolution of the *trueEventT0* and the experimental resolution.

The analysis is carried out with the imposition of $trueEventT0 \neq -999$, that is the error bin filled in case the simulation does not provide the truth matching (the MC provides a one-to-one match between a true simulated candidate particle and a reconstructed one): this way, events that miss the *CDCEventT0* are excluded.

4.2.1 $B^0\bar{B}^0$ events without beam background

The first performance study of the *SVDEventT0* algorithm is on 10000 simulated $e^+e^- \rightarrow \Upsilon(4S) \rightarrow B^0\bar{B}^0$ events from Belle II experiment 1003 with no background and tracking reconstruction. Before looking at the *SVDEventT0*, the time variables contained in the ROOT ntuple `SVDEventTOTTreePerformance` are analyzed.

The *trueTime* distribution, whose distribution is shown in fig.4.5 (left), can be compared to the reconstructed cluster time: the residuals computed as

$$clsTime - trueTime \tag{4.11}$$

give a measure of the difference between the SVD reconstruction and the MC truth. The cluster time residuals in fig.4.5 (right) have a small bias of -0.5ns, as expected since the cluster time is calibrated using the *CDCEventT0*, and

4.2. EVENT TIME ESTIMATE ON MONTE CARLO

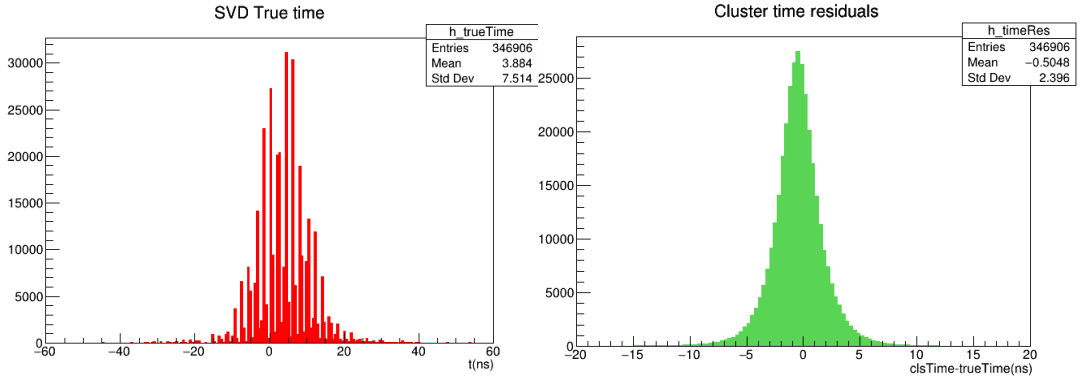


Figure 4.5: (left) True cluster time distribution for simulated $B^0\bar{B}^0$ events with no beam background; (right) cluster time residuals with respect to the true time.

a resolution of 2.4ns; no significant differences are observed looking at the four layers, similarly to what happens for the cluster time as shown in table 4.2. However, a slight variation is observed for the cluster time residuals on

layer	mean(ns)	σ (ns)
L3	-0.48	2.41
L4	-0.49	2.41
L5	-0.51	2.39
L6	-0.53	2.38

Table 4.2: Mean and standard deviation of cluster time residuals on different layers.

u and v sides, probably due to the different APV25 readout modes and the different speed of the carriers.

The residuals of $CDCEventT0$ with respect to $trueEventT0$, shown in fig.4.6 (right), is calculated as

$$trueEventT0 - CDCEventT0 \quad (4.12)$$

These residuals presents a very small bias of 0.15ns and a standard deviation of about 0.56ns; these values are the one to compare those of $SVDEventT0$.

The next step is to compute $SVDEventT0$ on $B^0\bar{B}^0$ events as in eq.4.1: the resulting distribution is plotted in fig.4.7. For a $B^0\bar{B}^0$ simulation without beam background, $SVDEventT0$ is calculated with an efficiency of 100%. Its residuals are computed as

$$SVDEventT0 - trueEventT0 \quad (4.13)$$

4.2. EVENT TIME ESTIMATE ON MONTE CARLO

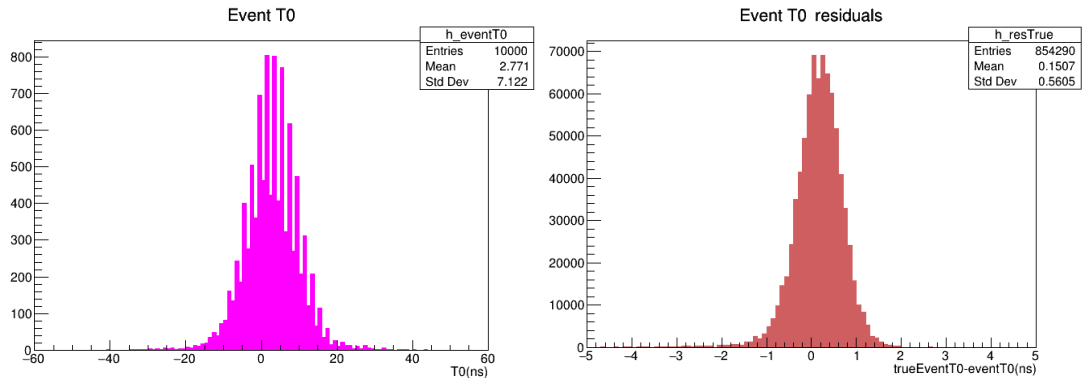


Figure 4.6: (left) $CDCEventT0$ for simulated $B^0\bar{B}^0$ events with no beam background; (right) CDC event time residuals with respect to the true time.

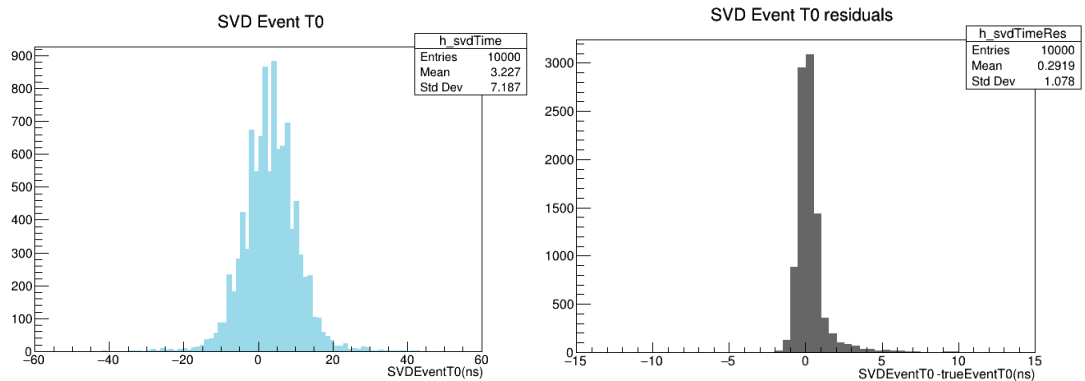


Figure 4.7: (left) $SVDEventT0$ distribution for simulated $B^0\bar{B}^0$ events with no beam background; (right) $SVDEventT0$ residuals with respect to $trueEventT0$.

and are shown in fig.4.7 (right): both the bias and the resolution, that are 0.3ns and 1ns respectively, are approximately twice the bias and the resolution of $CDCEventT0$. Unfortunately, the residuals distribution in fig.4.7 has an undesired tail, supposedly linked to soft particles: different features of tracks and clusters, and their impact on the $SVDEventT0$ residuals, are studied to reduce the tail. The correlation between $SVDEventT0$ residuals and the number of tracks per event is firstly checked and reported in fig.4.8: for events with 5 to 15 tracks, $SVDEventT0$ is essentially unbiased with respect to $trueEventT0$, while for events with more than 15 tracks the $SVDEventT0$ is overestimated. Therefore, we need to find a good rejection criteria to reject the tracks that cause the tail on the $SVDEventT0$ residuals.

Among the variables taken into account that yielded no optimization,

4.2. EVENT TIME ESTIMATE ON MONTE CARLO

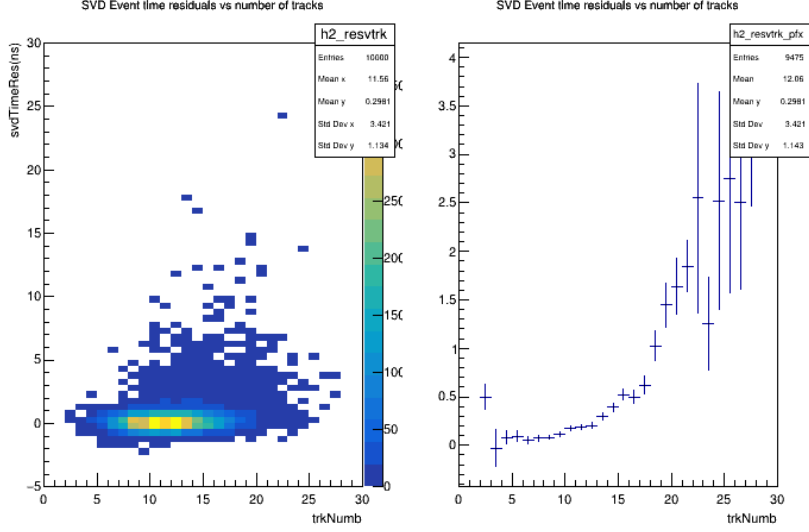


Figure 4.8: Scatterplot of $SVDEventT0$ residuals and the number of tracks per $B^0\bar{B}^0$ events and its profile.

there are the polar and the azimuthal angles θ and ϕ and the number of hits in the CDC. The first variable that produced good results is the transverse momentum p_T , shown in fig.4.9 (left). Different cuts under the mean value of 414MeV/c are attempted in order to both cut the tail of the residuals and keep an high efficiency for the $SVDEventT0$ computation. The best selection is found to be $p_T > 250\text{MeV}/c$ since it reduces the tail of the distribution, losing only 1 in 10^4 events. The correlation plot in fig.4.9 (right) appears less scattered than the previous one, implying for that events with 6 to 20 tracks $SVDEventT0$ computed as in eq.4.1 is basically a good estimate with a bias $< 0.5\text{ns}$. The $SVDEventT0$ residuals, plotted in fig.4.10, have a bias of 0.1ns, smaller than the one without the cut, and a better resolution, of 0.62ns, than before.

Another variable used for the optimization of the algorithm is the cluster SNR , whose cut is decided by looking at the scatterplot in fig.4.11; for SNR values between 10 and 50, that give an essentially unbiased profile of the SNR means, in addition to the previous cut on p_T , the $SVDEventT0$ computation is run again, resulting in a slight but negligible change in bias and standard deviation for the residuals in fig.4.13 (left), respectively of 0.15ns and 0.61ns, whereas the efficiency is left unaltered; although the tail is faintly shrank (fig.4.13 left) no remarkable improvements are observed. Therefore this cut is not considered anymore.

The last variable to play with is the longitudinal momentum p_z : looking

4.2. EVENT TIME ESTIMATE ON MONTE CARLO

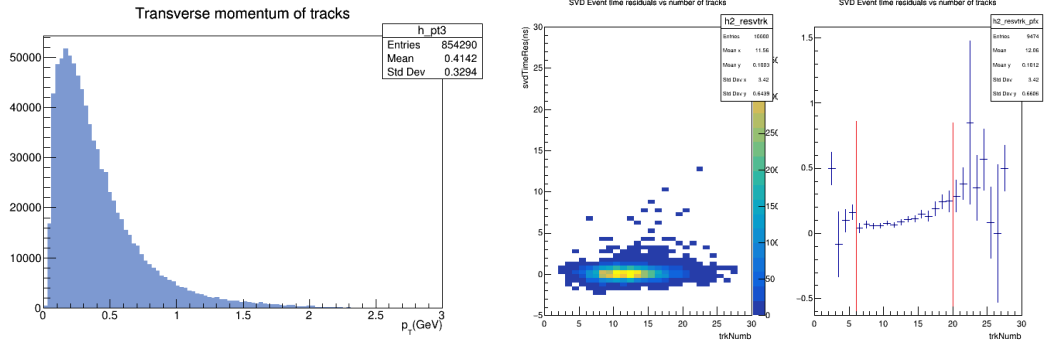


Figure 4.9: (left) Transverse momentum distribution for simulated $B^0\bar{B}^0$ events with no beam background; (right) scatterplot of $SVDEventT0$ residuals and the number of tracks per $B^0\bar{B}^0$ events and its profile with the selection $p_T > 250\text{MeV}/c$.

at its distribution (fig.4.12) and its mean of $270\text{MeV}/c$, one of the possible values to select is $p_z > 100\text{MeV}/c$. The selection is then implemented in the algorithm and $SVDEventT0$ and its residuals, in fig.4.13(right), are obtained: while the bias and the standard deviation improve moderately, reaching 0.06ns and 0.55ns respectively, the efficiency decreases since 7 additional events, on a total of 8 events out of 10^4 , are lost.

Mean, standard deviation (σ) and absolute efficiency (ε) of the algorithm for the discussed cuts are summarized in table 4.3.

cuts	mean(ns)	σ (ns)	ε
no cuts	0.29	1.08	100%
$p_T > 250\text{MeV}/c$	0.09	0.62	99.99%
$p_T > 250\text{MeV}/c$ & $10 < SNR < 50$	0.15	0.61	99.99%
$p_T > 250\text{MeV}/c$ & $p_z > 100\text{MeV}/c$	0.06	0.55	99.92%

Table 4.3: Recap of the performances of $SVDEventT0$ algorithm and optimization on $B^0\bar{B}^0$ events with no background.

To sum up, all the discussed selections successfully remove the tail on the $SVDEventT0$ residuals. Looking at table 4.3, the selections are comparable in terms of both σ , that is between 0.5 and 0.6ns , and ε , between 99.92% and 99.99% . Among the cuts discussed, the most favorable could be the one on p_T , since it is the simplest one. The cuts on p_T and p_z are applied to $B^0\bar{B}^0$ and $\tau^+\tau^-$ events with nominal beam background; since the cut on the SNR does not improve significantly either the resolution or the efficiency of the $SVDEventT0$, it is permanently excluded.

4.2. EVENT TIME ESTIMATE ON MONTE CARLO

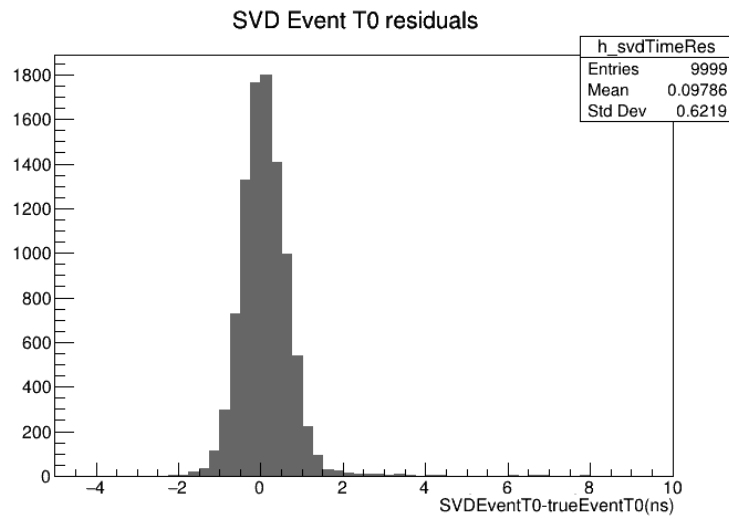


Figure 4.10: $SVDEventT0$ residuals distribution for simulated $B^0\bar{B}^0$ events with no beam background and with the selection $p_T > 250\text{MeV}/c$.

Despite the simplicity of the computation, that is a mean, $SVDEventT0$ can achieve great precision, comparable to that of the CDC (0.15ns bias and 0.56ns standard deviation) and an efficiency greater than 99.9% for $B\bar{B}$ without beam background.

4.2. EVENT TIME ESTIMATE ON MONTE CARLO

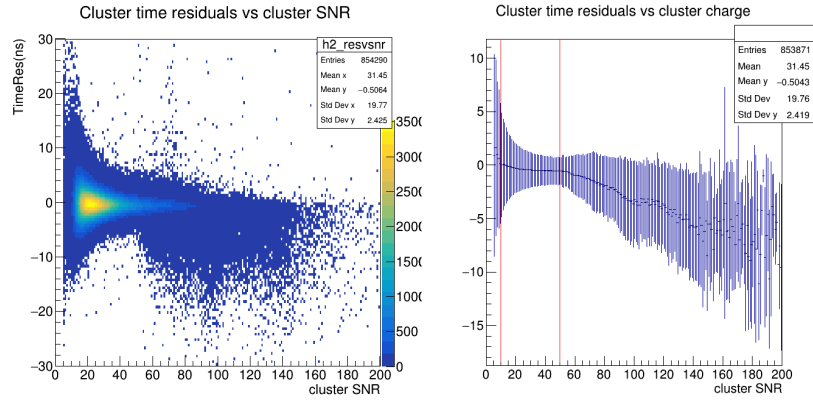


Figure 4.11: Scatterplot of cluster time residuals and the number of tracks per $B^0\bar{B}^0$ events and its profile.

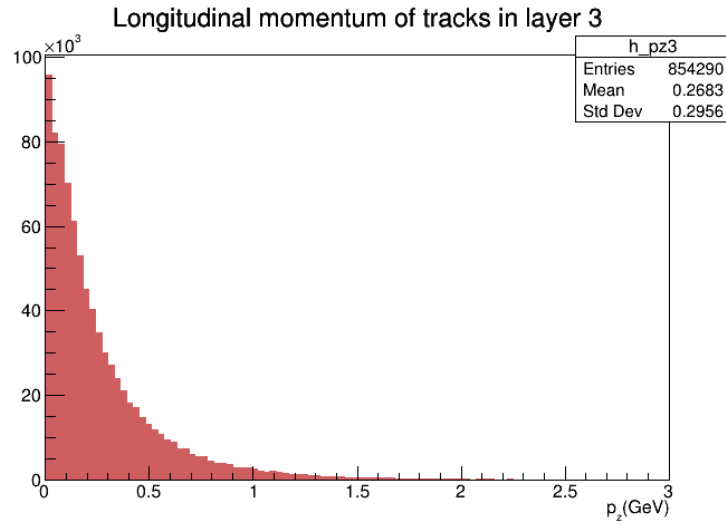


Figure 4.12: Longitudinal momentum distribution for simulated $B^0\bar{B}^0$ events with no beam background.

4.2. EVENT TIME ESTIMATE ON MONTE CARLO

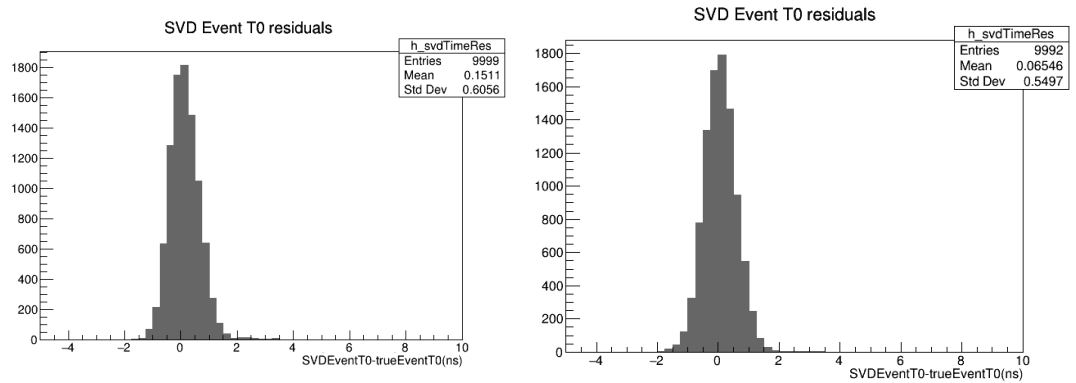


Figure 4.13: (left) $SVDEventT0$ residuals distribution for simulated $B^0\bar{B}^0$ events with no beam background and with the selection $p_T > 250 \text{ MeV}/c$ and $10 < SNR < 50$; (right) $SVDEventT0$ residuals distribution for simulated $B^0\bar{B}^0$ events with no beam background and with the selections $p_T > 250 \text{ MeV}/c$ and $p_z > 100 \text{ MeV}/c$.

4.2.2 $B^0\bar{B}^0$ events with nominal beam background

The algorithm is applied to a more challenging scenario, with the addition of the nominal beam background, i.e. the one expected at target luminosity; 100000 $B^0\bar{B}^0$ events are generated from Belle II Experiment 0 with tracking reconstruction ($TOPEventT0$ is still not available in the ntuple). The distributions of the cluster time and its residuals with respect to $trueEventT0$ are plotted in fig.4.14: the residuals (right) do not show significant changes with respect to the no background case.

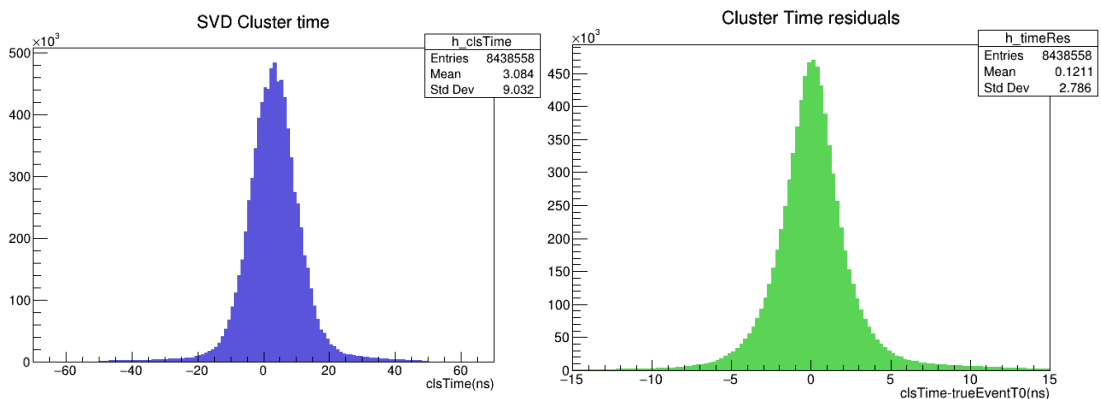


Figure 4.14: Cluster time distribution and its residuals with respect to $trueEventT0$ for $B^0\bar{B}^0$ events with nominal beam background.

A slight broadening is reported for the $CDCEventT0$ distribution, shown in fig.4.15(left) and its residuals, computed for events with an associated $CDCEventT0$ and $trueEventT0$, in fig.4.15(right), in particular the resolution is a bit worse, going from 0.56ns in the no background case, to 0.79ns. The mean and resolution values to compare the $SVDEventT0$ residuals ones are, respectively, -0.07ns and 0.79ns. The computation is applied and the resulting plot is shown in fig.4.16: the bias and the width, 3.05ns and 7.22ns respectively, are compatible with the values of the no background case, of 3.23ns and 7.19ns.

Without any selection, the residuals plot in fig.4.17(left) shows the unpleasant tail of events on the right: the optimization applied in the case without beam background is tested on this case, too. As discussed in the previous section, the possible selections are on p_T and p_z , in particular:

1. $p_T > 250\text{MeV}/c$
2. $p_T > 250\text{MeV}/c$ & $p_z > 50\text{MeV}/c$
3. $p_T > 250\text{MeV}/c$ & $p_z > 100\text{MeV}/c$

4.2. EVENT TIME ESTIMATE ON MONTE CARLO

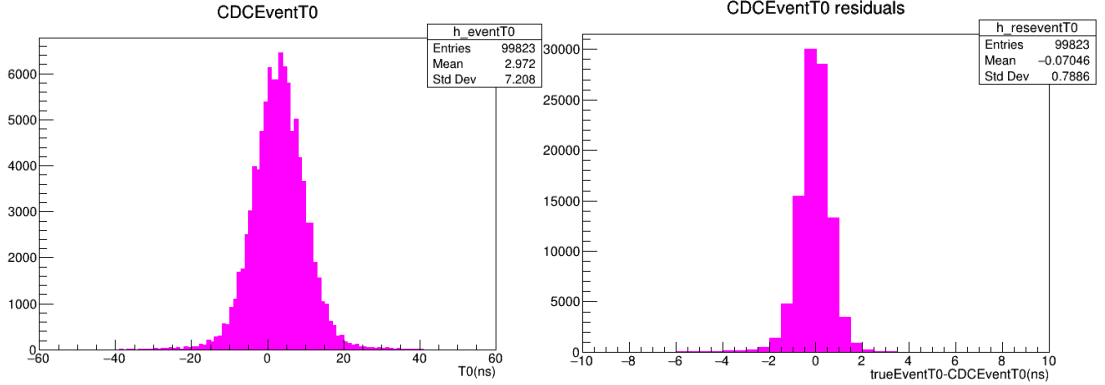


Figure 4.15: $CDCEventT0$ distribution and its residuals with respect to $trueEventT0$ for $B^0\bar{B}^0$ events with nominal beam background.

In table 4.4 the bias, the resolution σ , and the absolute efficiency ε are displayed for the different applied selections on the $SVDEventT0$ residuals, shown in fig.4.17 (right) and 4.18. Even with the nominal background, the

cuts on $B^0\bar{B}^0$ events	bias	σ	ε
no cut	0.13ns	1.74ns	99.996%
$p_T > 250MeV/c$	0.03ns	0.76ns	99.977%
$p_T > 250MeV/c$ & $p_z > 50MeV/c$	$8 \cdot 10^{-3}ns$	0.74ns	99.944%
$p_T > 250MeV/c$ & $p_z > 100MeV/c$	$9 \cdot 10^{-3}ns$	0.76ns	99.845%

Table 4.4: Recap of the performances of $SVDEventT0$ algorithm and optimization on $B^0\bar{B}^0$ events with nominal beam background.

$SVDEventT0$ algorithm can reach performances similar to the previous case with no beam background. It is affected by a small bias, which is negligible with the optimizing cuts, and has high efficiency (over 99.8%) and resolution of 0.75ns in average. Since the resolution does not vary significantly and the efficiency slightly lowers, the most favorable cut seems to be the simplest one, with the selection on p_T only.

4.2.3 $\tau^+\tau^-$ events with nominal background

After the promising results on $B^0\bar{B}^0$ events, to study the feasibility of the $SVDEventT0$ computation, it can be tested on τ -pairs. With respect to the previous script, the steering file has been modified with τ generator, but kept the tracking reconstruction, the Experiment number 0 and the output ROOT ntuple `SVDEventT0TreePerformance` untouched; the analysis without the

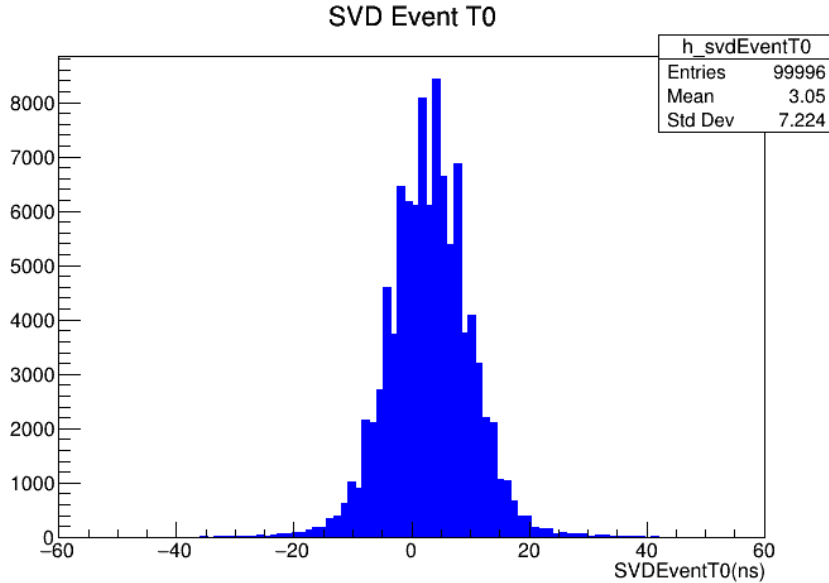


Figure 4.16: $SVDEventT0$ distribution for simulated $B^0\bar{B}^0$ events with nominal beam background.

background is skipped since the observed performance on $B^0\bar{B}^0$ deteriorates of $\mathcal{O}(0.4\text{ns})$ with its addition; 100000 $e^+e^- \rightarrow \tau^+\tau^-$ are generated.

Again, the $CDCEventT0$ performance and its residuals with respect to $trueEventT0$ are checked, as in fig.4.19, computed for events with an associated $trueEventT0$ or $CDCEventT0$ respectively. The event time, plotted in fig.4.19 (left), has a mean value of 2.32ns and a standard deviation of 9.16ns. Its residuals, plotted in fig.4.19 (right), are basically unbiased with respect to the true event time, and have a standard deviation of 1.11ns, which corresponds to a worsening of $\approx 40\%$ with respect to $B^0\bar{B}^0$ events.

Because of the truth matching failure, 1798 events out of 100000 do not have a $trueEventT0$ associated value, that corresponds to almost the 2% of the total, so $SVDEventT0$ is plotted only for those events that have one; its distribution, shown in fig.4.20, has a slightly smaller bias ($\approx 7\%$) but a worse resolution of about 12% than $B^0\bar{B}^0$ events.

The $SVDEventT0$ residuals, plotted in fig.4.21 (left) do not show the tail on the right of the distribution, as in fig.4.17 so the optimization is not really useful for this purpose, although it may reduce the background tails; nevertheless the resolution could be improved since it is twice the one of $CDCEventT0$ residuals in fig.4.19 (right): the same cuts as in $B\bar{B}$ case are applied:

1. $p_T > 250\text{MeV}/c$

4.2. EVENT TIME ESTIMATE ON MONTE CARLO

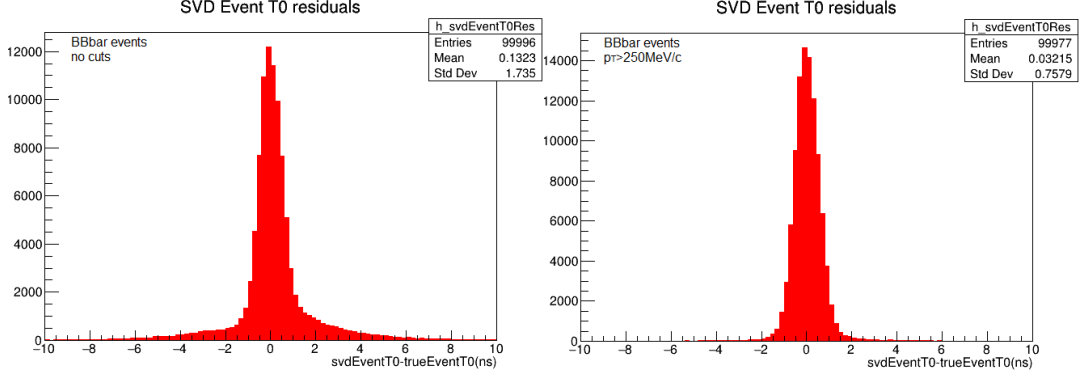


Figure 4.17: $SVDEventT0$ residuals with no selection applied (left) and with the $p_T > 250 \text{ MeV}/c$ (right) for simulated $B^0\bar{B}^0$ events with nominal beam background.

2. $p_T > 250 \text{ MeV}/c$ & $p_z > 50 \text{ MeV}/c$
3. $p_T > 250 \text{ MeV}/c$ & $p_z > 100 \text{ MeV}/c$

The resulting distribution of the $SVDEventT0$ residuals are plotted in figs.4.21 (right) and 4.22 and summarized in table 4.5. The bias is not significantly altered with respect to the no cut case, while the resolution σ improves a lot, going to 2.31ns to $\sim 0.96\text{ns}$ on average. However there is a loss of events causing a decrease of the absolute efficiency ε ($< 98\%$).

cuts on $\tau^+\tau^-$ events	bias	σ	ε
no cut	0.04ns	2.31ns	98.202%
$p_T > 250 \text{ MeV}/c$	0.04ns	0.97ns	96.417%
$p_T > 250 \text{ MeV}/c$ & $p_z > 50 \text{ MeV}/c$	0.03ns	0.95ns	95.588%
$p_T > 250 \text{ MeV}/c$ & $p_z > 100 \text{ MeV}/c$	0.03ns	0.95ns	94.492%

Table 4.5: Recap of the performances of $SVDEventT0$ algorithm and optimization on $\tau^+\tau^-$ events with nominal beam background.

To sum up, the bias and resolution of the $SVDEventT0$ do not change significantly with the different cuts, while the absolute efficiency drops from $\sim 98\%$ to $\sim 94\%$, the best cut is indeed the $p_T > 250 \text{ MeV}/c$ one, definitely.

4.2. EVENT TIME ESTIMATE ON MONTE CARLO

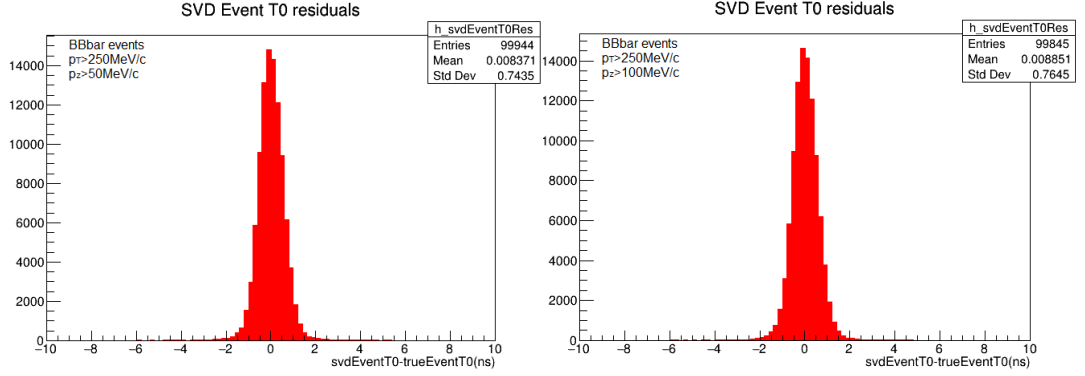


Figure 4.18: $SVDEventT0$ residuals with the selections $p_T > 250 \text{ MeV}/c$ and $p_z > 50 \text{ MeV}/c$ (left) and with the selections $p_T > 250 \text{ MeV}/c$ and $p_z > 100 \text{ MeV}/c$ (right) for simulated $B^0\bar{B}^0$ events with nominal beam background.

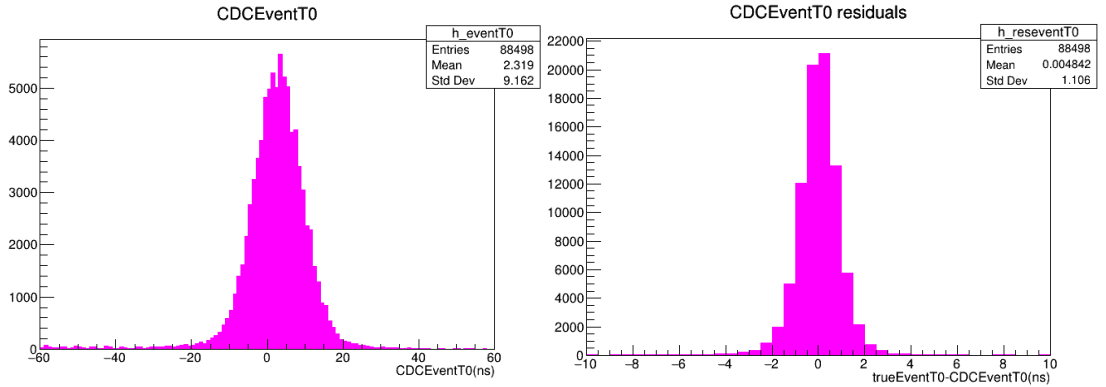


Figure 4.19: $CDCEventT0$ distribution and its residuals with respect to $trueEventT0$ for $\tau^+\tau^-$ events with nominal beam background.

4.2. EVENT TIME ESTIMATE ON MONTE CARLO

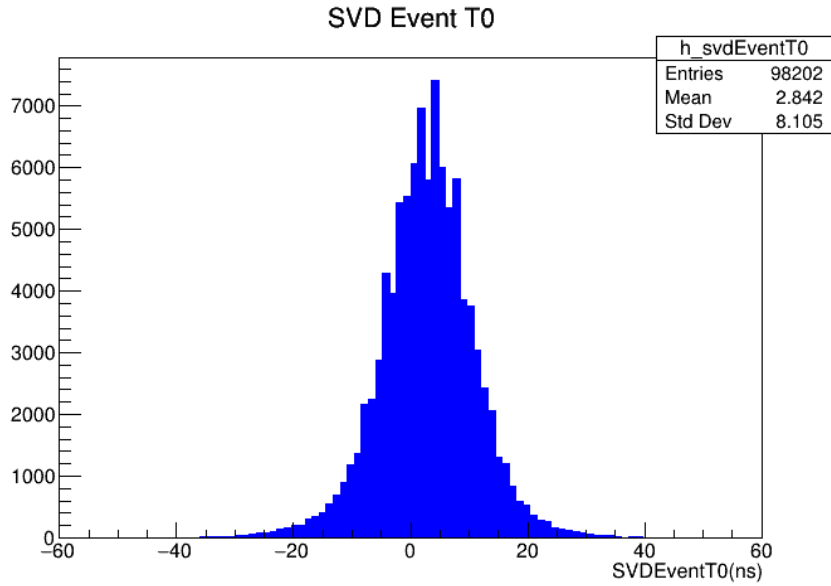


Figure 4.20: $SVDEventT0$ distribution for simulated $\tau^+\tau^-$ events with nominal beam background.

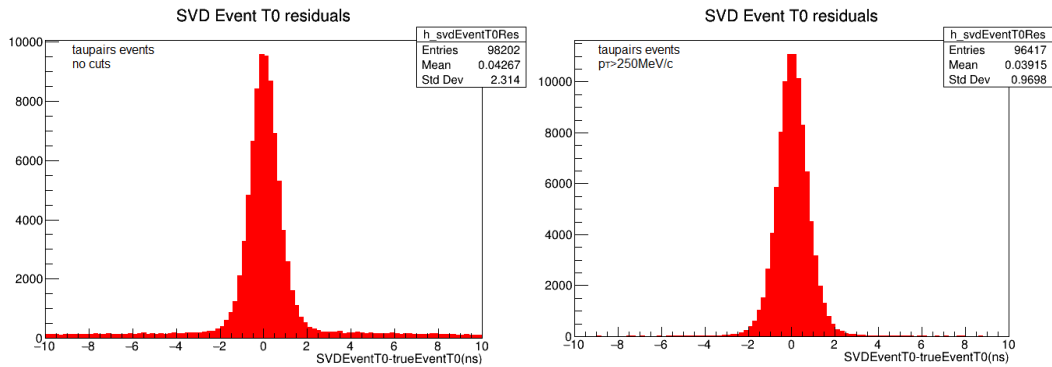


Figure 4.21: $SVDEventT0$ residuals with no selection applied (left) and with the $p_T > 250 \text{ MeV}/c$ cut (right) for simulated $\tau^+\tau^-$ events with nominal beam background.

4.2. EVENT TIME ESTIMATE ON MONTE CARLO

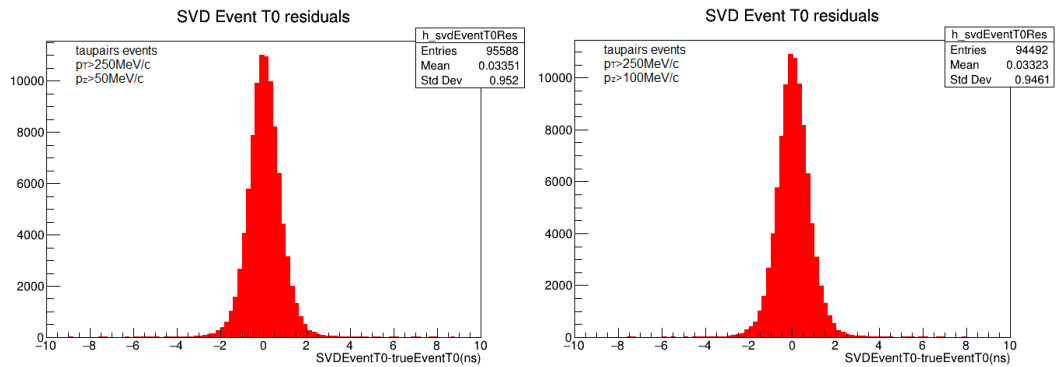


Figure 4.22: $SVDEventT0$ residuals with the selections $p_T > 250 \text{ MeV}/c$ and $p_z > 50 \text{ MeV}/c$ (left) and with the selections $p_T > 250 \text{ MeV}/c$ and $p_z > 100 \text{ MeV}/c$ (right) for simulated $\tau^+\tau^-$ events with nominal beam background.

4.3 Summary on simulated events

At the beginning, to optimize the *SVDEventT0* and remove the tail on its residuals, different cuts were tried out on $B^0\bar{B}^0$ events with no beam background. Among these cuts, there were selections on the transverse momentum, $p_T > 250\text{MeV}/c$, on the SNR, $10 < SNR < 50$, and on the longitudinal momentum, $p_z > 100\text{MeV}/c$. Since the cut on the SNR did not improve significantly the performance of the algorithm, it was definitely removed. Now, on $B^0\bar{B}^0$ and $\tau^+\tau^-$ events with nominal beam background, the selection of tracks is made with cuts on p_T and p_z only. The chosen cut, which is favorable in terms of both absolute efficiency ε and resolution σ is the $p_T > 250\text{MeV}/c$ one. A summary of the performance of *SVDEventT0* and a comparison to *CDCEventT0* is displayed in table 4.6: on Monte Carlo, *SVDEventT0* has a slightly better resolution and a higher absolute efficiency than *CDCEventT0*. The $p_T > 250\text{MeV}/c$ cut is implemented in the algorithm and it is applied to

	$B^0\bar{B}^0$		$\tau^+\tau^-$	
	<i>SVDEventT0</i>	<i>CDCEventT0</i>	<i>SVDEventT0</i>	<i>CDCEventT0</i>
bias[ns]	0.03	-0.07	0.04	$4 \cdot 10^{-3}$
σ [ns]	0.76	0.79	0.97	1.11
efficiency	99.98%	99.82%	96.42%	88.49%

Table 4.6: Recap of the performance of *SVDEventT0* for $B^0\bar{B}^0$ and $\tau^+\tau^-$ events with nominal background, with the selection $p_T > 250\text{MeV}/c$, and comparison to the *CDCEventT0*.

some sets of data collected in 2021.

Chapter 5

SVD event time estimate on data

In this chapter, the event time estimate by SVD is applied to different datasets collected in 2021 and its performance and efficiency are studied. The first studied dataset is the one containing hadronic events, used to make a comparison with Monte Carlo $B^0\bar{B}^0$ events; other events taken in to account are BhaBha and μ -pairs, to test the feasibility of the algorithm on events with a different topology. As a matter of facts, BhaBha and μ -pairs events have lower track multiplicity than the hadronic ones: their event time is more difficult to estimate since they have a lower number of signal clusters to use in the algorithm. Finally, a summary of the performance of *SVDEventT0* is given and the execution time of the algorithm is estimated.

5.1 Data samples

Given the promising results, regarding both efficiency and resolution, of the *SVDEventT0* algorithm on simulated events, it can be applied on Belle II data acquired in 2021. The data are usually stored in Mini Data Summary Tables (mDSTs), that contain reconstructed objects, e.g. tracks. For this study we need to repeat the reconstruction starting from raw data, since the SVD clusters information is not stored in mDSTs. Therefore, we unpack the data, apply the prompt calibration and run the full reconstruction. In the following section results on Runs 566 and 565 from Experiment 22 (acquired in 2021) are reported. In order to get a complete view, the global reconstruction is chosen over the tracking one, so the generated ntuple is the same, i.e. `SVDEventT0TreePerformance`, but with the addition of the TOP time information. Among the data the first to be analyzed is the *hadron*

5.2. PRELIMINARY CHECKS ON HADRONIC EVENTS

skim, which contains hadronic events such as $B\bar{B}$ offering a good benchmark for comparisons between data and MC behavior. To test the feasibility of the algorithm on data, the *bhabha* and the *mumutight* skims, that contain $e^+e^- \rightarrow e^+e^-$ and $e^+e^- \rightarrow \mu^+\mu^-$ events respectively, are studied: these events have a lower track multiplicity and therefore have less clusters, that means that their event time estimate is more difficult to compute.

5.2 Preliminary checks on hadronic events

As a first check to establish if the behavior of the $B\bar{B}$ simulation ($\sigma \approx 0.76\text{ns}$ on $B^0\bar{B}^0$ events) does reproduce hadronic events, some preliminary checks on their topology are studied:

- the number of hits per track;
- the number of signal clusters per event;
- the $CDCEventT0$;
- the $TOPEventT0$.

The number of SVD hits left per track and the number of signal clusters per event are plotted in fig.5.1: the average number of hits per track is 8 and the average number of clusters per event is 71, instead of 80 like in simulated $B^0\bar{B}^0$ events, but still consistent with the expectations for hadronic events. The $CDCEventT0$ and $TOPEventT0$ are plotted in fig.5.2. Since there are no

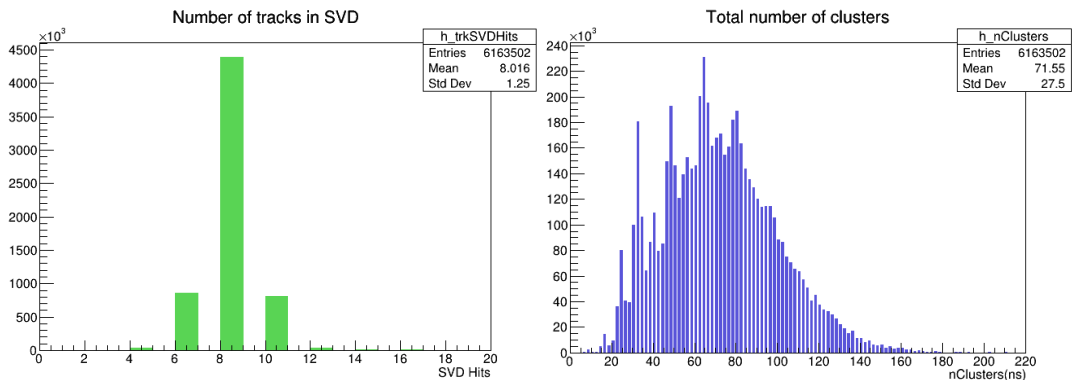


Figure 5.1: Distribution of the number of hits in SVD per track (left) and the number of SVD signal clusters per event (right).

true variables, it is impossible to compute the $EventT0$ residuals with respect

5.2. PRELIMINARY CHECKS ON HADRONIC EVENTS

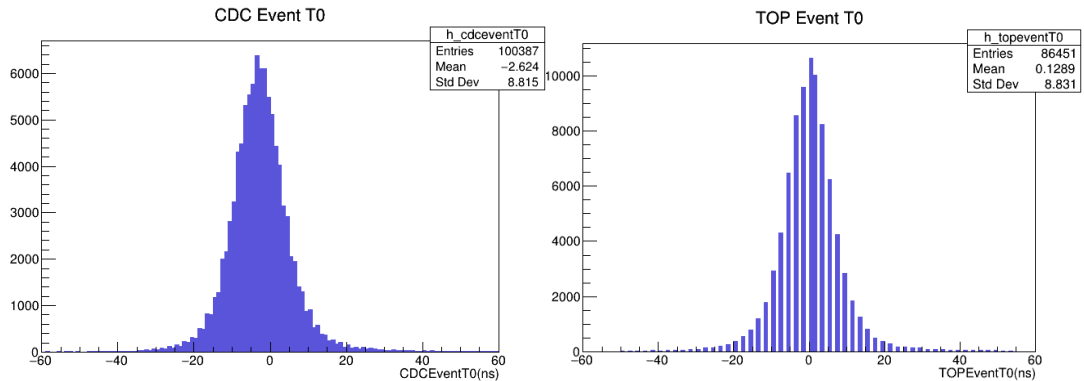


Figure 5.2: (left) $CDCEventT0$ for hadronic events; (right) $TOPEventT0$ for hadronic events from Experiment 22 Run 566.

to $trueEventT0$: it can be useful to define also the residuals of $SVDEventT0$ for simulated $B\bar{B}$ events as:

$$SVDEventT0 - CDCEventT0.$$

The residuals for simulation are shown in fig.5.3. These residuals, computed for events that have an associated $CDCEventT0$, have an efficiency of 99.81%, a mean of -0.03ns and a resolution of 1.08ns and can be used to compare the MC simulation to data. The comparison between the residuals computed

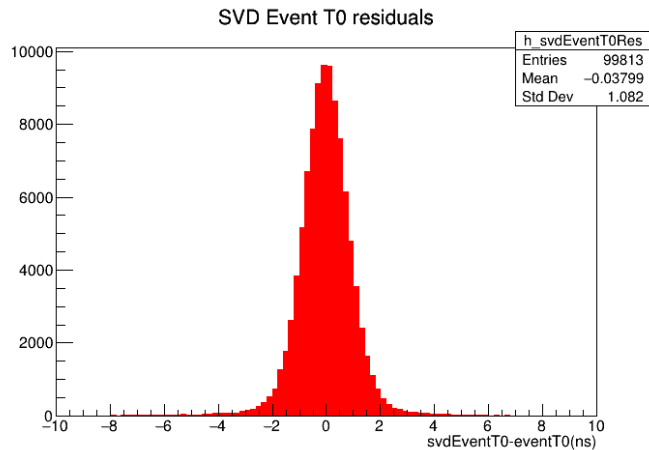


Figure 5.3: $SVDEventT0$ residuals distribution for simulated $B^0\bar{B}^0$ events with nominal beam background and with the $p_T > 250\text{MeV}/c$ selection.

with respect to the $trueEventT0$, plotted in fig.4.17 (right), and those computed with respect to $CDCEventT0$, plotted in fig.5.3, are displayed in table

5.3. SVD EVENT TIME FOR HADRONIC EVENTS

5.1. This table that shows that the two distributions are both essentially unbiased but the width worsens by a factor of 42% when using *CDCEventT0*. The resolution of $\mathcal{O}(1\text{ns})$ estimated for *SVDEventT0-CDCEventT0* on $B\bar{B}$ simulated events is taken as a benchmark value for data. The standard de-

Residuals	Mean[ns]	σ [ns]
<i>SVDEventT0</i> - <i>trueEventT0</i>	0.03	0.76
<i>SVDEventT0</i> - <i>CDCEventT0</i>	-0.03	1.08

Table 5.1: Comparison between the residuals of *SVDEventT0* with respect to *trueEventT0* and *eventT0* for simulated $B^0\bar{B}^0$ events.

viation of the residuals with respect to the CDC is larger than the one with respect to the *trueEventT0* because of the error on the *CDCEventT0*.

5.3 SVD Event Time for hadronic events

The *SVDEventT0* algorithm is applied to hadronic events, obtaining the plot in fig.5.4: the estimate has a mean value of -2.68ns and a standard deviation of 8.62ns, that result compatible with the *CDCEventT0* values of -2.62ns and 8.82ns, respectively. The absolute efficiency for the computation on hadronic events is high, around 99.86%, versus an absolute efficiency of 99.98% on simulated $B^0\bar{B}^0$ events.

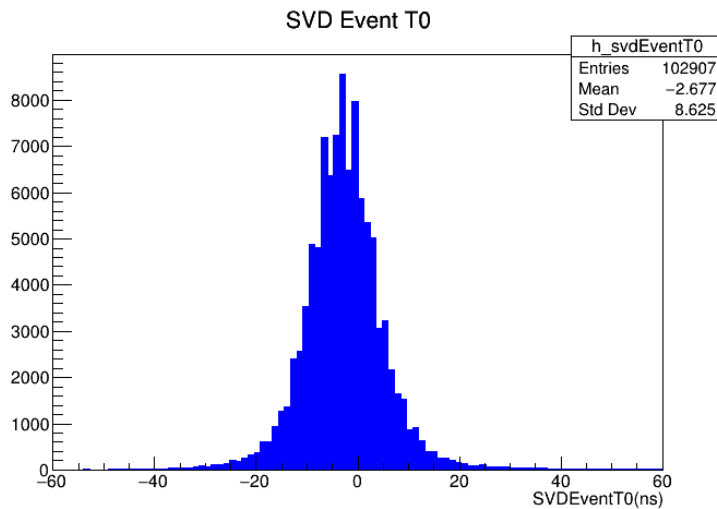


Figure 5.4: *SVDEventT0* distribution for hadronic events from Experiment 22 Run 566.

5.3. SVD EVENT TIME FOR HADRONIC EVENTS

The residuals are calculated with respect to $CDCEventT0$ and $TOPEventT0$, when they exist, and are plotted in fig.5.5: the mean value and the standard deviation are respectively 0.17ns and 1.39ns for

$$SVDEventT0 - CDCEventT0$$

the bias becomes 6 times the one in the simulation, but is still small, while the standard deviations worsens of $\approx 28\%$, but it is still $\mathcal{O}(1\text{ns})$.

The mean value and the standard deviation are respectively -2.68ns and 1.28ns for

$$SVDEventT0 - TOPEventT0.$$

The optimization is applied to other Runs of the same Experiment number,

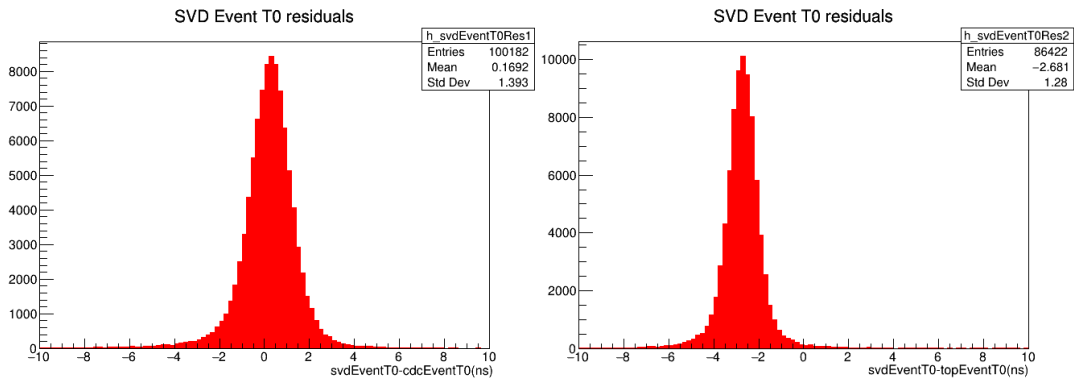


Figure 5.5: $SVDEventT0$ residuals with respect to $CDCEventT0$ (left) and to $TOPEventT0$ (right) with the selection $p_T > 250\text{MeV}/c$ applied on hadronic data from Experiment 22 Run 566.

e.g. Run 565. As earlier, the preliminary checks are carried out: the results are comparable with those of Run 566

- the average number of hits per track is 8;
- the average number of signal clusters per event is 71, that is consistent with hadronic events;
- the $CDCEventT0$ has a bias of -2.48ns and a standard deviation of 8.83ns (versus -0.26ns and 8.82ns for Run 566);
- the $TOPEventT0$ has a bias of 0.24ns and a standard deviation of 8.73ns (versus 0.12ns and 8.83ns for Run 566).

5.3. SVD EVENT TIME FOR HADRONIC EVENTS

The *SVDEventT0* computation (fig.5.6) for this Run has an efficiency of 99.76%, a bias of -2.58ns and a standard deviation of 8.65ns, compatible to the previous run; both its residuals with respect to *CDCEventT0* and to *TOPEventT0* (fig.5.7) have a standard deviation of $\mathcal{O}(1\text{ns})$.

Given the benchmark values of 1.08ns for the resolution and 99.81% for the efficiency on *SVDEventT0* estimated on simulated $B^0\bar{B}^0$ events with nominal background and $p_T > 250\text{MeV}/c$ selection, the absolute efficiency is compatible between data and Monte Carlo, being $\approx 99.8\%$. The biases and standard deviations obtained for the residuals with respect to the CDC and the TOP are stored in table 5.2: the bias increases by 6 times, but it is still not a significant variation, while the standard deviation increases by $\approx 30\%$ with respect to MC (SVD-CDC). Anyways, SVD can achieve great efficiency $\varepsilon > 99\%$ and resolution $\mathcal{O}(1\text{ns})$ on hadronic events.

	e22r566	e22r565	MC $B^0\bar{B}^0$
mean(SVD-CDC)[ns]	0.17	0.14	-0.03
mean(SVD-TOP)[ns]	-2.68	-2.69	/
$\sigma(SVD - CDC)$ [ns]	1.39	1.38	1.08
$\sigma(SVD - TOP)$ [ns]	1.28	1.26	/
ε_{SVD}	99.86%	99.76%	99.81%

Table 5.2: Summary of the *SVDEventT0* estimate performances for hadronic events from Experiment 22 Runs 566 and 565 and comparison with MC $B^0\bar{B}^0$ events with nominal beam background.

5.3. SVDEVENT TIME FOR HADRONIC EVENTS

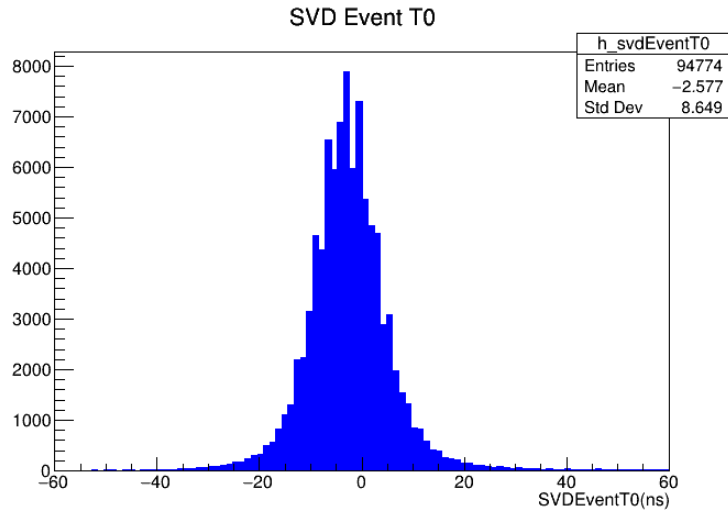


Figure 5.6: $SVDEventT0$ distribution for hadronic events from Experiment 22 Run 565.

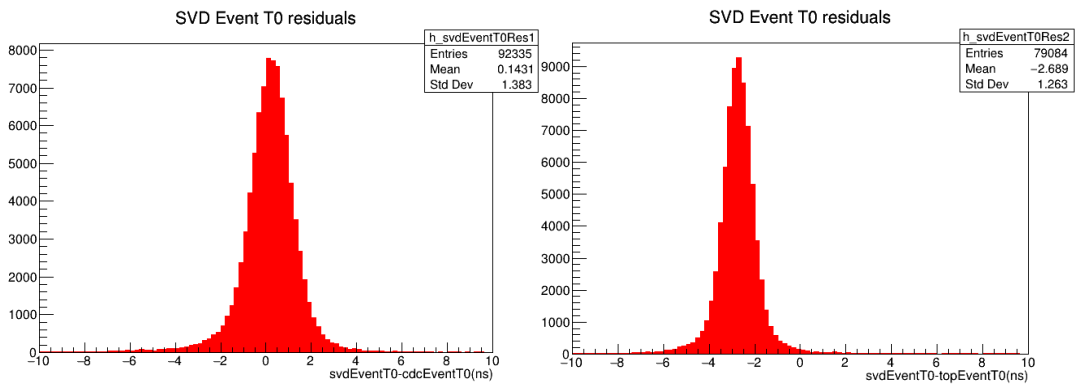


Figure 5.7: $SVDEventT0$ residuals with respect to $CDCEventT0$ (left) and to $TOPEventT0$ (right) for hadronic events with the selection $p_T > 250 \text{ MeV}/c$ from Experiment 22 Run 565.

5.4 SVD Event Time for BhaBha and μ -pairs

The performances of the algorithm can be tested on the other skims with a lower track multiplicity from Experiment 22 Run 566:

- *bhabha* skim: contains triggered events corresponding to BhaBha events;
- *mumutight* skim: contains triggered events with μ -pairs;

These datasets are useful to study the feasibility of the *SVDEventT0* computation: since these events have a 2 track multiplicity, they have a lower number of signal clusters per event, therefore the *SVDEventT0* may be more difficult to compute with respect to hadronic events, that count 10 tracks per event on average. Since the number of signal clusters, in fig.5.8, per event is

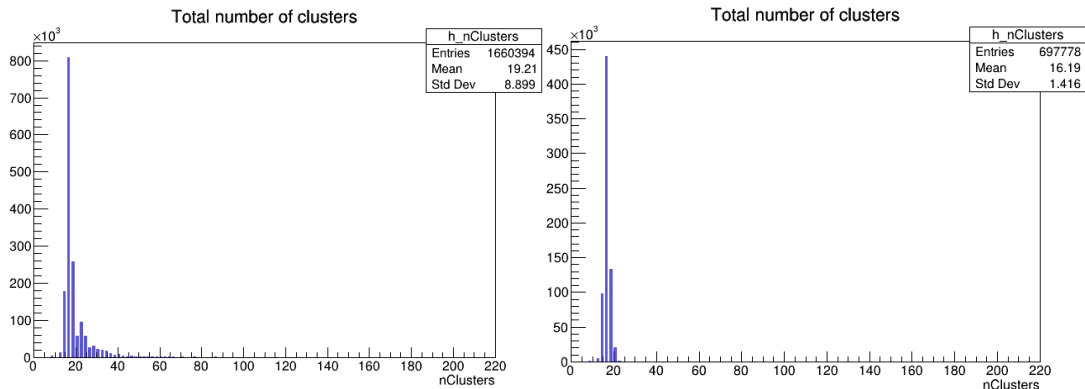


Figure 5.8: Number of signal cluster distributions for *bhabha* (left) and *mumutight* (right) events from Experiment 22 Runs 566.

between 16 and 19 and the average number of clusters per track is 8, then in both cases the track multiplicity per event is ≈ 2 as expected. The algorithm is applied to both skims: the *SVDEventT0* distribution, plotted in fig.5.9, for μ -pairs is wider than the others since the trigger jitter is worse on μ -pairs events. The *SVDEventT0* residuals are plotted in figs.5.10 and 5.11: the efficiency is still above 99% and the resolution is $\mathcal{O}(1\text{ns})$.

5.4. SVD EVENT TIME FOR BHABHA AND μ -PAIRS

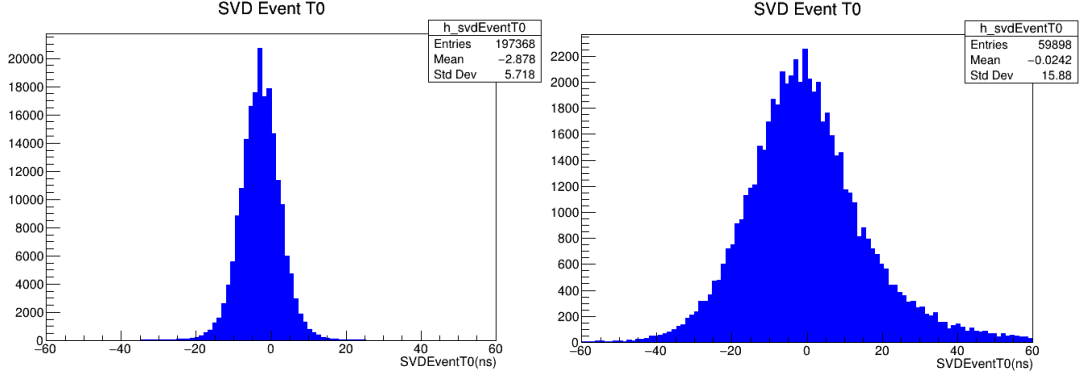


Figure 5.9: $SVDEventT0$ distribution for $BhaBha$ (left) and μ -pairs (right) events from Experiment 22 Run 566 with the selection $p_T > 250 \text{ MeV}/c$.

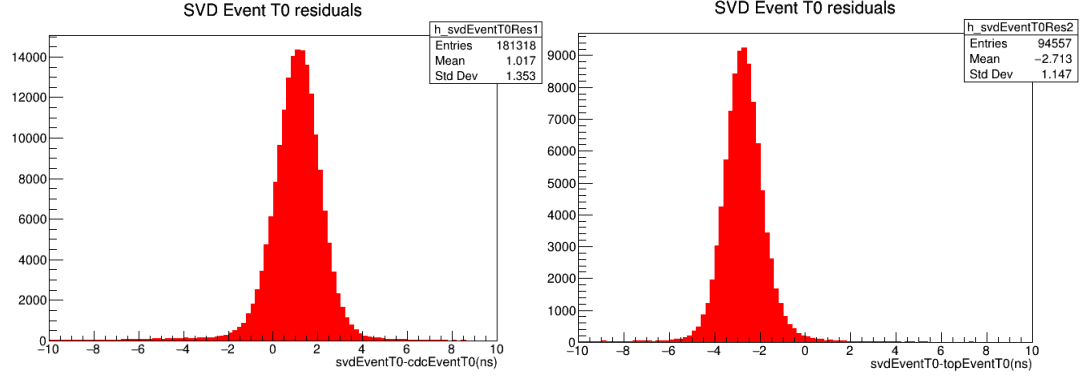


Figure 5.10: $SVDEventT0$ residuals with respect to $CDCEventT0$ (left) and to $TOPEventT0$ (right) for $BhaBha$ events from Experiment 22 Run 566 with the selection $p_T > 250 \text{ MeV}/c$.

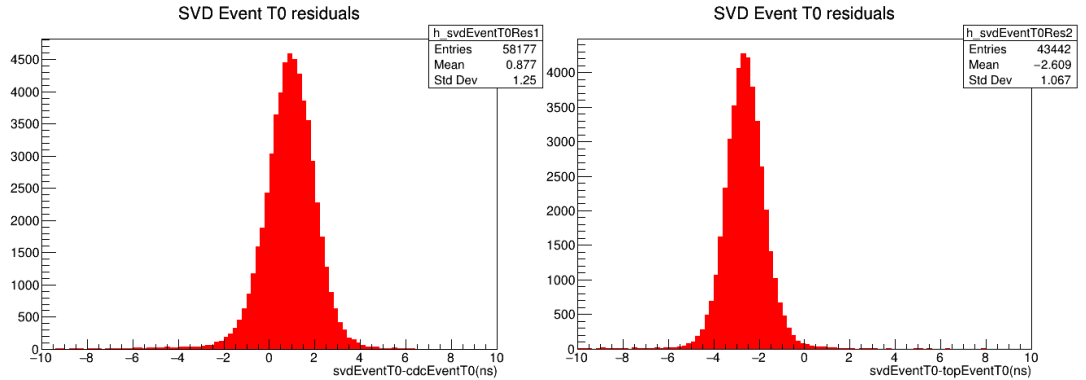


Figure 5.11: $SVDEventT0$ residuals with respect to $CDCEventT0$ (left) and to $TOPEventT0$ (right) for μ -pairs events from Experiment 22 Run 566 with the selection $p_T > 250 \text{ MeV}/c$.

5.5 Summary of the performances on data

SVD can provide an *eventT0* with a resolution of $\mathcal{O}(1\text{ns})$ for hadronic, BhaBha, and muonic events. The standard deviations of the residuals are listed in table 5.3

	$\sigma(SVD - CDC)[\text{ns}]$	$\sigma(SVD - TOP)[\text{ns}]$
hadron	1.39	1.28
BhaBha	1.35	1.15
mumutight	1.25	1.07
hadron (r565)	1.38	1.26

Table 5.3: Standard deviations of the *SVDEventT0* residuals for e22r566 (*hadron*, *BhaBha* and *mumutight* skims) and e22r565 (*hadron* skim only).

SVDEventT0 absolute efficiencies can be compared to those of the other detectors in giving an *eventT0*, as shown in table 5.4. Its absolute efficiency is higher than the ones from the CDC and the TOP, which are $<98\%$ and $<84\%$ respectively, on hadronic, BhaBha and μ -pairs events. Therefore,

Skim	Number of events	$\varepsilon(CDC)$	$\varepsilon(TOP)$	$\varepsilon(SVD)$
Hadrons	103132	97.38%	83.83%	99.78%
BhaBha	200000	91.57%	47.73%	98.68%
Mumutight	60000	97.06%	72.42%	99.83%

Table 5.4: Absolute efficiency of the *eventT0*s involved in the analysis.

SVD is at first proposed to be used to recover those cases in which the other sub-detectors fail to give an *eventT0*. In table 5.5 the recovery efficiency of *SVDEventT0* is shown: SVD is able to compute an *eventT0* in the majority of cases ($>95\%$) in which both TOP and CDC, or CDC alone (since its efficiency in estimating an event time is much larger than the TOP one) fail.

The biases are displayed in table 5.6, where they are compared to the bias of the *CDCEventT0 - TOPEventT0* residuals from Experiment 14 Run 694, introduced in section 3.6; even though the calibration of SVD cluster time is made with respect to the CDC, the biases are not consistent for the different skims, going from $\mathcal{O}(0.2\text{ns})$ to $\mathcal{O}(1\text{ns})$, but they are still quite small. Those computed with respect to the TOP seem to be constant: the offset between e22r566 and e14r694 for *CDCEventT0 - TOPEventT0* is fixed at $\approx \Delta t = 0.25\text{ns}$. These inconsistencies might reveal the need to calibrate the

5.6. FUTURE PROSPECTS

	hadron	BhaBha	mumutight
Total events	103132	200000	60000
CDC & TOP fails	2.59%	8.42%	2.94%
SVD recovery	99.25%	95.04%	97.50%
CDC fails	2.62%	8.42%	2.94%
SVD recovery	99.26%	95.04%	97.50%

Table 5.5: SVD recovery efficiency for the events without an *eventT0* given by the other detectors.

	hadron	BhaBha	μ -pairs
$SVDEventT0 - CDCEventT0$ [ns]	0.18	1.05	0.89
$SVDEventT0 - TOPEventT0$ [ns]	-2.68	-2.71	-2.61
$CDCEventT0 - TOPEventT0$ [ns]	-2.89	-3.78	-3.52
$CDCEventT0 - TOPEventT0(e14r694)$ [ns]	-3.15	-4.02	-3.77

Table 5.6: Biases of the *eventT0* residuals for e22r566 compared to those of e14r694.

shift among the detector timing algorithms depending on the skim used in the analysis.

To sum up, the *SVDEventT0* algorithm has an excellent performance in estimating an event time using particles with a transverse momentum $p_T > 250\text{MeV}/c$, with an absolute efficiency greater than 98%, higher than that of other sub-detectors, and a resolution of $\mathcal{O}(1\text{ns})$ on the residuals with respect to the CDC and the TOP for different kind of events.

5.6 Future prospects

In addition to the excellent results discussed previously, the *SVDEventT0* estimate has also proven to be favorable in the online reconstruction. The *SVDEventT0* algorithm is added to the Belle II Software Framework (basf2) in the `SVDEventT0Estimator` module. To check its performance with respect to the results given in the previous sections, the two computations (mine and the basf2 one), applied to hadronic events from Experiment 22 Run 566, are plotted in fig.5.12: they turn out to be identical as expected.

The execution time of the `SVDEventT0Estimator` module is compared to that of the CDC module that estimates the *eventT0* from the tracks (`FullGrid`). As stated in section 3.1, the `FullGrid` module takes up to 83% of the HLT processing time, resulting to be the one that takes the longest in the online reconstruction. The ratio of the two execution times is plotted

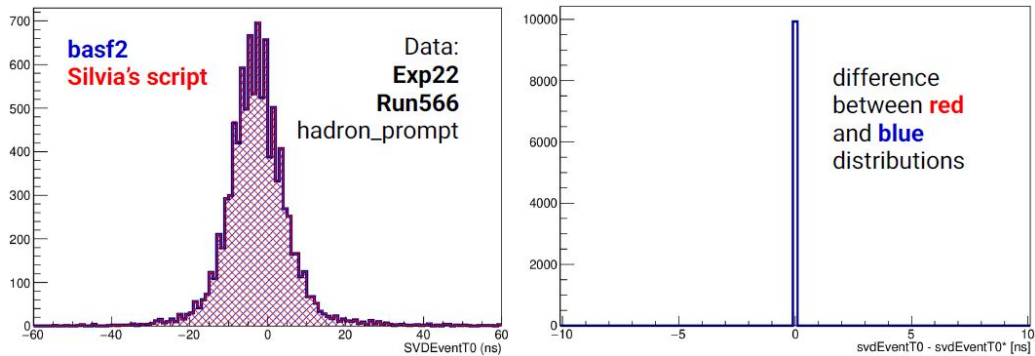


Figure 5.12: Comparison between my *SVDEventT0* (red) and the distribution of the *SVDEventT0Estimator* module (blue) (left) and their residuals (right) for hadronic events from Experiment 22 Run 566.

in fig.5.13: on average, the *SVDEventT0Estimator* module is ~ 1600 times faster than the *FullGrid* one on simulated $B^0\bar{B}^0$ events and ~ 2000 times on hadronic events. Since *SVDEventT0*:

- has a higher absolute efficiency ($> 98\%$) on hadronic, muonic and BhaBha events;
- has a comparable resolution $\mathcal{O}(1\text{ns})$ measured on the residuals with respect to the other sub-detectors;
- is quite aligned with the CDC, with small variations of $\mathcal{O}(1\text{ns})$ at most, depending on the type of skim used;
- has a convenient execution time in the online reconstruction

the *SVDEventT0Estimator* module is going to be used in place of the *FullGrid* module on the official Belle II Software in the next release, planned on June 2022.

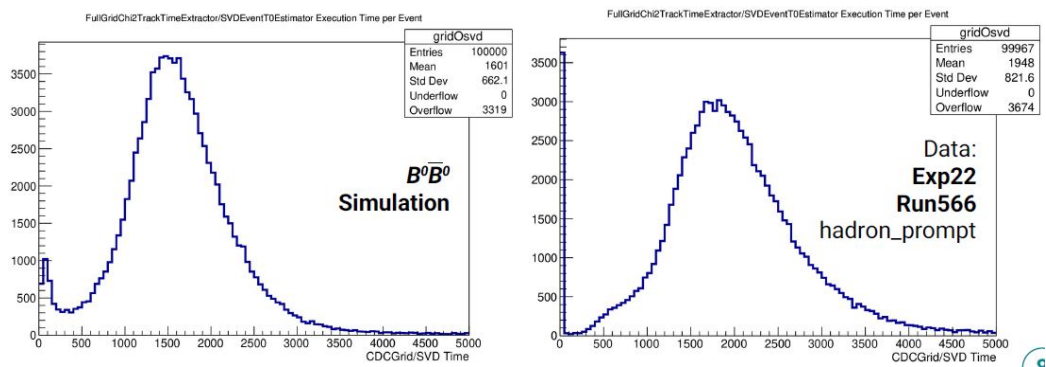


Figure 5.13: Ratio of FullGrid and SVDEventT0Estimator execution times for simulated $B^0\bar{B}^0$ events and hadronic events from Experiment 22 Run 566.

Conclusions

This thesis introduces an estimate of the event time using the Belle II Silicon Vertex Detector. This estimate is compared to the event time given by other sub-detectors, the Central Drift Chamber and the Time-of-Propagation, that are already implemented in the Belle II Software Framework. The main motivation of this thesis is to provide an alternative good event time estimate in a framework where distinction of data and the rejection of beam background hits are a crucial element for high precision measurements. In this scenario, the SVD, thanks to high efficiency and hit time resolution, is fundamental for the beam background rejection based on the hit time on the detector layers.

The algorithm that I developed computes this estimate as the average of the time of SVD clusters associated to tracks. It is applied to different physics events that are interesting in the Belle II framework to study its feasibility. The performance is excellent as the *SVDEventT0* has the a good resolution, compatible to the other time measurements ($\mathcal{O}(1ns)$ on both simulated events with nominal beam luminosity and data collected in 2021) but also a higher absolute efficiency ($>99.7\%$) on hadronic events versus the absolute efficiency of the Central Drift Chamber of about 97.5%: SVD is able to give a time estimate even when the other sub-detectors fail.

Moreover the execution time of the *SVDEventT0* estimator in the online reconstruction is measured to be significantly reduced with respect to the one of the current algorithm that gives the CDC event time. It is estimated to be 1600 times faster than the current one for simulated $B\bar{B}$ events and ≈ 2000 times faster for hadronic events. This result turns out to be promising for the Data AcQuisition system: since the increasing luminosity will also bring a higher rate of beam background, the data acquisition could stop due to the trigger rate too high. One of the processes that take up the most processing time in the online reconstruction is exactly the one that estimates the CDC event time. The new time event estimator takes significantly less time in the online reconstruction: this increases the maximum trigger rate limit, given by the CDC estimator, and could help to preserve good physics performance even with higher luminosities.

For these reasons, the SVD event time estimator has been inserted in the Belle II Software Framework and is planned to be used in lieu of the current one in the next Belle II Software release in June 2022.

Bibliography

- [1] W. N. Cottingham and D. A. Greenwood, "An Introduction to the Standard Model of Particle Physics". Cambridge University Press, 2nd edition, 2007.
- [2] E. Kou et al., "The Belle II Physics Book. Progress of Theoretical and Experimental Physics", 2019(12), Dec 2019.
- [3] N. Cabibbo, Unitary Symmetry and Leptonic Decays. *Phys. Rev. Lett.*, 10:531-533, 1963
- [4] I. Adachi et al., "Search for an Invisibly Decaying Z' Boson at Belle II in $e^+e^- \rightarrow \mu^+\mu^-(e^\pm\mu^\mp)$ Plus Missing Energy Final States" (Belle II Collaboration) *Phys. Rev. Lett.* 124, 141801 2020.
- [5] F. Abudinén et al., "Search for Axionlike Particles Produced in e^+e^- Collisions at Belle II" (Belle II Collaboration) *Phys. Rev. Lett.* 125, 161806 2020.
- [6] B. Aubert et al., "Observation of the Semileptonic Decays $B \rightarrow D^*\tau^-\bar{\nu}_\tau$ and Evidence for $B \rightarrow D\tau^-\bar{\nu}_\tau$ " (BABAR Collaboration) *Phys. Rev. Lett.* 100, 021801 2008.
- [7] Ed. A.J. Bevan, B. Golob, Th. Mannel, S. Prell, and B.D. Yabsley, "Physics of B factories" *Eur. Phys. J. C* 74 (2014) 3026, SLAC-PUB-15968, KEK Preprint 2014-3.
- [8] E. Fernandez et al. "Lifetime of Particles Containing B Quarks". *Phys. Rev. Lett.* 51, 1022 (1983).
- [9] Albrecht et al. "Observation of B0B0 Mixing". *Phys. Lett. B* 192, 245 (1987).
- [10] Y. Ohnishi et al., "Accelerator design at SuperKEKB." *PTEP*, 2013:03A011, 2013.

- [11] SuperB Collaboration, "SuperB Technical Design Report", (2013).
- [12] Status of the SuperB project - M. Boscolo on behalf of the SuperB Accelerator Team 2009.
- [13] "SuperKEKB Design Report" (SuperKEKB Collaboration) 2014.
- [14] T. Abe et al., "Belle II Technical Design Report", 2010.
- [15] G. Casarosa, "SVD Time - Update and plans" 35th Belle II General Meeting, 2020.
- [16] P. M. Lewis et al., "First measurements of beam backgrounds at SuperKEKB." Nucl. Instrum. Meth. A, 914:69–144, Jan 2019.
- [17] Z. Wang, "Updates on SVD beam background studies" 41st Belle II General Meeting 2022.
- [18] I. Adachi et al. "Detectors for extreme luminosity: Belle II" In: Nucl. Instrum. and Meth. A, 907 (2018) pp. 46–59. issn: 0168-9002. doi: <https://doi.org/10.1016/j.nima.2018.03.068>. url: <https://www.sciencedirect.com/science/article/pii/S0168900218304200>.
- [19] B. Spruck "Belle II Pixel Detector Commissioning and Operational Experience" The 28th International Workshop on Vertex Detectors PoS(Vertex2019)015 <https://pos.sissa.it/373/015/pdf> 2019.
- [20] Fischer P., et al. "Progress towards a large area, thin DEPFET detector module Vertex detectors." Proceedings, 15th International Workshop, VERTEX 2006, Perugia, Italy, September 25-29, 2006, Nucl. Instrum. Methods, A582 (2007), pp.
- [21] L. Massaccesi, "Performance study of the SVD detector of Belle II and future upgrades" Master Thesis 2021.
- [22] S. Longo, "Crystal Calorimeters and the Belle II ECL" Belle II Physics Week 2021.
- [23] T. Hara, T. Kuhr, and Y. Ushiroda, "Belle II Coordinate System and Guideline of Belle II Numbering Scheme" 2011.
- [24] A. Moll "The Software Framework of the Belle II Experiment." Journal of Physics: Conference Series 331.3, p. 032024. doi:10.1088/1742-6596/331/3/032024. url:<https://doi.org/10.1088/1742-6596/331/3/032024> dec. 2011.

- [25] M. T. Prim et al., "Design and Performance of the Belle II High Level Trigger" 40th International Conference on High Energy physics - ICHEP2020.
- [26] G. Rizzo, "The Belle II Silicon Vertex Detector Performance and Operational Experience in the first year of data taking" VERTEX 2020 2020.
- [27] V. Bertacchi, "Performance of the Belle II Silicon Vertex Detector and Standalone Track Finder" Connecting the Dots/Intelligent Trackers 2019.
- [28] G. Casarosa et al., "Track Finding at Belle II" (Belle II Tracking Group) Comput.Phys.Commun. 259 (2021) 107610.
- [29] E. Lund, L. Bugge, I. Gavrilenko, A. Strandlie, "Track parameter propagation through the application of a new adaptive Runge-Kutta-Nystrom method in the ATLAS experiment", Journal of Instrumentation 4 (04) (2009) P04001-P04001. doi:10.1088/1748-0221/4/04/P04001.
- [30] Y. Uematsu et al., "The Belle II SVD Collaboration, The Design, Construction, Operation and Performance of the Belle II Silicon Vertex Detector" (Belle II Collaboration) Nucl. Instrum. Meth. A Volume 1033, 2022, 166688, ISSN 0168-9002, <https://doi.org/10.1016/j.nima.2022.166688>.
- [31] V. Vobbiliseti, K. Trabelsi, Efforts for speeding the reconstruction on HLT (Belle II Internal Meeting) 2021.
- [32] V. Bertacchi, K. Trabelsi, TrackFitter DAF performance studies (Belle II Internal Meeting) 2022.
- [33] H. Kolanoski, N. Wermes, "Particle detectors" - Oxford University Press 2020.
- [34] F. Forti, "Semiconductor Detectors" - Belle II Physics Week 2021.
- [35] L. Corona et al., "New Results from the Silicon Vertex Detector of the Belle II Experiment" European Physical Society conference on high energy physics 2021" PoS EPS-HEP2021 DOI: <https://doi.org/10.22323/1.398.0802> 2021.
- [36] M.J. French et al., "Design and results from the APV25, a deep sub-micron CMOS front-end 156 chip for the CMS tracker", Nucl. Instrum. Meth. A 466 (2001) 359.
- [37] N. Braun, "CDC and Future Plans - Event T0" (Belle II Internal Meeting) 2019.

- [38] T. Schlueter, "Event Time from Tracks" (Belle II Internal Meeting) 2015.
- [39] C. Hearty, "Determination of event T0 using ECLCalDigits" (Belle II Internal Meeting) 2018.
- [40] M. Starič, "Requirements for integration of TOP Event t0" (Belle II Internal Meeting) 2021.
- [41] M. Starič, "TOP Event T0: some further studies" (Belle II Internal Meeting) 2022.